RESONANCE AND STABILITY OF CURVED CAPILLARY SURFACES

A Dissertation

Presented to the Faculty of the Graduate School

of Cornell University

in Partial Fulfillment of the Requirements for the Degree of

Doctor of Philosophy

by

Chun-Ti Chang

August 2014

RESONANCE AND STABILITY OF CURVED CAPILLARY SURFACES

Chun-Ti Chang, Ph.D.

Cornell University 2014

Due to surface tension, a liquid drop below the capillary length scale naturally forms a spherical cap on solid surfaces. Drops on solid surfaces are denoted as sessile drops to distinguish from spherical drop without liquid-solid contact. When a sessile drop is disturbed, surface tension restores the drop's partial spherical profile. Surface tension thus arms the liquid-gas interface as a spring. If one further considers the drop's mass and viscosity, then sessile drops can be identified as a mass-spring-damper system. The mechanical response of a drop reflects the three aspects of the system, and this experimental study mainly investigates these different aspects by probing the static and dynamic response of sessile drops using quasi-static and oscillatory forcing.

This experimental study focuses on the resonance of mechanically vibrated sessile drops and then extends to the mechanics of water balloons. Shape, frequency and amplitude responses of resonating sessile drops are first examined for individual modes. To characterize the observations, different aspects of experiments are related to Rayleigh-Lamb[90, 62], Bostwick-Steen inviscid[10] and Bostwick-Steen viscous potential flow (VPF)[16] theories. Observed mode shapes are related to predictions from Bostwick-Steen inviscid theory via ray-tracing simulation. Frequency responses are compared to all three theories, with Bostwick-Steen VPF theory best matching experiments as it includes both the presence of substrate and weak viscosity of drops. The observed amplitude responses of harmonic and subharmonic modes are qualitatively explained by nonlinear spring models, and

a frequency-matching technique is demonstrated to trigger superharmonic modes. Further exploration reveals the interactions of modes such as spectral crossing and mode mixing, from which a mode separation technique is developed. For subhemispherical drops, typical observations are mixtures of a half-frequency subharmonic non-zonal mixing a harmonic zonal mode. For superhemispherical drops, more diverse mixing phenomena are discovered by preliminary observations.

The investigation is extended to membrane-covered drops, or balloons. As it turns out, balloons can resemble purely liquid sessile drops in many aspects. When quasi-statically inflated, the balloons may or may not respond monotonically, and the response is adjustable via material properties and other parameters. When vibrated, these balloons exhibit several mode shapes similar to those of vibrated sessile drops. In fact, a one-to-one correspondence exists between mode shapes of drops and balloons, and therefore for these tests, balloons are technically drops equipped with a much higher effective surface tension.

BIOGRAPHICAL SKETCH

Chun-Ti Chang was born in Taipei, Republic of Taiwan on December 3rd, 1982. He attended National Taiwan University (NTU), where he was first admitted to the Department of Mechanical Engineering and later accepted to pursue a second major in the Electrical Engineering. With his double majors of mechanical and electrical engineering, he graduated in May 2006. As a male citizen of Taiwan, he then fulfilled his military service as a technical sergeant in the Taiwanese army. On the day of his dismissal, he was awarded by the commander of the military depot for his technical contribution in the camp. After working as a full-time teaching assistant in the Department of Mechanical Engineering at NTU, he attended Cornell to pursue his doctoral degree in 2008. He officially joined Steen group and conducted research under the guidance of Prof. Steen and Prof. Daniel. As a PhD candidate in the field of Theoretical and Applied Mechanics working with advisors in Chemical and Biomolecular Engineering, he is privileged to participate the be endowed for McManus Design Award by Sibley School of Mechanical and Aerospace Engineering and the Best Oral Presentation of Graduate Student Symposium by Chemical and Biomolecular Engineering. In 2013, Chun-Ti and Prof. Steen together won $5000 cash award for the CASIS Contest of Ideas.

To my family and friends back home, who have been waiting for my return on the other side of the earth.

ACKNOWLEDGEMENTS

Gratefully, the author appreciates all the machining work conducted by Glenn Swan, the Research Support Specialist at Olin Hall machine shop. With extreme care, high precision and brief lead time, all custom mechanical parts are manufactured by Glenn. The author sincerely appreciates all the guidance from co-advisors Dr. Paul H. Steen and Dr. Susan Daniel, with whom the theoretically sound and technically feasible objectives are defined, by whom all precious optical imaging hardware and chemical supplies are offered virtually without any limit of quantity, and from whom constant advising, financial and even mental support are received. Humbly and gratefully, the author acknowledges Dr. Michel Y. Louge for his generous offer of the precious VTS-100 mechanical vibrator, as without whose tremendous power and pristine quality of oscillation signal the phenomena of interest can be explored but only to some limited extent. In addition, the author recognizes Dr. Wolfgang H. Sachse's reference to Dr. Louge as the determining factor that facilitates all recent progress in experiments, as without the introduction, the mechanical vibrator remained unavailable. The author expresses the gratefulness for any technical knowledge associated with conditioning, acquisition and suppression of mechanical oscillatory signal instructed by Dr. Louge, Dr. Alan T. Zehnder and Dr. Wolfgang H. Sachse. The author thanks Prof. Claude Cohen, Prof. James T. Jenkins, Prof. Anil Narayan Netravali and Dr. Sam Zeng for intellectual and technical support for polymeric materials, and Prof. Richard H. Rand and Prof. Tim J. Healey inquiries about mathematical modelling. In addition, the author appreciates the considerate technical support from Cornell NBTC staff Dr. Teresa Porri, Penny Burke, Brian Bowman and Graham Kerslick. The author also thanks Dr. Bruce Land and Teaching Support Specialists David Hartino and Dan Mittler for frequent assistance associated with electronics and signal retrieval. The author

hopes to express his appreciation to the varieties of inspiring ideas and technical support of equipments constantly provided by colleagues Dr. Konrad Boettcher, Prof. Ling Chao at National Taiwan University, Dr. Deirdre A. Castello, Donald Lee, Mark Richard, Angela Chih-Yun Hsia, Hung-Lung Hsu, Dr. An-Cheng Ruo and NBTC staff . Among the ideas from Donald, enhancing observability by installation of multiple mirror is the one inspiring the design model of `OmniView` and facilitating subsequent experiments. Finally, the author thanks NASA, NSF and Xerox for their long-term financial support.

TABLE OF CONTENTS

LIST OF TABLES

LIST OF FIGURES

CHAPTER 1

INTRODUCTION: VIBRATION OF SESSILE DROPS

The content of this chapter has been largely disseminated in Chun-Ti Chang, Joshua B. Bostwick, Paul H. Steen, and Susan Daniel, *Phys. Rev. E, 88:023015, Aug 2013*.

Active manipulation of drops facilitates numerous applications, such as ink-jet printing, spray cooling [105], enhanced heat conduction [25, 24, 54], suspension collection[109], droplet actuation[5] and mixing within droplets [95]. Oscillatory forcing is frequently used for active manipulation, and different applications require different extents of droplet oscillation. On one extreme, ink-jet printing requires suppressing oscillation of ink droplets. On the other extreme, spray cooling[54] requires maximizing oscillation to induce atomization[105]. For intermediate cases such as droplet transport[25, 24] and suspension collection[109], forcing must incorporate adequate acceleration and appropriate frequency to induce target resonance while retaining bulk continuity. All these applications require effective control of a drop's resonant behaviors. Natural oscillations underlie resonance. To optimally control drops in different applications, fundamental knowledge about shape, frequency and amplitude responses of oscillating drops is crucial.

The dynamics of an oscillating free drop was predicted by Lord Rayleigh[90]. This early work took account of surface tension and inertia in the case where viscous effects are negligible, as appropriate for water drops on the millimeter scale. Rayleigh characterized the dynamics of a plucked, freely oscillating, spherical drop by its natural frequencies:

$$\omega_k^2 = \frac{\sigma}{\rho R^3} k(k-1)(k+2), \quad k = 0, 1, 2, ... \tag{1.1}$$

where σ is the surface tension, R the radius of the undisturbed drop, and ρ the density of the drop fluid. Corresponding drop mode shapes have radial deformations that are given by the Legendre polynomials $P_n(\cos\theta)$, a subset of the spherical harmonics (solutions of the Laplace equation in three dimensions), where θ is the angle to the north pole in a spherical coordinate system [62, 101]. Note that these shapes are axisymmetric. These mode shapes P_k with frequencies ω_n shall be referred to "Rayleigh drops." Rayleigh's predictions have been verified experimentally for immiscible drops by Trinh and Wang [102] and for free drops in microgravity by Wang, Anilkumar, and Lee [108], both using acoustic excitation. Rayleighs prediction for the oscillating free drop still sees widespread use even in situations where the drop is not completely free, as for a drop levitated [47, 12] or in contact with a solid [99, 26, 28, 77, 18] or with another liquid [29]. Modifications, *ad hoc* or otherwise, to Eq. 1.1 are often invoked to account for the influence of substrate contact on drop frequency [114, 83, 93]. Why has Rayleigh's result proved to be so resilient and what are its limits of applicability to the sessile drop case?

A sessile drop is a drop that sits on a planar substrate. For sessile drops both the equilibrium contact angle and the mobility of the contact line will influence frequencies and mode shapes. A subset of Rayleigh drops are exact solutions for inviscid sessile drops under the right conditions. This is because even modes ($k =$ even) have a zero normal velocity on the equatorial plane and thereby automatically satisfy the no penetration condition. Hence, provided the contact-line motion of the sessile drop is not restricted (i.e., is mobile) and the equilibrium shape is hemispherical (i.e., has a 90° contact angle), the Rayleigh half-drop is a solution to the sessile drop governing equations. These solutions will be called "Rayleigh half-drops" and, along with their frequencies, constitute the Rayleigh spectrum.

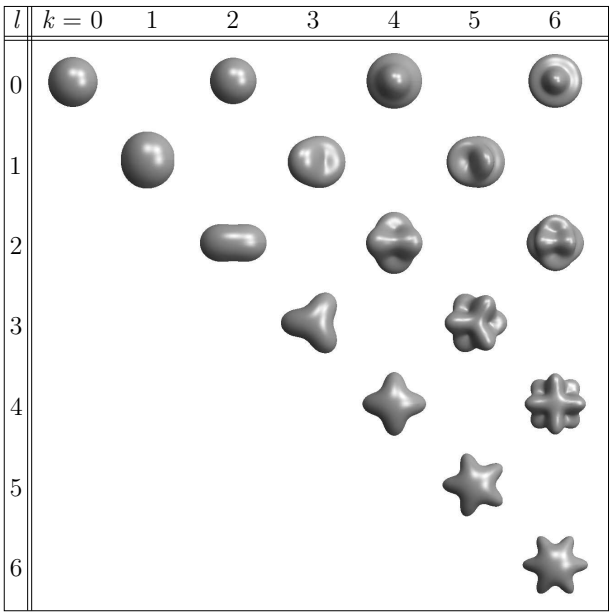

Figure 1.1: Eigenmodes of hemispherical drops predicted by the theory of Rayleigh and Lamb are spherical harmonics. Zonal modes are in row 1 ($l = 0$), sectoral modes are along the diagonal ($k = l$), and tesseral modes are where $k = l$. Note that the shape at [0, 0] is the static drop shape.

They are illustrated in the first row of figure 1.1 ($l = 0$ modes).

There are other solutions to the linear stability equations that the Rayleigh drops solve, as noted by Lamb[62] and others[14]. These solutions are also spherical harmonics, but include shapes that break the axisymmetry of the Rayleigh drops:

$$r(\theta, \psi) = 1 + \epsilon P_k^l(\cos\theta)\cos(l\psi), \quad 0 \leq \theta \leq \pi, \quad 0 \leq \psi \leq 2\pi \tag{1.2}$$

Here r is the scaled radial coordinate and θ and ψ are polar and azimuthal angles in spherical coordinates, ϵ is the magnitude of deformation such that $\epsilon \ll 1$, and P_k^l is the associated Legendre function of degree k and order l. The axisymmetric Rayleigh half-drops are zonal modes in the spherical harmonic classification, corresponding to $l = 0$ with mode shapes $P_k = P_k^0$, as noted. The shapes of Eq. 1.2 have frequencies given by Eq. 1.1, which makes them degenerate eigenmodes. These modes and frequencies shall be referred to as the "Lamb spectrum."

For Lamb modes, the condition $k + l =$ even guarantees no penetration on the equatorial plane and, hence, provides nonzonal solutions to the sessile drop equations, again for hemispherical drops with mobile contact lines. These are referred to as "Lamb half-drops" and illustrated in figure 1.1 in the rows below row one. The gaps in figure 1.1 represent the missing spherical harmonic solutions ($k + l =$ odd). Nonzonal modes ($l = 0$) are called "sectoral" if $k = l$, and "tesseral" if $k = l$. In figure 1.1, zonal modes occupy row one, sectoral modes fall on the diagonal, and the tesseral modes are all others. The [0, 0] entry is the static equilibrium spherical-cap shape.

For Lamb half-drop solutions, it turns out that nonzonals have identical frequencies to the corresponding zonal mode, according to the modal degeneracy. That is, all modes with the same k have the same frequency. The earliest observation of these nonzonal mode shapes is reported by Holter and Glasscock[50] for Leidenfrost drops. According to these authors, the mode shapes result from the disturbance of the evaporating steam flow which both levitates and disturbs the drop. Note that in contrast to most other experiments with resonating drops, no mechanical vibration is employed in this Leidenfrost experiment. To excite nonzonals of free drops by mechanical vibration, the source of excitement must break the symmetry by some means. For example, Shen *et al.* [94] have reported sectoral free drop oscillations excited using ultrasound. They employ a modulated time-periodic driving signal. The base signal (higher frequency) biases the drop to a prolate shape and the superimposed modulation (lower frequency) induces the sectoral shape. Sectorals up to seventh order are reported (up to $k = l = 7$) and, with a simple adjustment, observed frequencies compare reasonably to Lamb's sectoral predictions. For other levitation methods, using various excitation techniques, only zonal modes have been reported [47, 83]. Tesseral modes have never

been reported for levitated drop experiments, to the author's knowledge, although the large-amplitude shapes reported in the free fall experiments of Azuma and Yoshihara[3] may have started from tesserals. Even for levitated drops, the levitating force can influence the spectrum, as has been reported for diamagnetic levitation[47].

Drop contact with a solid has long been recognized to modify the Rayleigh spectrum. Strani and Sabetta[99, 100] studied drops in contact with a solid support of spherical bowl shape. Studies were restricted to axisymmetric shapes and predicted frequencies of vibration compared favorably to experiment[102]. More recently, Bostwick and Steen have reported the spectrum for a drop constrained by a spherical belt support[8, 9]. This two-parameter family of constraint recovers as special cases the Strani and Sabetta spectrum and that for a drop pinned along a circle, also considered elsewhere[7, 87]. Strani and Sabetta's spherical bowl results were pressed into service to account for the influence on frequency of the constraint of a planar substrate, with some success, at least for non-wetting drops[52]. Smithwick and Boulet's measurements of a vibrating mercury drop on a glass plate showed zonal shapes with a frequency response at half the driving frequency[52]. A subharmonic response was also noted by Yoshiyasu et al., who studied gravity-distorted nonwetting sessile drops, driven by a plane-normal substrate oscillation[114]. They reported sectoral-like shapes. Chebel *et al.* subjected a buoyant drop, attached to a capillary and immersed in a water bath, to volume oscillations[18]. They report a frequency response that matches the Rayleigh spectrum to within 3% for the first three zonal modes, even though the buoyancy considerably distorts the static shape. Brunet and Snoeijer vibrate drops on hydrophobic surfaces (contact angle 140°) and observe star-like, tesseral modes as the acceleration of the surface increases[12]. They note a chaotic regime where the

coexistence between two or several modes leads to an undefined (or fluctuating) number of nodes just before drop breakup.

The literature on driven sessile drops is large and growing; the literature review here focuses on previous work most relevant to this experimental study. More recently, the dynamics of the three-phase contact line has been a focus of theoretical efforts[67, 68, 36]. Lyubimov *et al.* [68] restricts to axisymmetric oscillations of a hemispherical drop, allowing contact-line movement by a Hocking condition[49]. A related analysis of asymmetric disturbances considers both plate-normal and plate-tangential driving forces[67]. The analysis of Fayzrakhmanova and Straube[36] also restricts to hemispherical drops and axisymmetric disturbances, where here the new feature is that a stick-slip Hocking condition[49] has been implemented. Modifications of the Rayleigh spectrum are reported in these three studies. Noblin et al. vertically vibrated sessile drops exhibiting moderate contact angle hysteresis ($10^\circ \sim 15^\circ$) and studied the transition from pinned to slipping contact line, the stick-slip regime[76]. These studies showed that the transition between regimes occurs when the contact angle fluctuation during vibration exceeds the contact angle hysteresis. Comparison of stick-slip behavior is also conducted in experiments that use white noise vibration to excite multiple resonance modes of sessile water drops on either a hydrophobic polystyrene surface (no slip), or superhydrophobic pillared surface (with significant slip)[71]. These experiments demonstrate that resonance frequencies decrease with contact angle and that contact-line slipping impacts (dampens) the higher frequency modes more than the lower ones. In a more recent follow-up study of water drops on a hydrophobic substrate driven by plane-normal oscillations, Noblin et al. observe sectoral shapes up to $l = 3$ and report that contact-line mobility is a necessary condition for these to appear[77]. When the contact line is pinned, at lower driving amplitudes, only zonal modes are

seen. A model that uses the one-dimensional dispersion relationship for gravity-capillary waves on a liquid bath of finite depth is proposed to account for these frequencies. Sharp *et al.* test Noblins model by measuring frequencies of nonzonal drops over a range of contact angles and find qualitatively similar dependence but quantitative discrepancies on the order of 20[93].

Another recent focus of experimental studies of sessile drops is the "rocking mode" [26, 53], an asymmetric mode, excitable by either in-plane or plane-normal driving oscillations, which seems to be linked to droplet translation[77, 29, 11]. Brunet et al. induce droplets to move uphill[11]. Noblin et al. use a combination of in-plane and plane-normal driving oscillations to induce droplets to move laterally[77]. Dorbolo et al. bounce an oil drop on a vibrating oil-air interface and report observed shapes using a spherical harmonics classification[29]. They point out an asymmetric shape $[k, l] = [2, 1]$ that, when excited, "rolls on the vibrated surface without touching it." Finally, Vukasinovic et al. drive a sessile water drop with a piezoelectric actuator and document the wave patterns corresponding to resonance frequencies on increasing driving amplitude until the drop is atomized[105]. On driving harder, they report the following sequence of waves: axisymmetric standing, azimuthal standing, azimuthal rotating, a "lattice mode," preejection waves, and finally atomized breakup. Along the way, 14 zonals are reported and several nonzonals, by making the association via dominant wave numbers. Their nonzonal modes may well be mixtures between more than one pure mode as the transitions in wave numbers are gradual. Their zonals have pinned contact lines and respond harmonically to the driving signal. The nonzonals respond subharmonically, consistent with other literature reports. However, in contrast to the Noblin observation, contact-line motion is believed to coincide with the appearance of nonzonal modes, not to precede it.

This experimental study starts with identification of individual mode shapes. In experiments, symmetry of the sessile drop is broken by the substrate plane and by the nonmobile contact-line behavior. However, because disturbed drop shapes satisfy periodicity in the azimuthal direction, the spherical harmonic classification into zonal, sectoral, and tesseral shapes still holds. Strictly speaking, since the shapes are modified from those for the Lamb half-drops, these are "zonal-like," "sectoral-like," and "tesseral-like" modes. For simplicity, the "like" in what follows may be dropped without confusion. The utility of this classification is demonstrated by showing how zonal, sectoral, and tesseral shapes can be identified. In particular, the observation of the first 37 modes, which includes zonals up to $k = 14$ and nonzonals up to $k = l = 10$, are summarized in figure 2.3. A more practical and visually intuitive approach for identifying modes is proposed based on their number of layers n and sectors l. The $k - l$ and $n - l$ notations are distinguished by the brackets $[k, l]$ and parenthesis (n, l) in the following context. In addition to identifying mode shapes from experiments, a ray-tracing simulation scheme is utilized to directly relate experiments to predicted mode shapes of Rayleigh and Lamb half drops and Bostwick and Steen[10].

Frequency responses of drops are investigated in terms of the resonance frequencies and bandwidths of identified modes. It turns out that nonzonals respond subharmonically, while zonals can respond either harmonically, subharmonically or even superharmonically to the forcing frequency. Resonance frequencies and bandwidths of modes are compared against (1) Rayleigh-Lamb theory (RL)[90, 62], (2) Bostwick-Steen inviscid theory (BS inviscid)[10], and (3) Bostwick-Steen forced viscous potential flow (VPF) theory[16]. As VPF theory best matches experimental observations, both the presence of a solid substrate and the weak viscosity must be explicitly included to properly predict resonance frequencies of drops. Further-

more, BS inviscid theory predicts that sub- and superhemispherical drops exhibit different ordering of modes on the frequency spectrum. Collectively comparing observed resonance bandwidths confirms the predicted spectral crossover.

Although various fascinating mode shapes of drops and liquid baths have been observed for decades, many aspects are still not investigated. Among others, the growth and decay (amplitude response) of subharmonic modes have not been characterized based on direct measurement. This is because of their complex mode shapes. To author's knowledge, the first observation was reported almost two centuries ago[35] for liquid baths by Faraday, roughly six decades ago for Leidenfrost drops[50] by Holter and Glasscock, and 35 years ago for sessile drops[42] by Rodot and co-workers. Subsequently, harmonic and subharmonic resonances of liquid-gas free surface continue to be reported for Faraday wave[31, 22, 32, 4], free drops under zero gravity[103, 3], acoustically levitated and excited free drops[94], vibrated semi-toroidal water ring[57] and mechanically vibrated sessile drops[105, 17]. Based on image analysis[105, 17], axisymmetric(zonal) and nonaxisymmetric(non-zonal) modes are typically quantitatively confirmed as harmonic and half-frequency subharmonic resonances, respectively. While profiles of zonal modes can be precisely measured by side view, those of non-zonal modes cannot. Top-view imaging offers human-readable snapshots of non-zonal modes[105, 17], but a reliable technique for measuring the deflection distance of these 3D mode shapes in real time is either unaffordable or, otherwise unavailable. Many authors report the emergence of subharmonic Faraday waves as results from sub- or supercritical bifurcations[4, 31, 86], but none provides direct measurement of the amplitude response. Therefore until subharmonic zonal modes are discovered, amplitude response of subharmonic modes cannot be precisely quantified. In this study, subharmonic zonal modes are discovered and investigated. Direct measurement of the amplitude response

of these modes are presented. The amplitude response of subharmonic modes are further inferred from these results.

While harmonic and subharmonic modes are typical observations of resonating free surface waves, superharmonic resonance is extremely rarely reported among experimental studies. The few examples are Xu and Attinger[111] for a bubble in a microchannel and Batson *et al*[4] for Faraday waves. A curious question is raised: Why the rarity of superharmonics? More fundamentally, how can superharmonics be triggered?

In experiments, numerous non-zonal modes are observed to coexist with zonal modes. A drop's state of mode coexistence can be approached from either lower or higher forcing frequency. Moreover, the observed shape is apparently a linear combination of fundamental modes. Such mode mixtures are typical of experimental observation[17]. Similar mixing phenomena have been suggested by Vukasinovic *et al.*[105]: With an elevated forcing acceleration, an axisymmetric mode persists to mix with a lattice mode. Numerous works report similar phenomena for Faraday waves. For example, Batson *et al.* reported their observations of stable, co-dimension 2 points on the spectrum where two mixing modes may or may not be of the same harmonic type[4]. In experiments with viscous liquids, Rajchenbach *et al.* observed mixing star-shaped patterns whose behaviors are independent of container's shape[86]. As presented in §5.3, VPF theory adequately models linear mode mixing observations.

For vibrated sessile drops, the content is organized as follows. First the mode identification scheme is introduced, and observed mode shapes are related to Rayleigh-Lamb and Bostwick-Steen inviscid theories by ray-tracing simulations. Next the frequency response of various modes is compared to different theories, fol-

lowed by the investigation of the amplitude responses of different harmonic modes. Observed mixing modes are subsequently presented, and the comparison of these mixing phenomena with Bostwick-Steen viscous potential flow theory concludes the presentation of the experimental study with sessile drops.

CHAPTER 2

SESSILE DROPS I: MODE SHAPES

The content of sections 2.1 and 2.2 have been largely disseminated in Chun-Ti Chang, Joshua B. Bostwick, Paul H. Steen, and Susan Daniel, *Phys. Rev. E, 88:023015, Aug 2013.*

2.1 Overview

In experiments, a drop is mechanically vibrated on a solid substrate and its motion is acquired by high-speed imaging. A custom platform is designed for the experiments, as reported in Appendix A. The mechanical oscillation is generated by a function generator (model 33220A, by Agilent Technologies, Santa Clara, CA), amplified by a power amplifier (model CE2000, by Crown Audio, Elkhart, IN), and finally sent to a mechanical vibrator (model VTS-100, by Vibration Testing Systems, Aurora, OH). A high-speed camera (model RedLake HG-XL, by DEL Imaging Systems, Cheshire, CT) captures images of sessile drops. The optics used on the camera are a Sigma 180 F2.8 APO Macro lens and Vitacon 2X AUTO Teleconverter (NIF). The observation platform allows imaging top, left or right view, one at a time of an oscillating drop through integration of multiple mirrors (BB1-E02 Broadband Dielectric Mirrors, by Thorlabs, Newton, NJ). A schematic of the integrated hardware system is shown in figure 2.1.

A key aspect of the system that enables identification of higher drop modes is a platform that allows collection of two-dimensional spatial drop deformation by top-view imaging. In experiments, a drop is deposited on a functionalized glass substrate. Beneath the clear glass surface, a metal mesh with a 50-μm line width

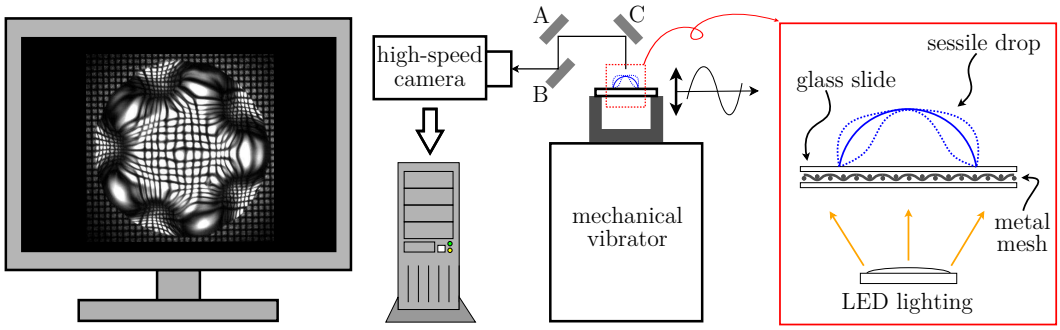

Figure 2.1: Schematic of imaging platform. Shown in the red (rightmost) box are the key components: mesh pattern and LED light source under the drop. Light rays from LEDs are refracted by the drops deforming surface, reflected into the high-speed camera by mirrors A, B, and C, and convey a deformed mesh pattern to the computer, thereby visualizing the deformation of the drop's surface. A signal generator (not shown) oscillates the surface sinusoidally in the direction perpendicular to the plane of the surface.

and 100μm $\times$100μm openings is affixed. This metal mesh is the key ingredient that allows the drop's deformation to be identified from the top view. The metal mesh, roughly 2cm$\times$2cm, is securely affixed beneath the functionalized surface by sandwiching with a second glass slide. White light emitted by light-emitting diodes (LED) from below the drop passes through woven metal mesh and is refracted by the drops surface. As the drop deforms, the mesh pattern is distorted, allowing clear visualization of the unique patterns of troughs and peaks on the drop surface. Refracted light is reflected by mirrors C, A, and B and finally transmitted to a high-speed camera (figure 2.1). By rotating the mirrors together by 90°, side views of a drop can also be obtained. This technique works better for drops for which light is refracted through only one liquid-gas interface. That is, it is better for sub- than superhemispherical drops. To clearly demonstrate observed mode shapes, the discussion in this chapter is restricted to subhemispherical drops only. Accordingly, results come from experiments with substrates of types A and C (cf. Appendix F). Type A substrates are capable of pinning drops within a 5-mm (diameter) circular region for drops up to 105° contact angle. Type C substrates are homogeneously

coated with APTES silane to achieve $60° \sim 80°$ contact angle for water drops. Whereas contact angles of drops on type A substrates are prescribed by drop volumes, those of drops on type C substrates require measurement from the side view of 20 μL drops. Contact angle measurements utilize static images of drops at the beginning and the end of each oscillation experiment. Details of surface preparation and characterization are provided in Appendix F.

In experiments, each sessile drop is excited by a single-frequency sine wave $A\sin(2\pi ft)$ with acceleration $a = (2\pi f)^2 A$. The range of forcing frequency f is $30 \leq f \leq 1100$Hz. The minimal driving amplitude is applied to induce the resonance modes: For zonal modes, peak accelerations range from 0.1g to 1g; while sectoral and tesseral modes require higher (>1g) accelerations. The highest acceleration among all experiments was 100g. The sessile drop itself consists of pure water of 20-μL volume. With respect to these experimental parameters, Reynolds (Re) and Bond (Bo) numbers are defined as

$$Re \equiv \frac{ar}{\omega\nu}, \qquad Bo \equiv \frac{\rho g r^2}{\sigma} \tag{2.1}$$

where a is the driving acceleration, r the footprint radius of drop (typically around 2.5 mm), ω the driving frequency in radians per second, ν is the kinematic viscosity of water, ρ the liquid density, g the gravitational acceleration, and σ the surface tension. Parameters of forcing signals are tabulated in table 2.1. The ranges of Re and Bo_g indicate that viscosity and gravity are less significant than surface tension.

(a) Physical parameters

Parameter	frequency(f)	amplitude (A)	acceleration (a)
Range	30∼1100 Hz	1∼430 μm	0.1∼100 g

(b) Dimensionless parameters

Frequency	Reynolds, forcing	Bond, gravity	Bond, forcing
$\omega \equiv 2\pi f(\rho r^3/\sigma)^{1/2}$	$Re \equiv ar/f\nu$	$Bo_g \equiv \rho g r^2/\sigma$	$Bo_a \equiv \rho a r^2/\sigma$
2.5∼100	$70 \sim 2000$	≤ 0.5	$0.1 \sim 80$

Table 2.1: Parameters of response and forcing by plane-normal displacement $A\sin(2\pi ft)$ where acceleration $a = (2\pi f)^2 A$.

2.2 Mode Identification

We shall catalog observed shapes according to the zonal, sectoral, and tesseral classification of spherical harmonics

$$r(\theta, \psi) = 1 + \epsilon P_k^l(\cos\theta)\cos(l\psi) \tag{2.2}$$

Modes are identified using the indices [k, l]. Examples of all three different types of modes are presented in figure 2.2. As can be seen from the snapshots in the bottom two rows in figure 2.2, distortion of the mesh pattern by zonal modes is axisymmetric to the eye. The [3, 3] and [5, 5] modes exhibit one single layer of azimuthal wave patterns with three and five peaks, respectively. For the tesseral modes, the [5, 3] mode possesses a Y pattern inside a triangle and the [7, 5] shows a star of five vertices in a pentagon. Notice that for all combinations of k and l, $k + l =$ even numbers, consistent with Lamb half-drops.

To further illustrate the scheme of mode identification, the image in column 1, row 3 of figure 2.2 is marked with red circles. These marks indicate the location of the nodal circles of the surface wave. According to the axisymmetric distortion of the underlying mesh pattern, the corresponding mode is zonal and possesses no azimuthal wave pattern, and hence a zero azimuthal wave number: $l = 0$.

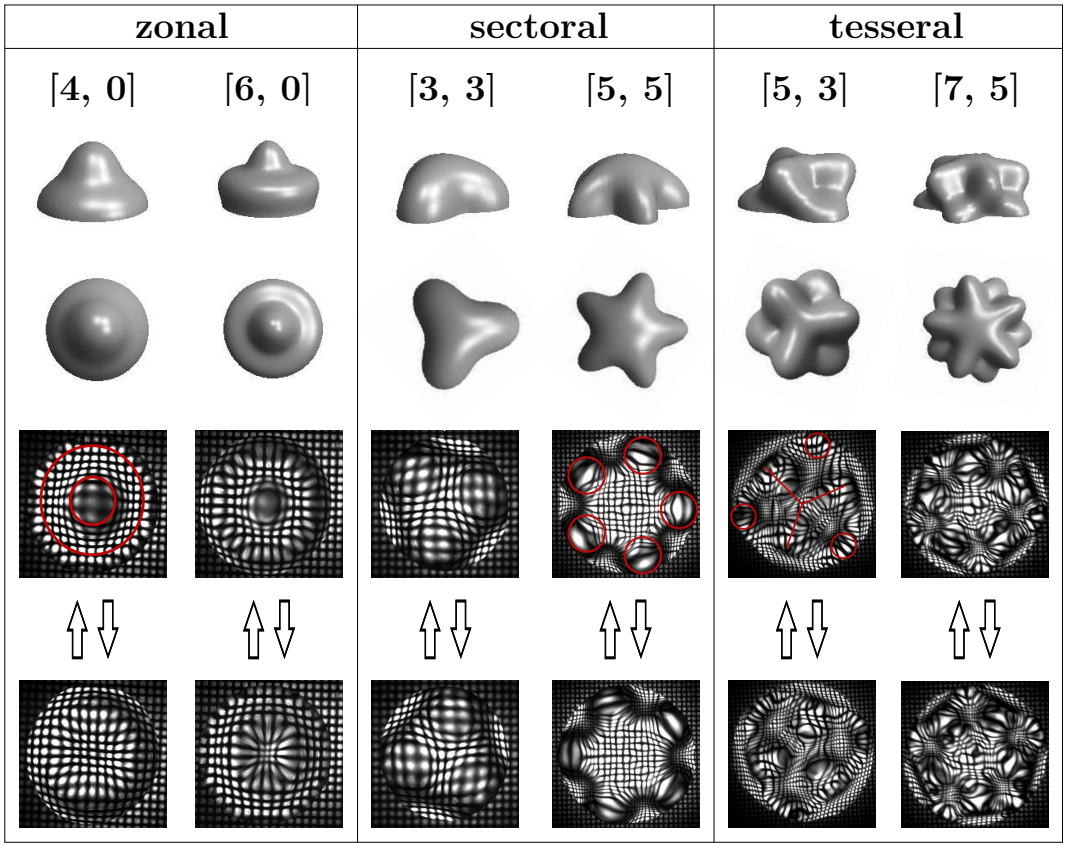

Figure 2.2: Examples of zonal, sectoral, and tesseral modes, where the numbers in the brackets are degree k and order l of the associated Legendre function , according to which the 3D surfaces are rendered in rows 1 and 2. Images in rows 3 and 4 are top-view snapshots from experiments. The two snapshots for each mode differ temporally by one half-period of oscillation.

In addition, because the two nodal circles intersect any diameter of the drop four times, or alternatively the surface disturbance exhibits four zero crossings, $k-l = 4$, we find $k = 4$. Therefore the zonal mode is identified as a $[k, l] = [4, 0]$ mode. This scheme facilitates the identification of any mode with an axisymmetric mesh deformation.

The sectoral and tesseral modes are identified based on their polygonal profiles from the top views. Two examples are provided in figure 2.2, columns 4 and 5. The similarity between the image marked with red circles in column 4, row 3, with the simulation, column 4, row 2, is apparent: Both exhibit a pattern of one single

star pattern with five vertices, which suggests that the former indeed results from the refraction of light across a deformed drop interface of the same qualitative geometry as the latter. Again, l is the azimuthal wave number that can be read off from the top view images by counting how many rotationally symmetric sectors a mode shape has. However, k cannot be obtained with the same intuitive visual approach. Instead, the image must be related to Eq. 2.2, which suggests that $k = l$ yields mode shapes with one single layer of azimuthal wave pattern. Since the three- and five-vertex star patterns correspond to $l = 3$ and $l = 5$, the sectoral modes in figure 2.2 are therefore $[3, 3]$ and $[5, 5]$.

Similarly, in figure 2.2, column 5, the observed image is associated with the simulated image of a [5, 3] mode by recognizing the marked "Y" pattern inside the outer triangle. Again, k cannot be obtained by counting geometric features of a mode shape. Instead, the image must be related to Eq. 2.2 to infer k. For the $[5, 3]$ mode, the "Y" pattern and the underlying triangle form two layers of triangular azimuthal waves. According to Eq. 2.2, the mode shape with one layer of triangle azimuthal wave is $[3, 3]$, that with two layers is $[5, 3]$, that with three layers is $[7, 3]$, etc. Therefore the mode with a "Y" pattern inside the outer triangle is identified as a $[5, 3]$ mode. Similarly on the rightmost column, the mode with a five-vertex star on a pentagon is a double-layer $l = 5$ mode. Since the single-layer five vertex star is $[5, 5]$, the double layer is $[7, 5]$. Notice the primary difference between experimental images and simulations: Drops in experiments exhibit an approximately circular footprint, while drops in simulations exhibit a non-circular footprint. This difference is clarified by the fact that experimental drops are observed to possess limited mobility of their contact lines, while the simulations assume completely mobile contact lines, as consistent with assumptions leading to Lamb half-drops.

With reference to Eq. 2.2, all modes with $k \leq 10$ and $l \leq 10$ (corresponding to the first 35 modes), and two additional zonal modes [12, 0] and [14, 0] are observed. Indices $[k, l]$ are useful as they establish the relationship to Lamb half-drops. Index l is the azimuthal wavenumber. However, k is not the polar wave number and, in fact, it is not intuitively related to the observed mode shape. Nevertheless, there is a simple relationship to the polar wave number where

$$n \equiv \frac{k-l}{2} + 1 \tag{2.3}$$

By this definition, n represents the number of layers of wave peaks for any given mode. For zonal modes, $l = 0$, which possess no azimuthal variations, n is the number of layers of polar wave peaks or troughs observable from the side views. Sectoral modes are those that have $l > 0$ and $n = 1$, which observationally means the modes with one single layer of azimuthal variation. All others (those with $l > 0$ and $n > 1$) are tesseral modes. Together with legends illustrating the (n, l) mode identification scheme, all 37 observed modes are cataloged in figure 2.3.

2.3 Ray-Tracing Simulation

To directly and intuitively compare observed mode shapes to predictions by [10], ray-tracing simulation is conducted with predicted mode shapes. Recall that mode shapes of oscillating drops are recorded in terms of the deformation of underlying mesh as 2D images, while the theory predicts 3D surfaces of drops. For bridging theory and experiments, the ray-tracing simulation takes a predicted mode shape as a lens and computes how an imaging pattern is deformed by refraction. As illustrated in figure 2.4, each pixel on an image plane forms an incident ray with the view point. The simulation traces where at the bottom of the lens an incident

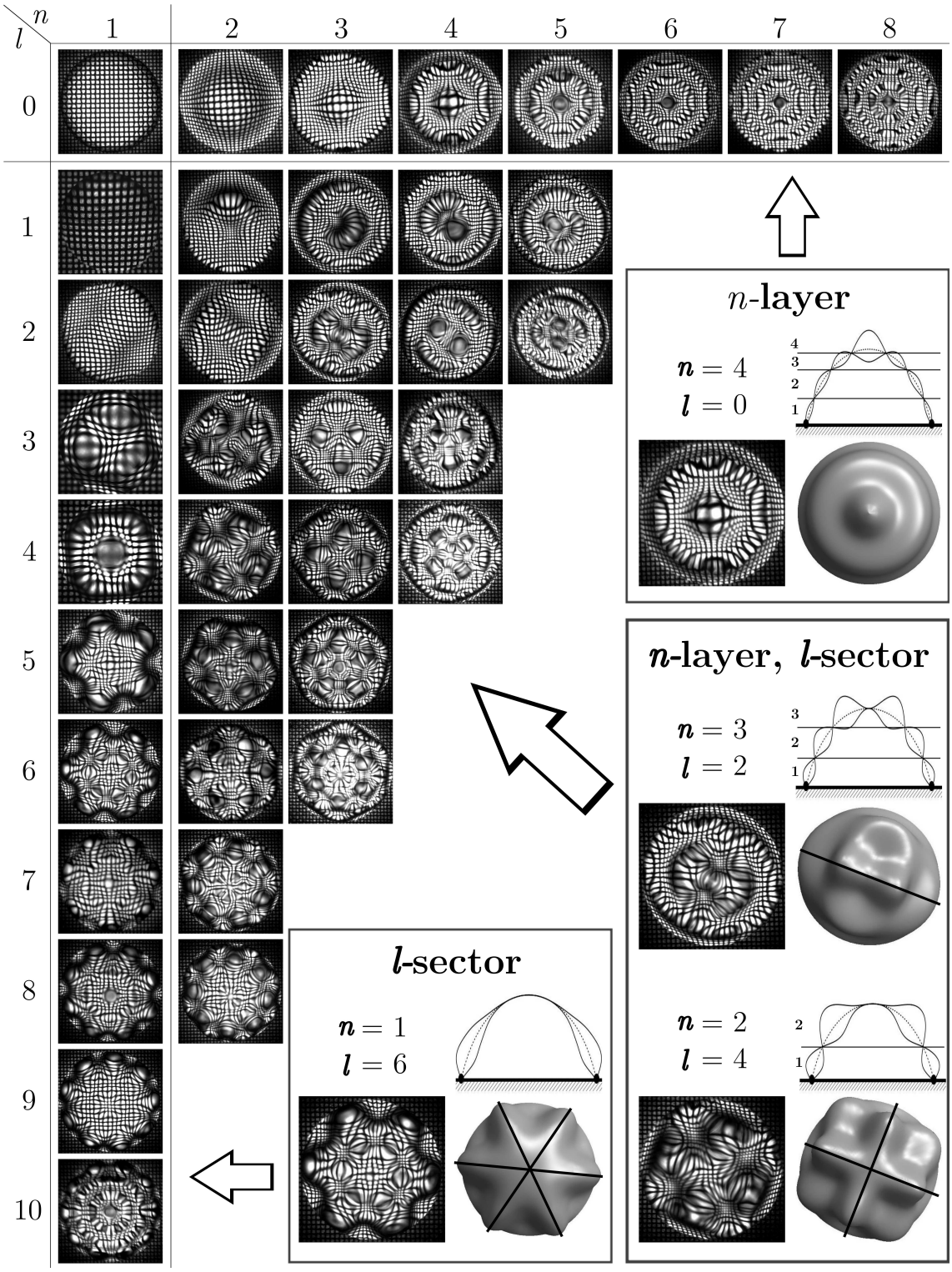

Figure 2.3: Summary of mode shapes observed in experiments. For reference, the picture for (n,l) = (1, 0) is the top view of a static drop. Modes are arranged by physical appearance: Zonal modes ($l = 0$) consist of layers of axisymmetric wave patterns, sectoral modes ($n = 1$) possess one single layer but multiple sectors of azimuthal waves, and tesseral modes exhibit multiple layers and sectors.

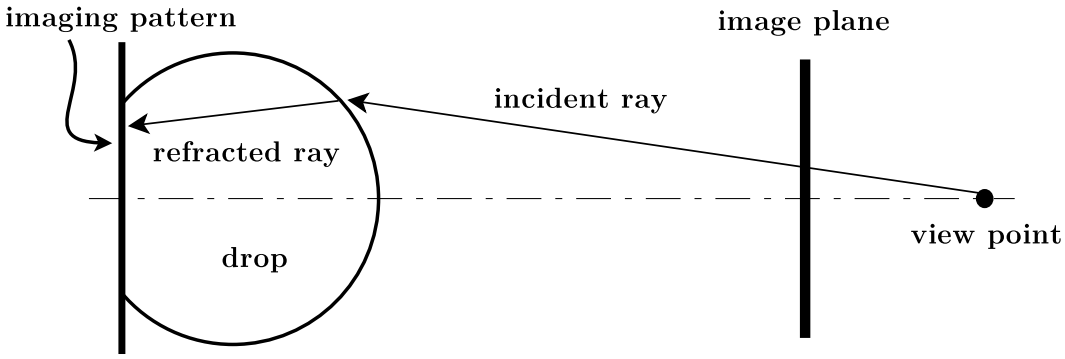

Figure 2.4: Schematics of ray-tracing simulation. On the image plane, each pixel forms an incident ray with the view point. The simulation traces where on the image pattern an incident ray is refracted to and renders the same color on the original pixel.

ray is refracted to. The color of the pattern at the point of incidence is copied to the originating pixel of the ray on the image plane. The same computation is repeated for every pixel on the image plane. For simplicity, no reflection at any interface is considered, and each incident ray is assumed to possess the same amount of energy (= brightness) as the refracted ray.

In practice, the simulation consists of two solvers: One for the intersection of an incident ray with the drop's surface, and the other for refraction across the surface. The scheme of intersection solver is illustrated in figure 2.5. For simplicity, the scheme is demonstrated with a static sessile drop. An incident ray L determines an w-z plane, which intersects the drop's surface in curve M. With P (north pole) and R (where curve M intersects contact line) as initial endpoints of M, the solver bisectionally approximates the coordinates of Q. Afterwards, the refraction solver calculates the normal vector at M. Denote coordinates of points on the drop's free surface as $\vec{P} = (P_r, P_\theta, P_\psi)$, where P_r, P_θ and P_ψ are components in the radial (r), polar (θ) and azimuthal(ψ) directions in a spherical coordinate system, and they are functions of θ and ψ. The normal vector $\vec{n}$ at $\vec{P}$ is obtained from the cross

product of tangent vectors[60] $\vec{u}_\theta$ and $\vec{u}_\psi$ in the θ and ψ directions as

$$\vec{n} = \vec{u}_\theta \times \vec{u}_\psi, \quad \vec{u}_\theta = \frac{d\vec{P}}{d\theta}, \quad \vec{u}_\psi = \frac{d\vec{P}}{d\psi} \tag{2.4}$$

The direction of the refracted ray is obtained from Snell's law. For each incident ray, the simulation completes when the intersection of the drop's bottom and the refracted ray is acquired.

Software verification is conducted for both solvers. For the intersection solver, results are examined by simply plotting and inspecting incident ray L, curve M and point Q on the w-z plane. For the refraction solver, two methods are implemented to calculate the normal vector $\vec{n}$ at Q: one computes $\vec{u}_\theta$ and $\vec{u}_\psi$ with analytical formuli, while the other approximates them by finite differencing, that is

$$\vec{u}_\theta = \frac{1}{2\delta}[\vec{P}(\theta+\delta,\psi) - \vec{P}(\theta-\delta,\psi)], \qquad \vec{u}_\psi = \frac{1}{2\delta}[\vec{P}(\theta,\psi+\delta) - \vec{P}(\theta,\psi-\delta)] \tag{2.5}$$

Consistency of results from the two methods confirms the integrity of computed $\vec{n}$. Note that verifying $\vec{n}$ is the most complicated testing step among others for implementing the ray-tracing simulation. Finally, computation of Snell's law is confirmed by manually repeating the same calculation at randomly selected points on the surface.

Based on the proposed algorithms, ray-tracing bridges the observations to predictions. Results for four representative modes are presented in figure 2.6 based on Rayleigh-Lamb [90, 62] (RL) and Bostwick-Steen inviscid[10] (BS inviscid) theories. Mode shapes from RL theory are spherical harmonics $P_k^l(\cos\theta)\cos(l\psi)$ in figure 1.1. Recall that all observed modes are identified by relating to those of $k + l =$ even. Observations differ from spherical harmonics mainly because of the pinned contact line of drops in experiments. An improved comparison is achieved by predicted mode shapes from BS inviscid theory, since pinning of contact line is

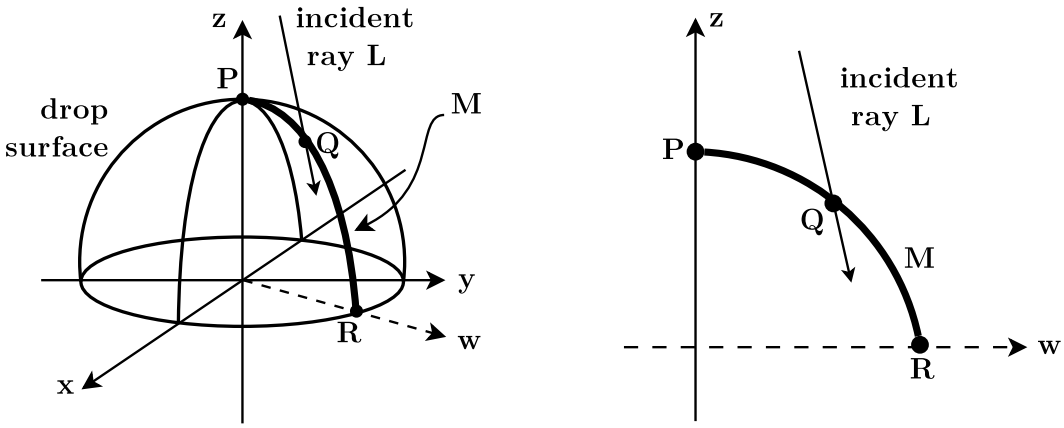

Figure 2.5: Schematics of intersection solver. Incident ray L lie on w-z plane, and the plane intersects the drop's surface in curve M. Starting with P and R as the initial endpoints of M, the intersection Q is bisectionally approximated.

considered. Take [5, 5] mode as an example. Although simulation based on both theories suggest a 5-vertex star pattern, prediction from BS inviscid theory yields a star in a circle. Overall, the simulation confirms that magnification of mesh pattern is due to local convexity of the drop's surface. The more obvious examples are the central part of [2, 0] mode and upper half of the [3, 1] mode. The peaks of the instantaneous mode shapes magnify the underlying mesh. For [5, 5] and [7, 5] modes, their peaks and troughs locally magnify and shrink underlying mesh, thereby resulting into one and two layers of pentagonal patterns in the simulation. Careful comparison of experimental and simulated images further suggests the co-existence of certain zonal modes with each mode: Close to the centers of both [5, 5] and [7, 5] modes, the mesh is only magnified in the experimental image but not in the simulation. The observation suggests ray-tracing simulation as a useful means of providing reference images for detecting mixing modes. Detailed discussion of mode mixing is presented in chapter 5.

Ray-tracing simulation has not been exhaustively explored, and several poten-

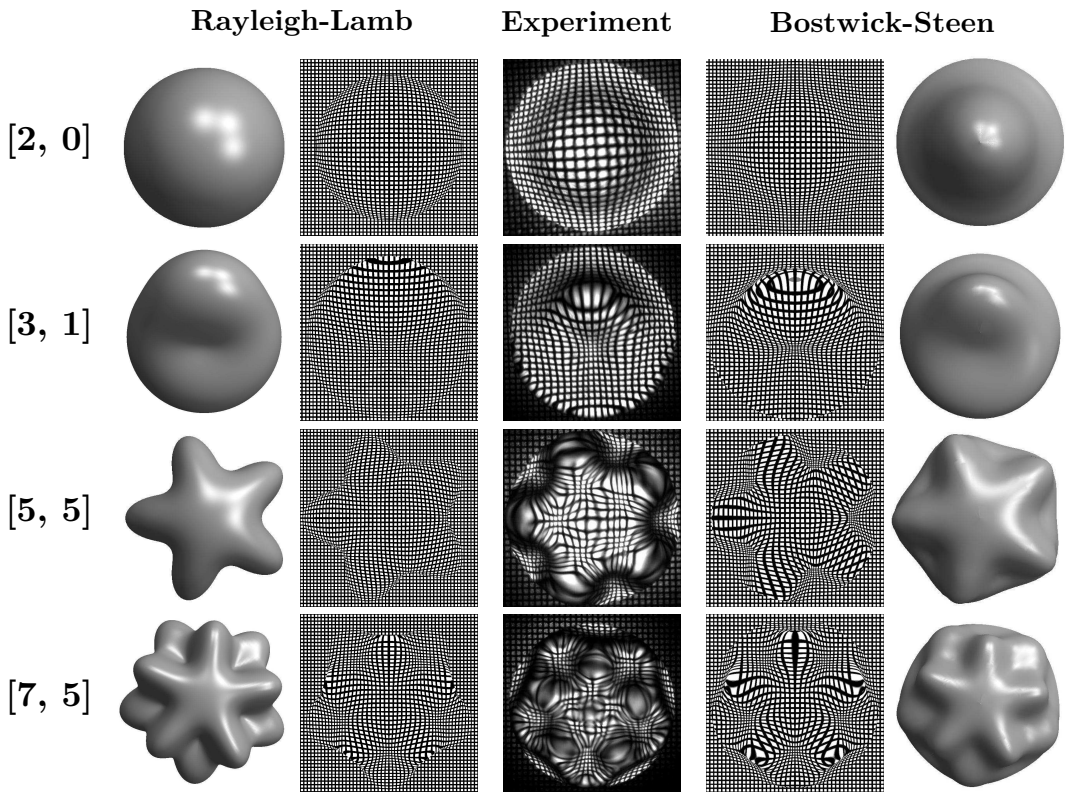

Figure 2.6: Comparison of mode shapes from experimental observation, ray-tracing simulation and theoretical prediction.

tial applications of the method are noticed. First of all, the method is applicable to free surface waves in a shallow and transparent liquid bath. Besides bridging experiment and theory, the simulation also provides reference for detecting mode mixing. More importantly, one may simulate any imaging pattern for visualizing surface waves. Therefore the simulation facilitates previewing the effectiveness of any candidate imaging pattern, thereby optimizing flow visualization in experiments to acquire images which are either human-readable, machine-readable[1] or suitable for other specific benchmarks.

[1]Such as images for particle image velocimetry (PIV)

CHAPTER 3

SESSILE DROP II: FREQUENCY RESPONSE

The content of this chapter has been largely disseminated in Chun-Ti Chang, Joshua B. Bostwick, Paul H. Steen, and Susan Daniel, *Phys. Rev. E, 88:023015, Aug 2013*.

3.1 Overview

To characterize the frequency response of vibrated sessile drops, resonance frequencies of observed modes are investigated from different aspects. From top-view images of oscillating drops, resonance frequencies are estimated (cf. Appendix D) for different modes. By comparing resonance and forcing frequencies of different modes, typical observations are qualitatively classified as harmonic or subharmonic modes: The former oscillates at the forcing frequency, while the latter at half of it. To quantitatively characterize these responses, estimated resonance frequencies are compared against (1) Rayleigh-Lamb (RL), (2) Bostwick-Steen inviscid (BS inviscid) and (3) Bostwick-Steen viscous potential flow (VPF) theories. The investigation first compares resonance frequencies of drops with $60^\circ \sim 80^\circ$ contact angles to RL and BS inviscid theories. Subsequently, resonance frequencies for drops with $35^\circ \sim 135^\circ$ contact angles are compared to both BS inviscid and VPF theories. These comparisons suggest the inadequacy of RL theory in the presence of substrate constraint, and the necessity of including viscous effects to predict appropriate bandwidths for various modes. Therefore these mode-wise comparisons suggest that VPF theory most appropriately describes the observations. Finally, combining probed resonance frequencies reveals the crossings modes on the fre-

quency spectrum as predicted by BS inviscid theory.

3.2 Comparison with theories

3.2.1 Experiments for drops with $60^\circ \leq \alpha \leq 80^\circ$

The characterization first probes resonance frequencies of vibrated drops with $60^\circ \leq \alpha \leq 80^\circ$ and then compares observations to Rayleigh-Lamb (RL) theory. Substrates homogeneously coated with APTES silane (type C substrates in Appendix F) are used in these experiments. The observations are technically made by random walks on the frequency-amplitude parameter space. For all modes, their resonance frequencies f_r are estimated from top-view image sequences as (cf. Appendix D)

$$f_r \approx f_s \times \frac{N_c}{N} \tag{3.1}$$

where f_s is the frame rate of high-speed imaging, N_c is the number of complete periods within N snapshots. Subsequently, f_r is compared to predictions of Eq. 3.2:

$$f_t = \sqrt{\frac{\sigma}{3\pi \times 2m} k(k-1)(k+2)} \tag{3.2}$$

where $\sigma = 72mN/m$ and $m = 20$mg are the surface tension and mass of 20μL pure water drops in these experiments, respectively, and k as defined in Eq. 1.1. The comparison includes all modes of $k \leq 10$, $l \leq 10$ but [10, 4], which is never observed in experiments with type C substrates.

3.2.2 Rayleigh-Lamb theory, $60^\circ \leq \alpha \leq 80^\circ$

The RL theory describes free oscillation of spherical drops in space, while in experiments the drops are sessile and mechanically vibrated. Nonetheless, it is of interest to determine how well the classical theory can capture the observed resonance frequencies of sessile drops. To compare the sessile drop equivalent to the Rayleigh and Lamb half-drop, ideally, the sessile drop should be perfectly hemispherical (90° contact angle) with freely moving contact lines (no pinning). The experiments would then correspond most closely to the theory and the estimated resonance frequencies of sessile drops with mass m could be compared to eigenfrequencies of spherical drops with mass $2m$. Notice here the discussion is restricted to undisturbed drops that are subhemispherical. A subtle point is then how to account for the mass m to fairly compare to the Lamb prediction.

One way to address this point is to remove the capillary time scale $\sqrt{3\pi \times 2m \div \sigma}$ in Eq. 3.2 by normalizing frequencies. For experimental data of zonal modes, the average frequency $\bar{f}$ of [2, 0] mode in all observations is calculated first. The ratio q of observed resonance frequencies to $\bar{f}$ is subsequently computed. For theoretical predictions of zonal modes, the same ratios q are calculated by normalizing all predicted eigenfrequencies by that of the [2, 0]. The ratios q are plotted together in figure 3.1(a). From the figure, ratio q lie above the data points for $k \geq 10$. Because the normalization removes capillary time scale, the choice of volume, density, and surface tension no longer affects the result. Only the predicted scaling is compared to the scaling trend of experiments. According to figure 3.1(a), the theory mismatches experiments for zonal modes as predictions overshoot observations.

Comparison for sectoral and tesseral modes further confirms the inadequacy of

the theory. The same normalization procedure for zonals is used. For sectorals, the experimental and predicted eigenfrequencies are normalized by the average of the frequencies of the observed [2, 2] mode and by the Lamb [2, 2] frequency, respectively. Note that the [2, 2] eigenfrequency is the first nonzero Lamb frequency. For tesseral modes, the frequencies are all normalized by those of the $l = 1$ modes, i.e., [3, 1], [5, 1], [7, 1], and [9, 1], respectively. The results are presented in figure 3.1(b)-(d). As the RL theory overshoots the experimental data, it is inadequate for describing behaviors of these modes. Recall the fundamental distinction between theory and experiments: The Lamb half-drops correspond to a sessile drop with completely free contact lines. However, in reality, these drops exhibit nearly fully pinned contact lines. The anticipated impact of this condition is to spread the experimentally observed frequencies for each mode as well as to lower the mean frequency.

3.2.3 Bostwick-Steen Inviscid Theory, $60^\circ \leq \alpha \leq 80^\circ$

We now compare the experimental data with Bostwick-Steen inviscid (BS inviscid) theory[10]. The theory considers free oscillation of an inviscid sessile drop with prescribed contact angle and contact-line mobility. The spherical-cap base states are parametrized by the scaled volume or, alternatively, the equilibrium contact angle. In either case, there is a one-parameter family of base states. The contact-line constitutive behavior is characterized by a mobility parameter with two limiting cases: the fully mobile contact line and the pinned contact line. As little contact-line motion is detectable in our experiments, predictions are all based on pinned contact lines. For each mode of indices [k, l], a pair of eigenfrequencies are calculated based on the experimental parameters of liquid volume (20μL), sur-

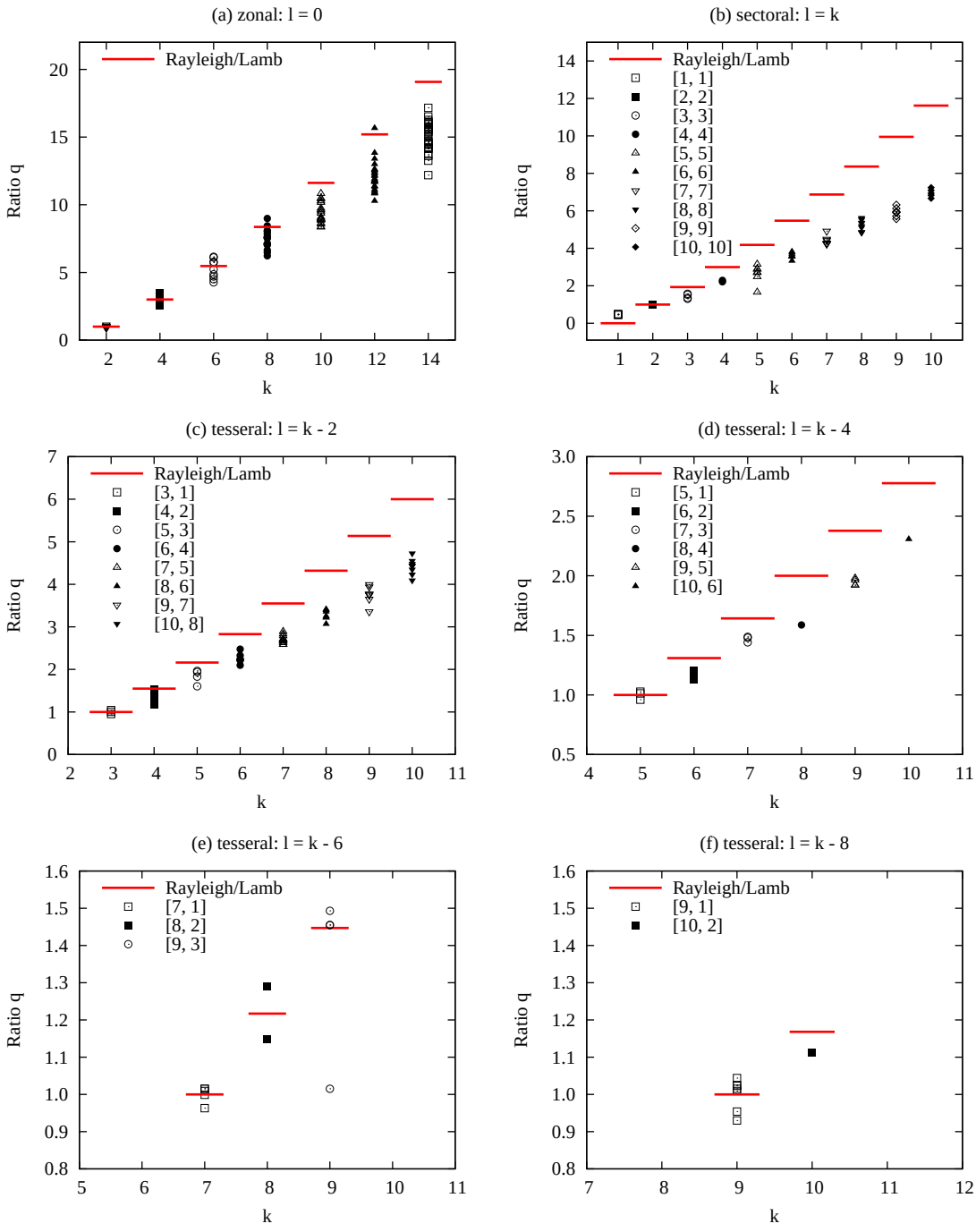

Figure 3.1: Comparison of frequency scaling prediction by Rayleigh[90] and Lamb[62] for (a) zonal, (b) sectoral, (c-f) tesseral modes. According to the overshooting trend of the predicted frequency scaling, the theory is inadequate for describing experimental observations.

face tension (0.072 N/m), density (1000 kg/m^3), and pinned contact lines. The two eigenfrequencies correspond to maximal and minimal contact angles observed for a drop before and after the oscillation, respectively. These bounds, based on the observed contact angle spread, are represented by the solid lines in Figs. 3.2. Note that since BS inviscid theory explicitly considers both the presence of a substrate and a drop's contact angles, direct comparisons are conducted in physical units without frequency normalization. Results for zonal modes are presented in figure 3.2(a). In contrast to the trend of uniform overestimation by RL theory, the BS inviscid theory reasonably matches with experimental results: Predicted frequencies fall within the lower portion of the experimental data. Because of the neglect of viscous effects, bandwidths of predicted eigenfrequencies are small and prediction cannot be expected to capture a wide spread of frequencies. A similar comparisons for sectoral and tesseral modes are presented in figure 3.2(b)-(d). Reasonable agreement is noted. Among the observed modes, the ones with fewer layers of azimuthal variations exhibit a better match between experiment and prediction. But even for the higher modes, the predictions fall within the spreading of experiment data, therefore suggesting a credible consistency between the experiments and BS inviscid theory.

3.2.4 Experiments for $35^\circ \leq \alpha \leq 135^\circ$

As BS inviscid theory appears promising in comparisons already presented, the theory is further tested for selected modes in a broader range of contact angles. The experiments are facilitated by substrates with pinning sites. The pinning sites are the more hydrophilic regions on a surface and can be created with either contrasting surface chemistry, presence and absence of physical patterns, or the

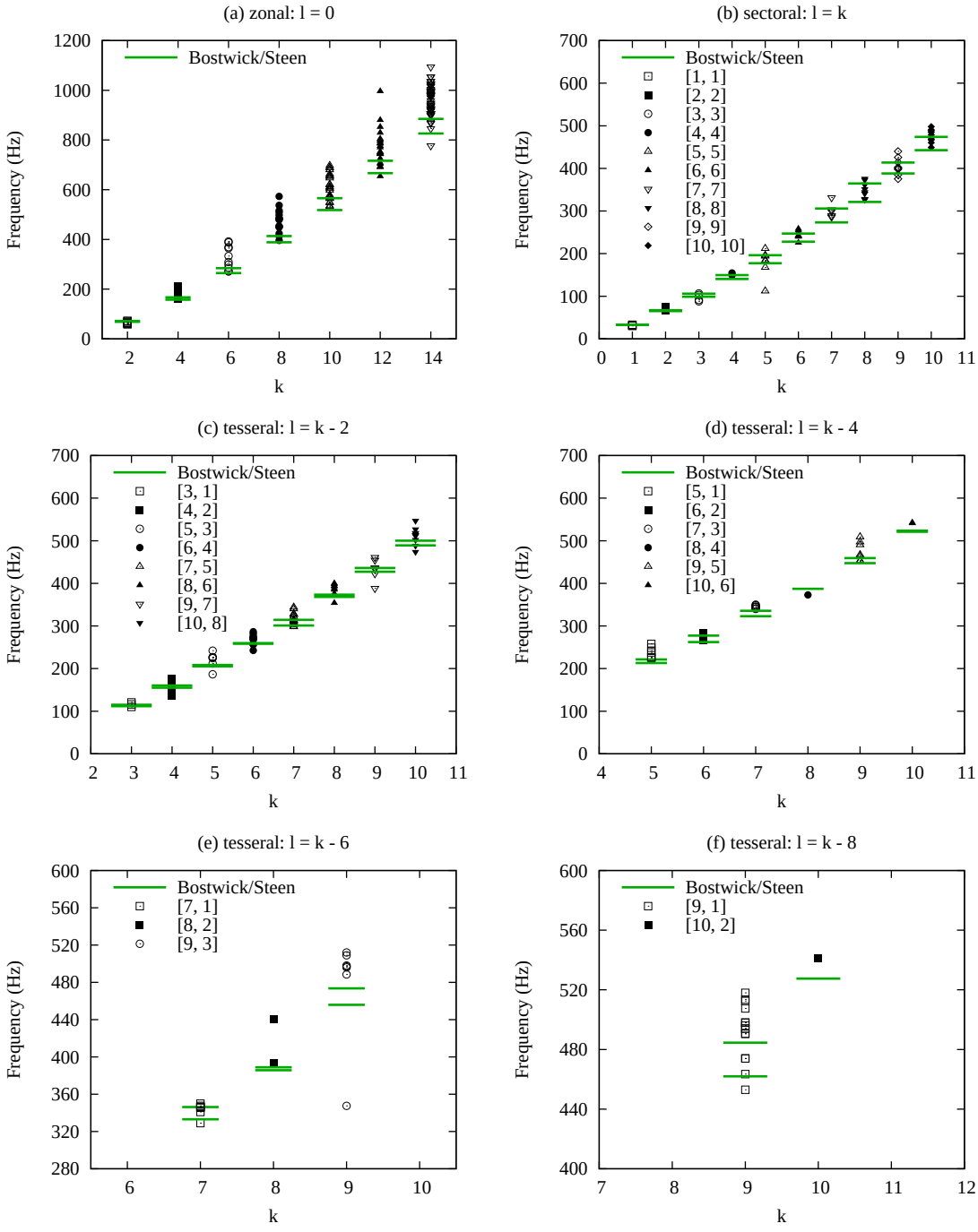

Figure 3.2: Comparison of frequency scaling prediction by Bostwick-Steen inviscid theory[10] for (a) zonal, (b) sectoral, (c-f) tesseral modes. All predicted frequencies fall within the spreading of experimental data. Accordingly, the theory adequately captures experimental observations.

combination of both. With the same fixed footprint, contact angles of drops can simply be controlled by prescribing the volume. The experiments here utilize substrates of types A and B (cf. Appendix F) to respectively achieve contact angles $35^\circ \leq \alpha \leq 102^\circ$ and $105^\circ \leq \alpha \leq 135^\circ$. To accommodate different footprint radii of pinning sites on type A and B substrates, estimated resonance frequencies f_r are normalized as

$$\omega = f_r \times \sqrt{\frac{\rho r^3}{\sigma}} \times 2\pi \tag{3.3}$$

where ρ ($= 1000\ kg/m^3$) and σ ($= 72mN/m$) are the density and surface tension of pure water, respectively, and r ($\approx$ 2.5mm and 1.37mm for type A and B substrates, respectively) the footprint radii of drops.

Resonance frequencies of zonal modes are probed by observing side views of drops and recording frequencies with maximal deflection. Technically, identification of the frequency is based on visual inspection of real-time video stream from the high-speed camera. The experimental protocol is depicted in figure 3.3. In practice, the forcing amplitude is first increased (a $\rightarrow$ b in figure 3.3), and a frequency scan at the fixed forcing amplitude (b $\rightarrow$ c $\rightarrow$ d in figure 3.3) iteratively locates the frequency maximally deflects the drop. The experiments are conducted only on type A slides, and forcing accelerations are less than 4g in these experiments.

Frequency responses of non-zonal modes are probed differently. In contrast to zonal modes, amplitude of non-zonal modes cannot be precisely quantified from either top or side view. Consequently, the forcing frequency leading to maximum deflection cannot be identified. Therefore the frequency response of a non-zonal mode is investigated in terms of the maximal frequency range (bandwidth) it persists. The experimental protocol is depicted in figure 3.4. In practice, the forcing

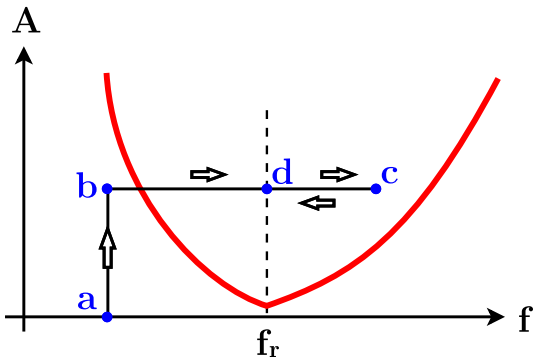

Figure 3.3: Schematics of probing the resonance frequency of a zonal mode. Parameters f and A are forcing frequency and amplitude, respectively. The curve form an Arnold tongue, which represent the bandwidths of two modes at different forcing amplitudes. In practice, the forcing amplitude is first increased ($a \to b$), and the frequency scan proceeds at fixed amplitude to iteratively locate ($b \to c \to d$) the resonance frequency f_r.

amplitude is first increased to the prescribed setting (a $\to$ b). The forcing accelerations range from 10g to 35g. The forcing frequency is then tuned manually, roughly 1Hz/s. Once a mode appears, the forcing frequency is decreased to probe the lower limit f_m (b $\to$ c), below which the mode suddenly disappears. Alternatively, from the same starting frequency (at point a in figure 3.4), the frequency is increased to probe the upper limit f_M (b $\to$ d), beyond which the mode vanishes. Emergence and disappearance of modes are visually inspected from a drop's top view via the high-speed camera. Bandwidths for $k = 5$, 7 and 9 modes are probed.

In experiments, the emergence of modes are found to depend strongly on contact angle of drops. For example, as shown in figure 3.5 and 3.6, flat drops ($\alpha < 50°$) cease to exhibit [5, 5], [7, 5] and [7, 7] modes, and any attempt to generate these modes by increasing driving amplitude ends up ejecting satellite droplets without disturbing the drop's circular footprint. Since features of sectoral modes reside along the contact line, the absence of [5, 5] mode is suspected to result from the enhanced influence of a pinned contact line on the deflection of the free surface.

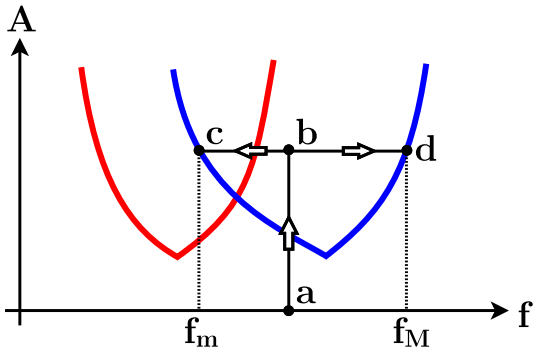

Figure 3.4: Protocol schematic of probing the bandwidth of a non-zonal mode. Parameters f and A are forcing frequency and amplitude, respectively. The curves of the same color form two Arnold tongues, which represent the bandwidths of two modes at different forcing amplitudes. In practice, the upper and lower limits of the mode's bandwidth are probed by a downward (a $\rightarrow$ b $\rightarrow$ c) and an upward (a $\rightarrow$ b $\rightarrow$ d) frequency scan at the same forcing amplitude.

With $\alpha = 90° \sim 100°$, multiple modes mix and/or compete, among which sectoral modes typically dominate. This explains the significantly reduced bandwidths of tesseral modes [5, 1], [5, 3], [7, 1], [7, 3] and [7, 5]. Further increasing contact angle separates spectra of modes. For superhemispherical drops, the patterns of [5, 3], [5, 5], [7, 5] and [7, 7] remain recognizable. However, identification of [5, 1] and [7, 1] is difficult, because only the topmost peak is clearly observable from the top view yet the peak resembles that of a zonal mode, while features below a drop's equator cannot be identified from any direction. Hence the absence of these $l = 1$ modes for $\alpha > 110°$. For [7, 3], it is suspected that the mode either requires a much higher acceleration to excite, or it simply gets scavenged by others. For all experiments seeking $k = 7$ modes of superhemispherical drops, no clear triangular pattern has been observed at any contact angle.

Similar behaviors are observed for $k = 9$ modes. As presented in figure 3.7, flatter ($\alpha < 50°$) drops don't exhibit [9, 9] and [9, 7] modes, and only [9, 5], [9, 7] and [9, 9] are observed for $\alpha > 110°$. The absence of [9, 1] and [9, 3] are speculated

to result from similar causes for [7, 1] and [7, 3]. Note that the observations of [9, 5], [9, 7] and [9, 9] modes not only serve to test the theories, but also demonstrate the complete reversal of the order of their spectra, as discussed in section 3.3.

3.2.5 Bostwick-Steen Inviscid Theory, $35^\circ \leq \alpha \leq 135^\circ$

Resonance frequencies of zonal modes from experiments are first compared to BS inviscid theory. As shown in figure 3.5(a), the predictions reasonably match observations for $60^\circ \leq \alpha \leq 100^\circ$ but deviates for flatter ($\alpha < 60^\circ$) drops. In addition, the deviation exacerbates for higher zonal modes. Accordingly, the inadequacy of BS inviscid theory is speculated.

The speculated inadequacy of inviscid theory is further tested with non-zonal modes. Recall that the resonance frequency f_r of a non-zonal mode is probed in terms of the mode's bandwidth $f_m \leq f \leq f_M$. In figure 3.5(b)-(d) and 3.6, bandwidths for $k = 5$ and $k = 7$ modes are compared to the BS inviscid theory. Similar to the comparison for zonal modes, a reasonable match is achieved around $70^\circ \leq \alpha \leq 100^\circ$. In addition, agreement with inviscid theory deteriorates for higher wavenumber (larger n) and flatter droplets. Results for $k = 9$ modes are presented in figure 3.7. Again, $60^\circ \leq \alpha \leq 80^\circ$ remains where the inviscid theory and experiments best agree, and any deviation increases for flatter drops and modes with larger n. Although the cause of the theory's deviation from experiments is unclear, a growing importance of viscous effects in these cases is speculated to be the main suspect. The speculation is motivated by the disappearance of [5, 5], [7, 7] and [7, 5] modes for flatter drops. For flatter drops, liquid-solid surface takes on a larger proportion of the total surface area, and therefore possibly the more profound the viscous effect on this interface becomes. In addition, non-zonal modes

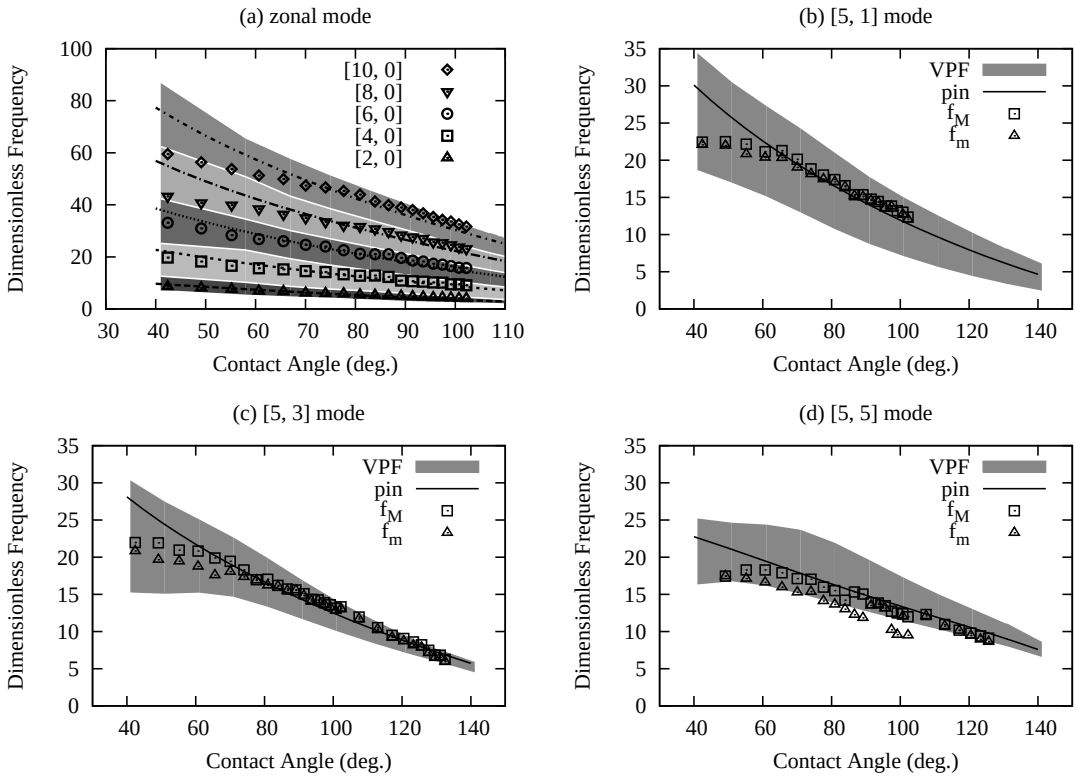

Figure 3.5: Comparison of theories and experiments for (a) zonal modes and (b)-(d) modes of $k = 5$. Shadows are predicted bandwidths from VPF theory. Curves are predicted resonance frequencies from the inviscid theory. Symbols of f_M and f_m correspond to max. and min. observed resonance frequencies of each mode. For both theories, an overall matching of predictions and observations is found for $\alpha > 60°$. Except for [2, 0] and [4, 0] modes, predictions based on the inviscid theory deviates noticeably from observations for $\alpha < 60°$. Due to difficulty of mode identification, [5, 1] mode is absent for $\alpha > 105°$. The bandwidths provided by the VPF theory adequately accommodate all observed frequencies/bandwidths.

of these relatively flat drops require a forcing higher than 30g to excite. Possibly due to such tremendous forcing, strong nonlinearity is induced in experiments but not considered in the theory, and hence their mismatch. To test these hypotheses, the observations are compared to Bostwick-Steen viscous potential flow theory which includes weak viscous effects.

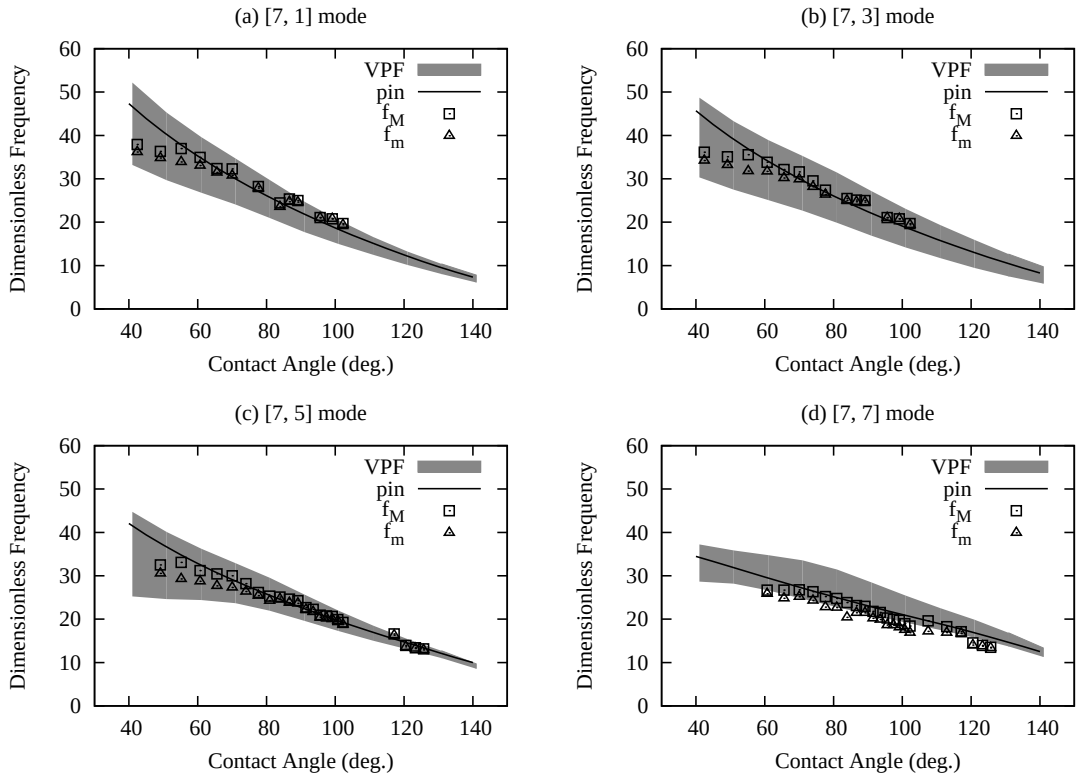

Figure 3.6: Comparison of theories and experiments for $k = 7$ modes. Shadows are predicted bandwidths from VPF theory. Curves are predicted resonance frequencies from the inviscid theory. Symbols of f_M and f_m correspond to max. and min. observed resonance frequencies of each mode. An overall matching is found again for $\alpha > 60°$. Whereas [7, 7] and [7, 5] disappears for flatter drops, [7, 3] and [7, 1] are not identified $\alpha > 110°$, either due to mode mixing or difficulty of mode identification. Between the inviscid theory and experiments, the same mismatch as that for $k = 5$ modes is found for flatter drops. Based on forcing case D, the VPF theory predicts adequate bandwidths that more precisely matches with experimental observations.

3.2.6 Bostwick-Steen VPF Theory, $35° \leq \alpha \leq 135°$

To test whether viscous effects invalidates BS inviscid theory for the broader range of contact angles, experiments are compared against Bostwick-Steen viscous potential flow (VPF) theory. Given (1) azimuthal wave number l, (2) static contact angle α, and (3) type of forcing, the VPF theory predicts the mode shape and response amplitude of a drop as a function of the frequency. For (3), the theory

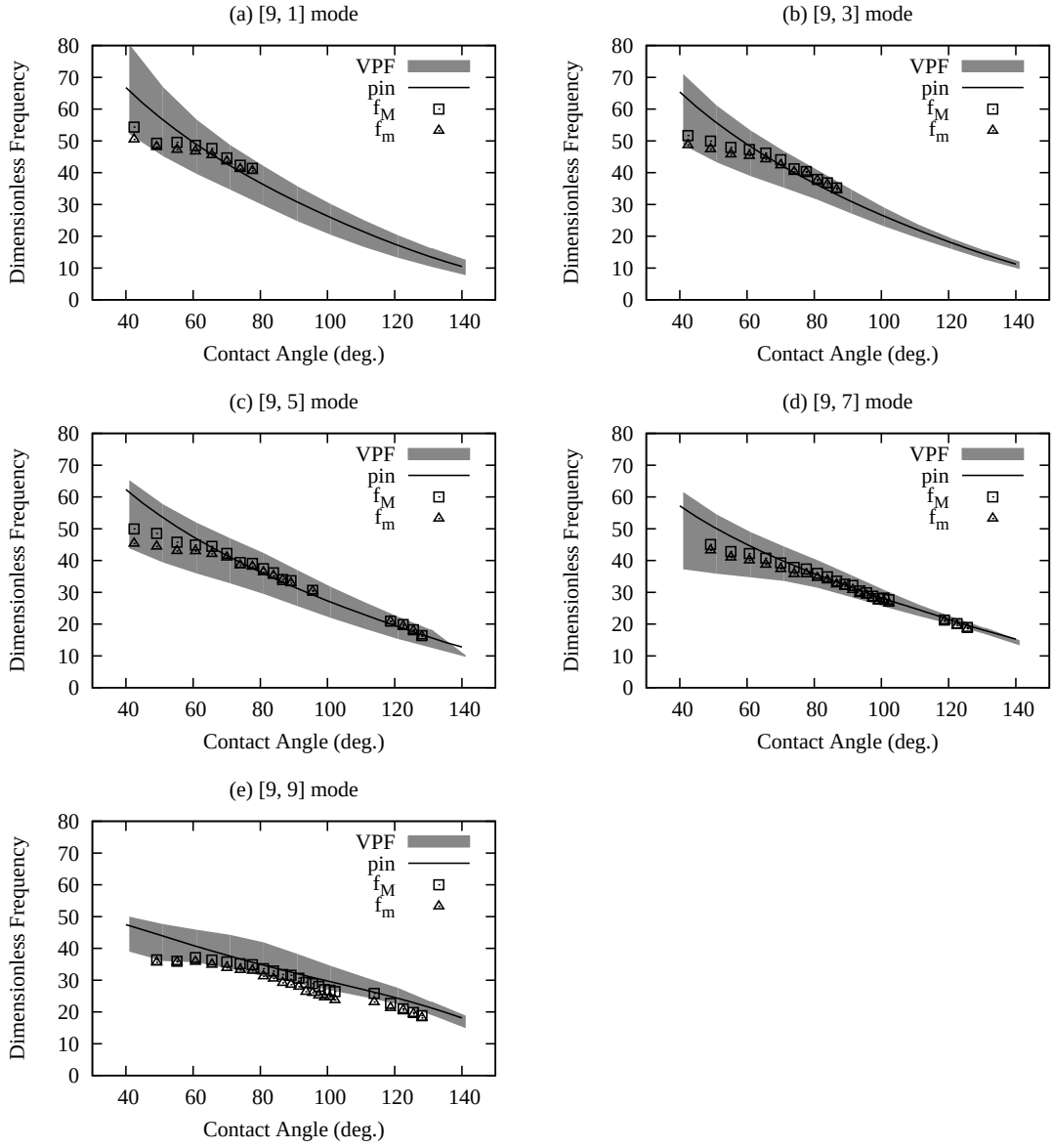

Figure 3.7: Comparison of theories and experiments for modes of $k = 9$. Curves and shadows are predictions from BS inviscid and VPF (case D) theories, respectively. Symbols of f_M and f_m are max. and min. observed resonance frequencies of each mode. Similar to $k = 5$ and $k = 7$ modes, [9, 9] and [9, 7] modes are absent for $\alpha < 50°$, and [9, 1] and [9, 3] submerge among others for $\alpha > 110°$. Similar extents of agreement between theories and experiments to those in figure 3.5 and 3.6 are found again. The inviscid theory matches experiments for $\alpha > 60°$ but mismatch for $\alpha > 60°$. The VPF theory more adequately captures the observed bandwidths for $k = 9$ modes.

	uniform	vertical	horizontal
force	A (red)	B (green)	E
acceleration	D (black)	C (blue)	F

Table 3.1: Different cases of forcing in the VPF theory

provides six cases for consideration, as tabulated in table 3.1. Only cases A, B, C and D are considered, since no drop is horizontally oscillated. Viscous effects are incorporated in terms of an Ohnesorge number $\epsilon \approx 0.0024$, which is based on water drops' dynamic viscosity $\mu = 10^{-3}$ Pa·s, surface tension $\sigma = 72$mN/m, density $\rho = 1000$kg/m^3 at 20°C and footprint radius $r = 2.5$mm in experiments. Note that the comparison here also tests which of the four forcing cases matches experiments the best, and the result is case D. Therefore the comparison for case D of VPF theory against experiment is presented in figure 3.5, 3.6 and 3.7. Comparison for other cases are shown in figure 3.9 and 3.10.

The forcing and viscous effects in VPF theory need to be properly interpreted. Because the forcing is not parametric and the theory remains linear, all modes are harmonic and involve neither bifurcation nor hysteresis. The appropriate physical interpretation of the 'forcing' is the internal variation of pressure or potential of an oscillating drop instead of a real, external excitation. Although little, viscous effects are included in terms of an Ohnesorge number ϵ. A small yet nonzero ϵ is necessary to ensure boundedness of resonance amplitudes, which facilitates definition of bandwidths based on a target percentage of amplitude.

The bandwidth of a mode is defined in terms of percentage peak-to-valley amplitude difference. Suppose a resonance peak of a particular mode locates at dimensionless frequency $f = f_1$, amplitude $A = A_1$, and let the closest local minima be at $(f, A) = (f_2, A_2)$ to the right (i.e. $f_2 > f_1$) and (f_3, A_3) to the left

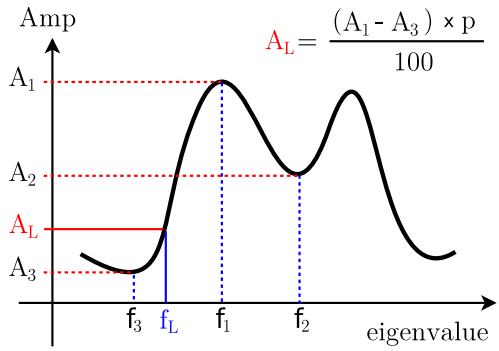

Figure 3.8: Schematic illustrating the definition of p-% bandwidth for a resonance peak.

($f_3 < f_1$). The p-% target amplitudes A_r and A_l are defined as

$$A_R = A_2 + \frac{p}{100} \times (A_1 - A_2), \quad A_L = A_3 + \frac{p}{100} \times (A_1 - A_3)$$

The scheme (for A_L and f_L only) is illustrated in figure 3.8. The frequencies f_R and f_L respectively associated with A_r and A_l are linearly interpolated within $f_3 < f < f_1$ and $f_1 < f < f_2$ on the response curve. The p-% bandwidth is compared to experimental data in terms of f_r and f_l. Note that according to the definition, $A_L = A_R \Leftrightarrow A_2 = A_3$, and typically $A_L \neq A_R$. The lower limits of bandwidths for [2, 0] and sectoral modes are frequencies at 2% peak amplitudes. Otherwise, a 0-% bandwidth is adopted in this chapter.

Results of comparing VPF theory (case D) against experiments are shown in figure 3.5, 3.6 and 3.7. In contrast to the BS inviscid theory, VPF theory case D provides adequate bandwidths that accommodate the observed resonance frequencies even for flat drops. Predicted bandwidths of zonal modes overlap all observed resonance frequencies. For $k = 5$ modes, a reasonable agreement is achieved even for $\alpha < 60°$. Although for [5, 5], [7, 7] and [9, 9] modes, predicted and observed bandwidths do not overlap completely, they follow roughly the same trend. The mismatch is very likely due to the hysteresis and bandwidth broadening of modes observed in experiments, as the VPF theory models neither. Again, VPF theory

is linear while excited sessile drops resemble nonlinear parametric oscillators (cf. chapter). Hysteresis have been observed in our experiments (cf. figure 3.14 in §3.3). However, the VPF theory is linear and our definition of bandwidth further truncates hysteresis by splitting response curves at the valleys ($p = 0\%$). In addition, the predicted bandwidths are independent of the driving amplitude, but eigenmodes of drops in our experiments exhibit broadening bandwidths with driving amplitudes. As drops are excited by 25$\sim$35g, modes are expected to survive a broader bandwidth than predicted. These differences possibly result in the mismatch for these sectoral modes within $80^\circ \leq \alpha \leq 100^\circ$.

Additional comparisons of VPF theory and experiments are presented in figure 3.9 and 3.10. According to the results, predicted bandwidths from cases A and B are too narrow for flat drops ($\alpha \leq 60^\circ$), while predictions from case C agrees with experiments equally well as those from case D. The different extents of agreement suggest that drops experience forcing as accelerations. Although cases C and D compare equally well in results already presented, the latter also matches observed mode mixing (cf. §5.3) better than the former. Note that the zig zag of predicted bandwidths are simply due to the fact that the calculated response curves are sampled differently. Smoothing the original response curves can effectively remove these artificial defects. No preprocessing is conducted for response curves of cases A, B and C since these predictions exhibit clear deviation from observations.

The comparisons need to be properly interpreted. For each mode, its response is probed as a function of driving acceleration a, driving frequency f and the drop's static contact angle α. Increasing acceleration is observed to broaden bandwidths of modes in experiments. Therefore it is possible to experimentally manipulate

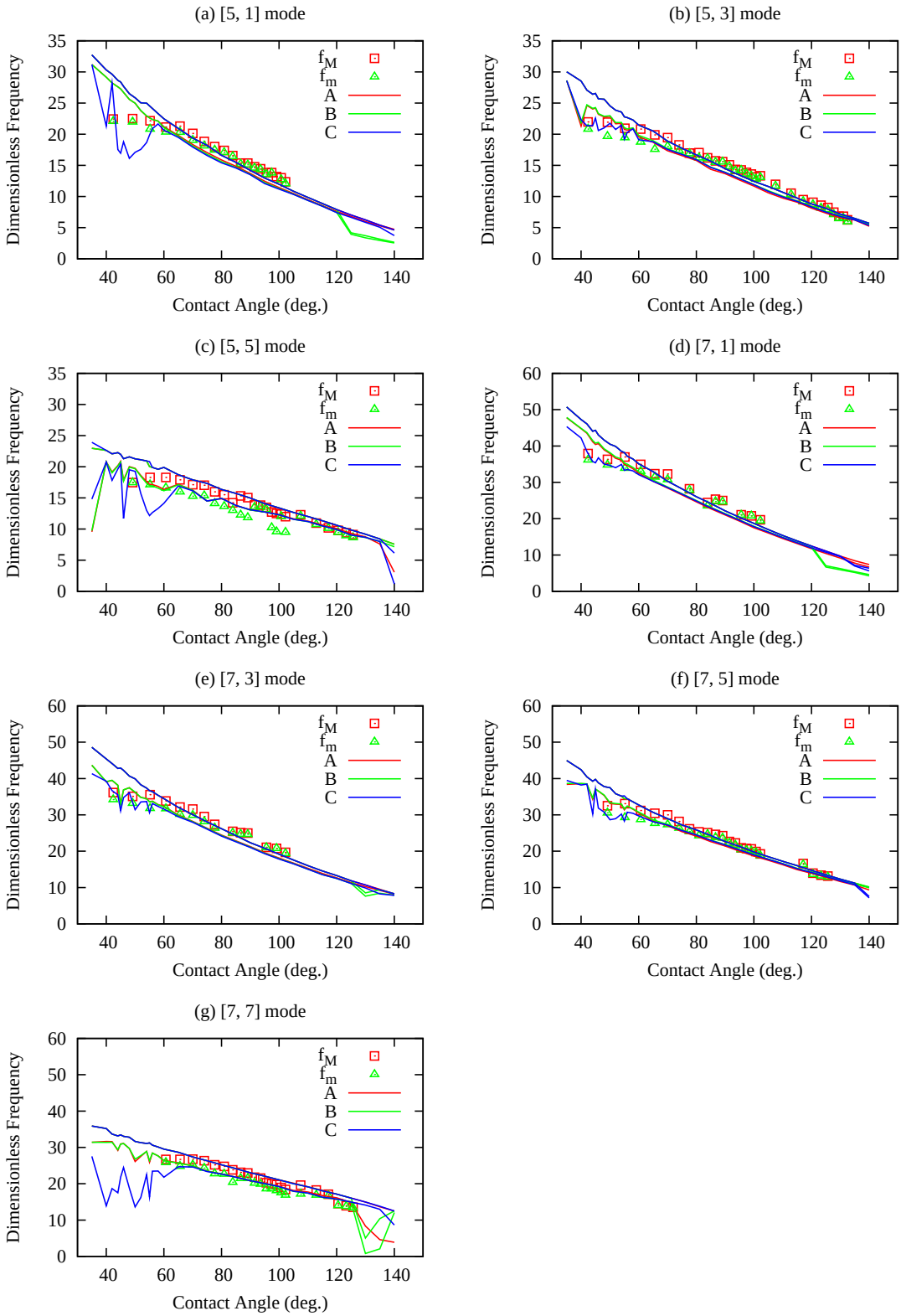

Figure 3.9: Comparison of VPF theory with experiments for $k = 5$ and $k = 7$ modes. Cases A and B cannot predict adequate bandwidths to match observations. Since case C achieves a similar extent of matching as case D, external forcing is experienced by drops as an acceleration.

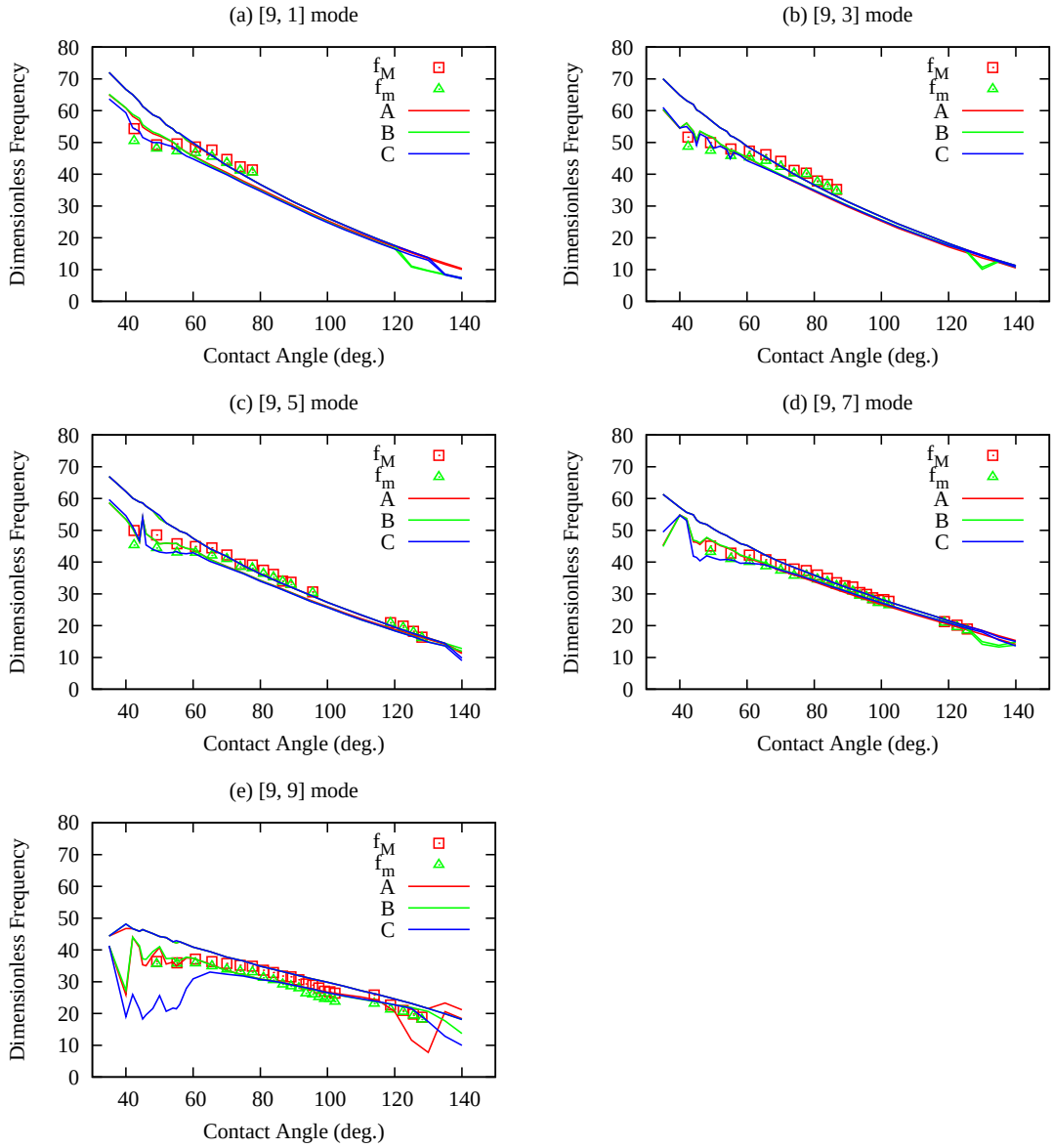

Figure 3.10: Comparison of VPF theory with experiments for modes of $k = 9$. Consistent with figure 3.9, case C matches experiments equally well as case D. Therefore it is more appropriate to model the forcing as an acceleration.

bandwidths of modes by simply adjusting a, thereby 'generating' data that 'fit' any predicted bandwidths. In fact, the choice of applying $a = 20 \sim 35$g is intrinsically an artificial manipulation. Because of such subjectivity, a perfect match between either theory and experiments is never proclaimed. Instead, the match is considered as a reasonable agreement. The 20∼35-g range is chosen for being capable of exciting all 12 non-zonal modes without ejecting satellite droplets. With the presented comparisons, the reasonable agreement suggests that the bandwidths predicted by forcing case D of the VPF theory adequately approximates the observed resonance of drops excited by $a = 20 \sim$35g.

3.3 Mode Crossing

3.3.1 Mode Crossing across 90° Contact Angle

As predicted by BS inviscid theory[10] and shown by combining figure 3.5(b)∼(d), 3.6 and 3.7, certain modes reverse orders on the frequency spectrum as contact angle changes. The experiments confirm the predictions and are summarized in figure 3.11. Recall that [5, 3], [5, 5], [7, 5], [7, 7], [9, 5], [9, 7] and [9, 9] are observed for drops on type B substrates. In figure 3.11, average frequencies of the observed maximum and minimum (cf. figure 3.5(b)∼(d), 3.6 and 3.7) are plotted against contact angles. The re-ordering of modes is obvious from figure 3.11: For the chosen target modes with $\alpha < 110°$, their orders of resonance frequencies are, from low to high, [5, 5]→[5, 3], [7, 7]→[7, 5] and [9, 9]→[9, 7]→[9, 5]. The orders reverse completely for $\alpha > 110°$, such that [5, 3]→[5, 5], [7, 5]→[7, 7] and [9, 5]→[9, 7]→[9, 9]. Careful inspection of figure 3.11 suggests that crossings are predicted

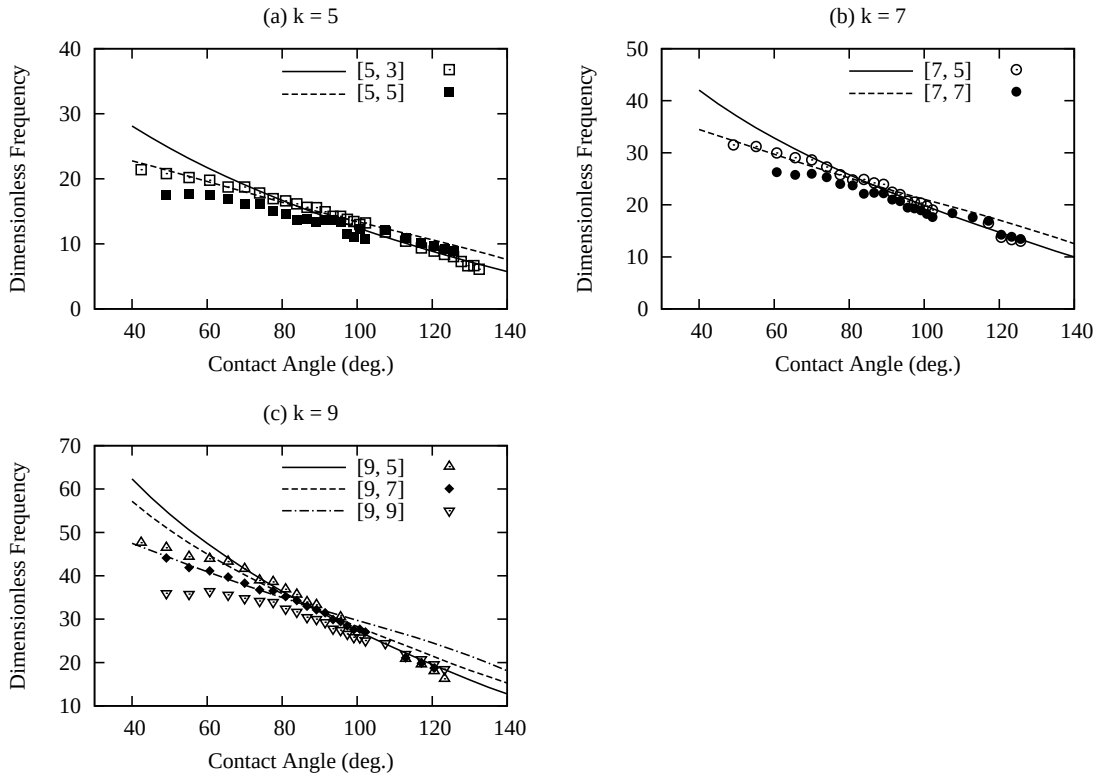

Figure 3.11: Mode crossing across $\alpha \approx 90°$. Symbols are average $(f_m + f_M)/2$ from figures 3.5, 3.6 and 3.7. Curves are predictions from BS inviscid theory for drops of pinned contact lines. For subhemispherical drops, [5, 3], [7, 5] and [9, 5] pertain to higher frequencies than [5, 5], [7, 7], [9, 7] and [9, 9], respectively. The order reverses for superhemispherical drops.

around $\alpha = 90°$ but not observed until $\alpha \approx 105°$. As mentioned in §3.2, modes mix and compete around $\alpha \approx 90° \sim 100°$. Since sectoral modes typically dominate, the mode crossing may occur as predicted but be masked due to the scavenging of tesseral modes by the sectoral.

3.3.2 Mode Crossing of Subhemispherical Drops

Besides the crossings around $\alpha = 90°$, similar phenomena occur for lower contact angles. For drops with $\alpha = 60° \sim 80°$, the crossings predicted by BS inviscid

theory for particular modes of $k = 7$, 8 and 9 are explored. Although BS inviscid theory also predicted crossings of modes with $k = 5$, 6 and 7, these predicted phenomena have not been observed in experiments.

Mode crossings of subhemispherical drops are probed by automatic frequency scans. All experiments utilize type A substrates. The experimental protocol is depicted in figure 3.12. A sufficient driving amplitude A_d, a starting (f_s) and an ending (f_e) frequencies are chosen first. Experiments start with oscillating a deposited drop of a prescribed volume at f_s. The amplitude is manually increased to A_d (a $\rightarrow$ b in figure 3.12), and then the scan is triggered manually and proceeds at 1Hz per second (b $\rightarrow$ g in figure 3.12). The top view of the oscillating drop is monitored by visually inspecting the real-time video stream from the high-speed camera. The forcing frequency is monitored with an oscilloscope. Upon observing any pattern variation (at point c, d and e in figure 3.12), the shape changes and the corresponding frequency measured by the oscilloscope are documented. The automatic frequency scan continues until the prescribed ending frequency f_e is reached (at point g in figure 3.12). The forcing acceleration along the locus b-c-d-e-g are 20g to 30g. Due to hysteresis, an excited mode tends to persist. In fact, mode selection is observed to depend mostly upon which mode is generated first, which in turn depends on the direction (i.e. up- or downward) of the frequency scan. Figure 3.12 conveys such mode-selection mechanism: The portion of Arnold tongues depicted as dashed curves represent the 'missing' boundary of a mode's bandwidth due to hysteresis. In the following discussion, all frequency scans are monotonic and results from upward ($f_s < f_e$) and downward ($f_s > f_e$) scans are reported separately. The protocol ensures that any depicted overlapping bandwidths indicate an observed mode mixing.

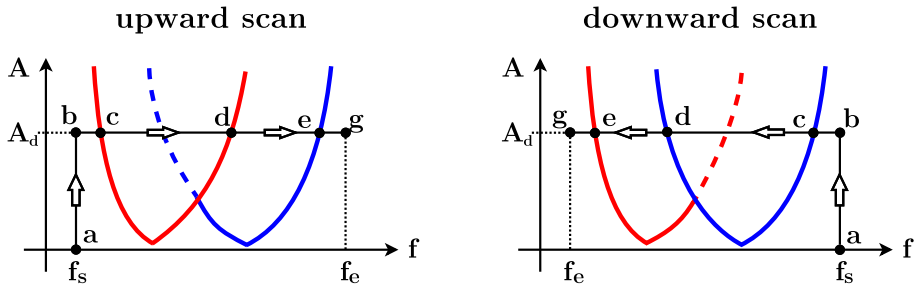

Figure 3.12: Protocol schematic for mode-crossing of subhemispherical drops. Parameters f and A are the forcing frequency and amplitude, respectively. The curves of the same color form Arnold tongues, which represent the bandwidth along as it depends on forcing amplitudes. At a fixed amplitude A_d, the automatic scan proceeds from a starting (f_s) to an ending (f_e) points b to g. Frequencies and mode shapes at points c, d and e are recorded. The dashed curve segments represent the mode's hidden bandwidth limit due to hysteretic competition of modes.

Based on previous experiments, crossings of $[8,8]$ and $[7,3]$, figure 3.13, and $[9,9]$, $[8,2]$ and $[8,4]$, figure 3.14, are investigated. These two sets are chosen because they are not only predicted but also repeatedly observed. To probe the phenomena, a range of contact angles is chosen such that frequency ranges of the crossing modes are separated from those of others. Upward and downward scan results are shown in figure 3.13(a), (b), respectively, where the shaded bands indicate range of observed frequencies. The same acceleration a is used for all these scans. Note that, in contrast to the inviscid prediction which is included as a simple guide to the eye, the VPF results would predict a crossing within the range of contact angle probed. In the upward scan, $[8,8]$ is observed to cross $[7,3]$ around $\alpha \approx 65°$. In the downward scan, the $[7,3]$ mode is missing for $\alpha \approx 65°$ and the crossing must be inferred from the scans near $\alpha \sim 60°$ and $\alpha > 70°$, where the $[7,3]$ reappears. In summary, mode mixing is observed where bands lie on top of one another and mode competition is observed where a mode disappears behind the band of another. Comparing figures 3.13(a) and (b) yields the extent of hysteresis. We say that sectoral mode $[8,8]$ hysteretically scavenges mode $[7,3]$,

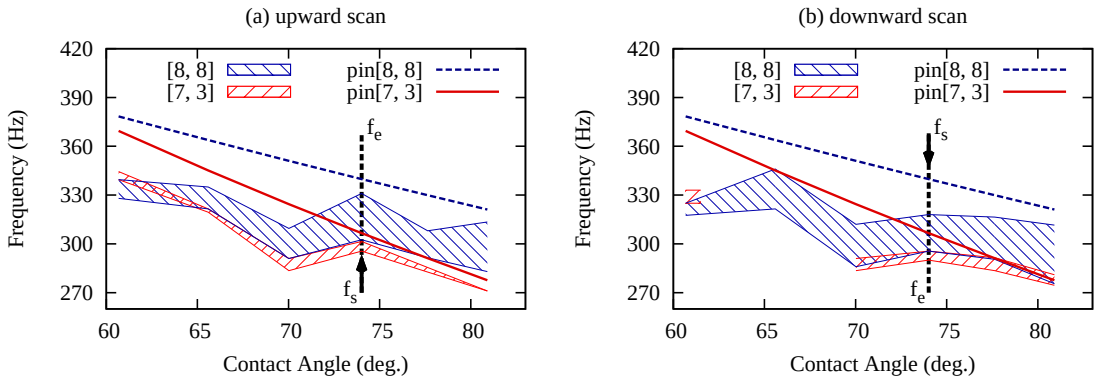

Figure 3.13: Bandwidths (hatched) of modes $[8,8]$ and $[7,3]$ for upward (a) and downward (b) scans, from f_s to f_e. Differences from (a) to (b) represent hysteresis. Based on (a), frequencies cross around $\alpha \approx 60^\circ \sim 70^\circ$. Based on (b), where there is a gap in the observation of the $[7,3]$ mode, the $[8,8]$ mode hysteretically scavenges the $[7,3]$ mode across the gap, from $\alpha \approx 62^\circ$ to about $\alpha \approx 70^\circ$. Lines are inviscid predictions, for reference.

figure 3.13(b), that there is a range of mode mixing, figure 3.13(a), and that the crossing occurs within $60^\circ \leq \alpha \leq 70^\circ$, figure 3.13(a),(b).

Results of $[9,9]$ crossing $[8,2]$ and $[8,4]$ are shown in figure 3.14. Similar features are observed. From figure 3.14(a) starting at $\alpha \approx 60^\circ$, $[9,9]$ is excited at the lowest frequency. As the contact angle increases, $[9,9]$ is observed to hysteretically annex the bandwidth of $[8,2]$ first around $\alpha = 65^\circ$ and then that of $[8,4]$ for $\alpha = 70^\circ$. According to upward scans, the crossing between $[9,9]$ and $[8,4]$ occurs roughly within $60^\circ \leq \alpha \leq 70^\circ$. Similarly, $[8,2]$ crosses $[9,9]$ within $65^\circ \leq \alpha \leq 75^\circ$. Further increase of contact angle finally allows the $[9,9]$ mode to separate from the other two modes completely. The $[8,2]$ and $[8,4]$ are observed to mix for cases with $\alpha > 75^\circ$. The driving amplitude a is the same for all the results reported in figure 3.14.

Whereas the upward scan shows mode mixing (overlapping bands), the downward scan reveals mode competition (disappearing bands). For the downward scan,

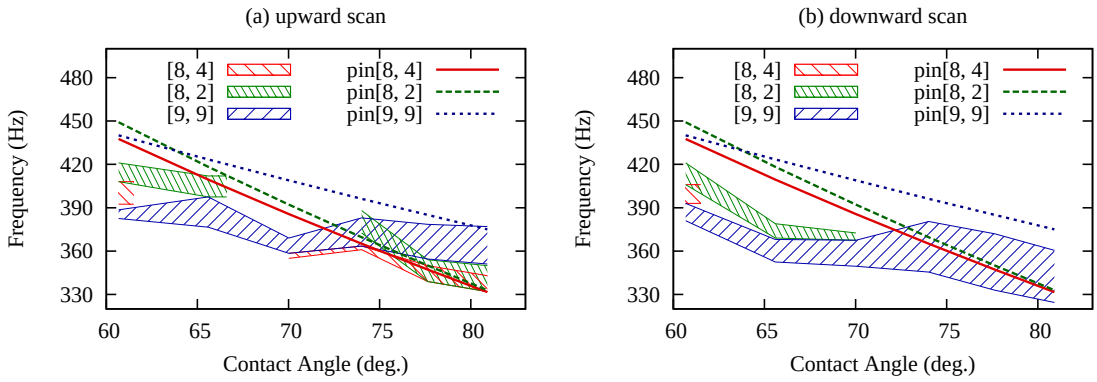

Figure 3.14: Bandwidths (hatched) of modes of modes $[9,9]$, $[8,2]$ and $[8,4]$ by upward (a) and downward (b) scans. Differences from (a) to (b) represent hysteresis. Based on (a), frequencies of $[9,9]$ and $[8,4]$ cross around $\alpha \approx 60^\circ \sim 70^\circ$ and of $[9,9]$ and $[8,2]$ around $\alpha \approx 65^\circ \sim 75^\circ$. Based on (b), the gaps in observed $[8,4]$ for $\alpha > 60^\circ$ of $[8,2]$ for $\alpha > 70^\circ$ suggests a hysteretic scavenging of both missing modes by the $[9,9]$ mode. Lines are inviscid predictions, for reference.

figure 3.14(b), all bands but the $[9,9]$ disappear for $\alpha > 70^\circ$. We say that the $[9,9]$ has scavenged the $[8,2]$ and $[8,4]$ modes. Another side of this hysteresis is seen in a separate test with a different protocol that varies driving amplitude. For $\alpha > 70^\circ$, starting with the observed $[9,9]$, the $[9,9]$ mode disappears if the amplitude is reduced sufficiently and then either $[8,2]$, $[8,4]$ or their mixture replaces $[9,9]$ when the amplitude is ramped back up to its original level. In summary, for $\alpha > 70^\circ$, a bi-stable bandwidth where drops of the same volume subject to the same forcing select a mode shape according to which mode emerges first is observed. The observation is in contrast to the work by Ciliberto and Gollub[22], which reports higher frequency modes as dominant mode when Faraday waves compete.

CHAPTER 4

SESSILE DROP III: AMPLITUDE RESPONSE

4.1 Overview

In terms of [2, 0] mode reported in [17], the amplitude responses of sub-, super- and harmonic resonances of a mechanically oscillated sessile drop are probed. Any mode of a drop is classified as harmonic, subharmonic or superharmonic according to how its resonance frequency f_r compare to forcing frequency f. For harmonic modes, $f_r = f$. For subharmonic (superharmonic) modes, $f_r = nf$, where n is some positive rational number such that $n < 1$ ($n > 1$).

At fixed frequencies, a drop is vibrated with different accelerations and its response amplitude acquired in terms of its *central height*, the height at the center of its footprint. figure 4.1 illustrates top- and side-view images of the [2, 0] mode of a sessile drop with maximal and minimal central heights. The [2, 0] mode is chosen because of its axisymmetry, its largest deflection among all zonal modes and its diverse harmonic responses. Its axisymmetry allows measuring a drop's deformation from the side by simple imaging techniques. Its largest deflection yields the best spatial resolution of the motion among zonal modes. Its presence as a harmonic or subharmonic mode allows exploring the dynamics of both families of resonance. Note that any standing wave patterns are considered as signs of a drop's resonance. Two distinct types of harmonic modes are recognized. For subharmonic [2, 0] modes, experimental evidence is presented to classify them as members of the same family as all half-frequency, subharmonic non-zonal modes. Finally, a technique of exciting [2, 0] mode as a superharmonic mode is demonstrated. In fact, [2, 0] mode is the best candidate for testing superharmonic resonance of drops

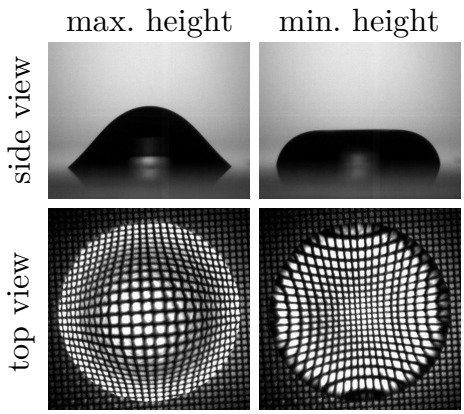

Figure 4.1: Top- and side-view images of a drop's [2, 0] mode with maximal and minimal central heights.

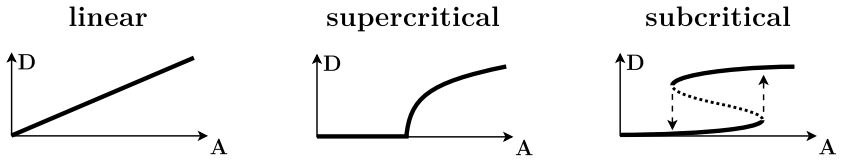

Figure 4.2: Three general scenarios of a drop's amplitude response D to the amplitude A of the forcing.

because of its relative 'loneliness' on the frequency spectrum.

From experiments, probed amplitude responses are classified as linear, subcritical or supercritical. As depicted in figure 4.2, linear modes are triggered at any infinitesimal forcing amplitude, while nonlinear modes, either supercritical or subcritical, require minimum amplitudes to excite. Subcritical modes differ from the supercritical by exhibiting hysteresis. In practice, experiments start with an upward-downward amplitude scanning procedure to detect any hysteresis. The up- and downward scans respectively probe the lower and upper branches of response curves (cf. subcritical case in figure 4.2). The former simply ramps up the forcing acceleration slowly to prescribed values. In the latter, the acceleration is first ramped up to exceed the upper limit of the lower branch and then slowly decreased to prescribed values.

For harmonic and subharmonic [2, 0] modes, nonlinear oscillator models are proposed to describe the observations. The earliest model for oscillations of inviscid spherical drops dates back to Rayleigh[90] and was later extended to include and non-zonal modes[62] by Lamb. Many studies[36][67] predict forced oscillations of drops but only discuss axisymmetric harmonic modes. A recent study[10] predicts zonal and non-zonal mode shapes for free oscillation of inviscid sessile drops. To the author's knowledge, no hydrodynamic theory is proposed for forced resonance of sessile drops in general. As the current study focuses on the amplitude response of forced harmonic resonances, the model must relate forcing to response. For simplicity, nonlinear oscillator models are developed using perturbation and two-variable expansion[89][85][98]. The general form of the models is

$$x''(t) + x(t) + \epsilon c x'(t) + \epsilon g(x, x', t) = A\cos(\omega t) \tag{4.1}$$

where $\epsilon \ll 1$, g is a nonlinear function, A the forcing amplitude, and $x(t)$ the response of the drop. While harmonic modes are triggered with small (< 1g) amplitudes in experiments and hence $A \sim \mathcal{O}(\epsilon)$, subharmonics requires large amplitudes (> 1g), i.e. $A \sim \mathcal{O}(1)$. A different nonlinear function g is specified for each type of harmonics. Superharmonic modes are not modelled due to the persisting noise associated with them.

Note that prior to modelling drops with nonlinear springs in Eq. 4.1, numerical computation is attempted using Ansys Fluent R14.5. For modeling drops, the volume-of-fluid method is adopted[48, 41]. The software performs computation in Navier-Stoke's equations. Initial and boundary conditions can be specified using user-defined functions (UDF)[2]. Due to the lack of numerical model for contact-line motion in the software, the computation does not converge. Further pursuit of numerical modeling was hence abandoned.

Table 4.1: Experimental parameters I: test-specific parameters

Harmonic Type	harmonic	subharmonic	superharmonic
Forcing Frequency	73Hz	147Hz	37Hz
Forcing Amplitude	0.1∼0.7g	0.6∼5.2g	0.2∼3.3g
Frame Rate	1500Hz	3000Hz	750Hz
Data Length	446	449	446

Table 4.2: Experimental parameters II: constant parameters

Drop	Substrate	Coating	Pinning Site	Resolution
16μL	glass	fluoro silane	circular, Φ = 5mm	12.6∼12.8μm/pix

4.2 Experimental Methods

All tests start with drop oscillation and image acquisition, followed by image analysis and frequency analysis, and finally the amplitude estimation of signals at target frequencies. The same vibration platform is used, as depicted in figure 4.3(a). A glass slide with a circular pinning site (type A substrates[16]) is installed on the platform. A DI water drop is deposited on the pinning site and vibrated. Side-view profiles of a drop are acquired by high-speed imaging. Experimental parameters are listed in table 4.1 and 4.2. The forcing frequencies are chosen based on other experiments (cf. chapters 2 and 3), which suggest 73 $\sim$ 74Hz as the resonance frequency of the [2, 0] mode of a 16-μL drop. The forcing accelerations are iteratively selected during experiments to clearly characterize dynamics of interest. The accelerations are measured using an accelerometer (model No. 8704B100, by Kistler Instrument Corp., Amherst, NY), whose signal is amplified by a signal conditioner (model No. 5114, by Kistler Instrument Corp., Amherst, NY) and monitored with a digital oscilloscope (model GDS-1102-U, by GW Instek, Taiwan). To facilitate direct comparison with models, measured forcing amplitudes are scaled by the footprint radius of the drop.

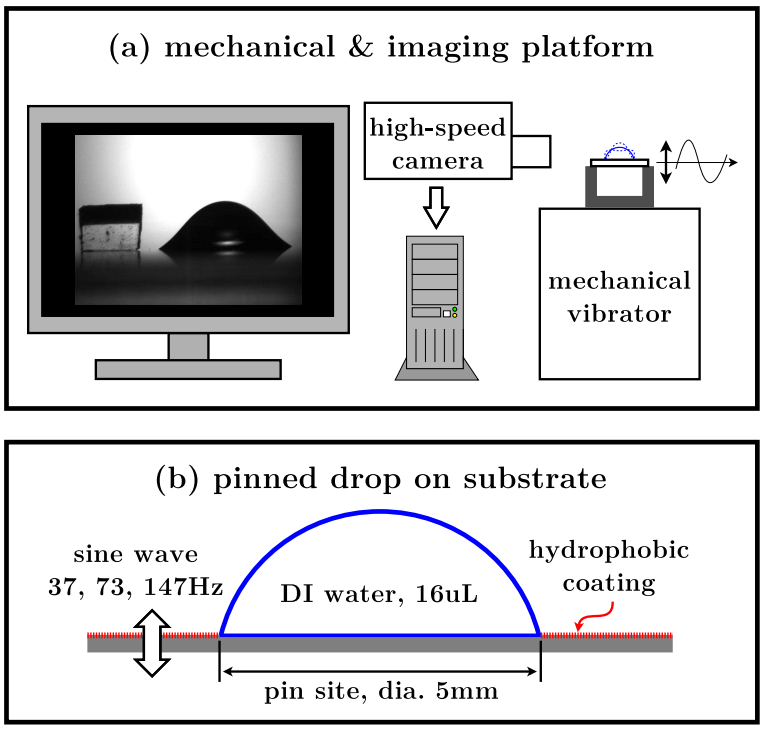

Figure 4.3: Experimental setup: (a) High-speed imaging a vibrated sessile drop's side view. (b) A drop on a substrate with a $\Phi = 5$mm pinning site.

The oscillation of a drop's central height is extracted from side-view images. An example is shown in figure 4.3(a) with a drop and a reference block to its left. The custom image analysis program traces the boundary of the drop. In addition, the program keeps track of the substrate's displacement in terms of that of the reference block. The method is reported in Appendix C. Position of the drop's contact line is updated. The distance between the midpoints on the drop's (1) contact line and (2) free surface is subsequently calculated as the drop's instantaneous central height. The same procedure is repeated for all images. The drop's response amplitudes at target frequencies are then acquired from the optimized frequency analysis (Appendix E) of the central height oscillation signal.

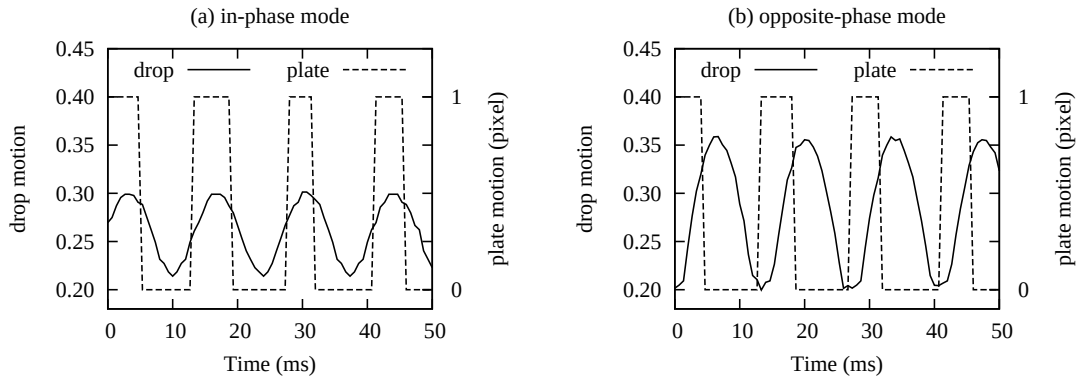

Figure 4.4: In- and opposite-phase modes of a drop driven at 73Hz and 0.4g. The in-phase mode in (a) is obtained from an upward scan, while the opposite phase in (b) comes from a downward scan. The presence of both in- and opposite-phase modes for the same forcing clearly suggests the bistability and hence nonlinearity of drop's oscillation.

4.3 Harmonic Resonance

Harmonic [2, 0] mode of vibrated sessile drops exhibits coupled hysteretic responses in phase and amplitude. At 73Hz, a small forcing acceleration triggers a drop's small-amplitude [2, 0] mode that oscillates nearly in-phase with the substrate. When the acceleration increases beyond threshold a_1, the drop's amplitude multiplies dramatically, and its phase becomes nearly opposite to the forcing. The drop's large-amplitude, opposite-phase mode persists until the acceleration decreases below threshold a_2. The observation of $a_2 < a_1$ suggests the bistability and hysteresis of a drop's harmonic [2, 0] mode. A direct experimental evidence is presented in figure 4.4: While both 16-μL drops are driven at 73Hz and 0.4g, one exhibit small-amplitude, in-phase mode and the other large-amplitude and opposite-phase. Responses of drops are presented in terms of the ratio of its central height to the footprint diameter. Substrate (plate) motions are pure sine waves, and their lack of smoothness in figure 4.4 results from their small amplitudes and the 1-pixel ($\approx 12.7\mu$m) resolution in image analysis.

In experiments of harmonic [2, 0] modes, up- and downward scans probe in- and opposite-phase modes, respectively. Downward scans first ramp up the acceleration to 0.5g before slowly decreasing to prescribed values. Results are shown in figure 4.5(a), where symbols in the lower and upper branches represent in- and opposite-phase modes, respectively. While the in-phase mode grows roughly linearly with forcing, the opposite-phase jump-starts and saturates quickly. These behaviors suggest that opposite-phase mode is nonlinear and subcritical. In contrast, the in-phase mode is either linear or supercritically nonlinear.

Besides amplitude jump and phase shift, a more subtle difference exists between shapes of in- and opposite-phase modes. Accumulated side-view profiles in the insets of figure 4.5(a) suggest that the former preserves a convex free surface at any time, yet the latter leads to concavity. In other words, bifurcating from in- to opposite-phase mode also results in the sign change of a drop's curvature.

The harmonic response $x(t)$ is modeled with $g(x, x', t) = \alpha x^3 + \beta x^5$ and $A = \epsilon F$, i.e.

$$x''(t) + x(t) + \epsilon c x'(t) + \epsilon(\alpha x^3 + \beta x^5) = \epsilon F \cos(\omega t) \tag{4.2}$$

For subsequent perturbation, Eq. (4.2) is expanded in terms of stretched time $\xi = \omega t$ and slow time $\eta = \epsilon t$ as

$$\omega^2 \frac{\partial^2 x}{\partial \xi^2} + 2\omega\epsilon \frac{\partial^2 x}{\partial \xi \partial \eta} + \epsilon^2 \frac{\partial^2 x}{\partial \eta^2} + x + \epsilon\omega c \frac{\partial x}{\partial \xi} + \epsilon^2 c \frac{\partial x}{\partial \eta} + \epsilon(\alpha x^3 + \beta x^5) = \epsilon F \cos(\omega t) \tag{4.3}$$

To model harmonic response, ω is perturbed off of the resonance frequency ($= 1$), i.e.

$$\omega = 1 + \epsilon k \tag{4.4}$$

Substituting $x = (x_0 + \epsilon x_1 + \epsilon^2 x_2 + \dots)$ and Eq. (4.4) into Eq. (4.3), the $\mathcal{O}(1)$

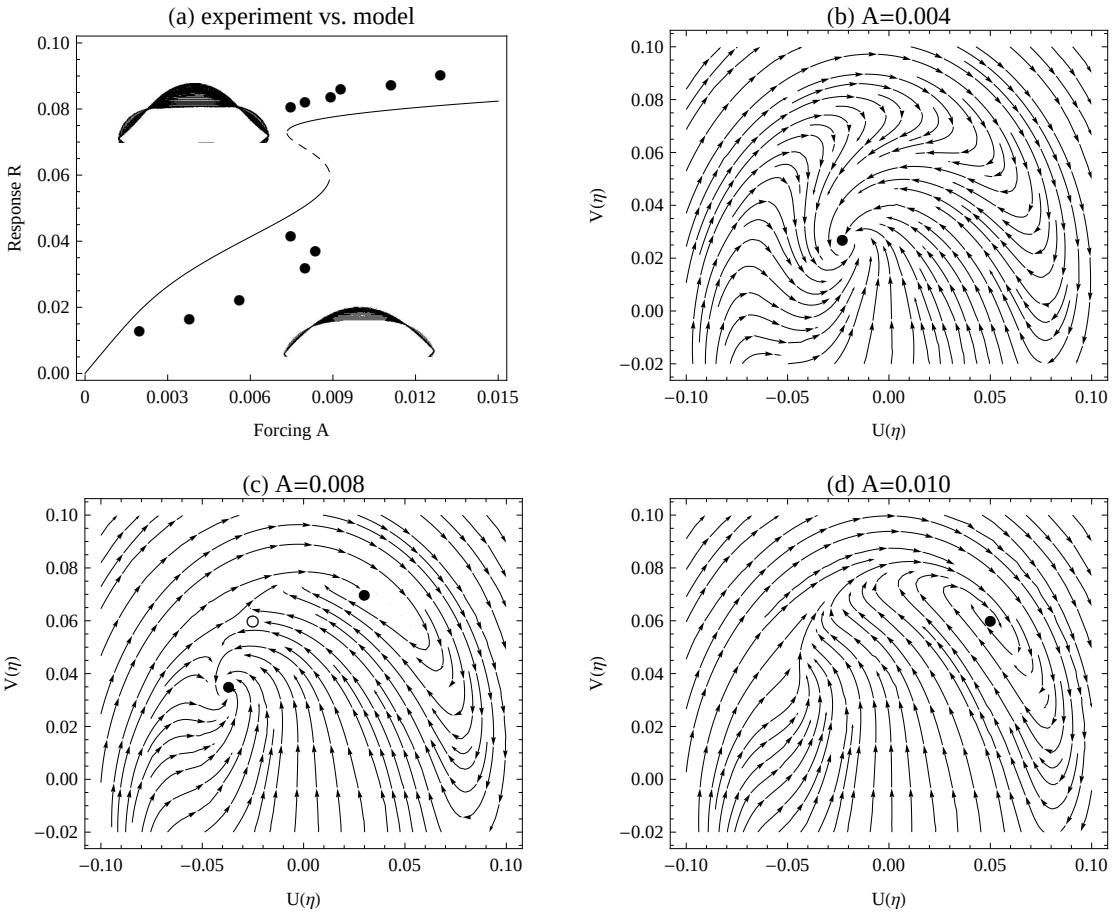

Figure 4.5: Amplitude response of a harmonic [2, 0] mode and the nonlinear harmonic oscillator model. Solid (dashed) line represents stable (unstable) branch. Filled (empty) circles are stable nodes (saddle). (a) Comparison of the experimental data and the model with $c = 0.1$, $\alpha = -120$ and $\beta = 26500$. (b-d) Phase portraits. (b) For small F, node Q_1 represent slow-time equilibrium of small-amplitude, in-phase mode. (c) Intermediate F induces bistability by creating a second stable node Q_2 and a saddle, but the drop's state remains equilibrated at Q_1. (d) Large F merges the saddle with Q_1, forcing the drop to exhibit large-amplitude opposite-phase mode.

equation is obtained as

$$\frac{\partial^2 x_0}{\partial \xi^2} + x_0 = 0, \qquad \Rightarrow x_0(\xi, \eta) = U(\eta)\cos(\xi) + V(\eta)\sin(\xi) \tag{4.5}$$

Substituting $x_0(\xi, \eta)$ into $\mathcal{O}(\epsilon)$ equation of Eq. (4.3), removing resonance terms $\{[...]\cos(\xi), [...]\sin(\xi)\}$ and rearranging the equations yield

$$F^2 = c^2 R^2 + \frac{9\alpha^2 R^6}{16} + \frac{15\alpha\beta R^8}{16} + \frac{25\beta^2 R^{10}}{64} \tag{4.6}$$

where $R^2 \equiv U^2 + V^2$ is the response amplitude. With $c = 0.1$, $\alpha = -120$ and $\beta = 26500$, the response curve is matched to the experiment data, as shown in figure 4.5(a). As nonlinear least-square fitting doesn't ensure uniqueness, no fitting is attempted and the response curve in figure 4.5(a) is manually tuned to match the probed bi-stable region.

Despite the obvious mismatch between model and data, the drop's behavior is qualitatively captured. For small F, the phase portrait in figure 4.5(b) exhibits a stable node Q_1 close to the origin. As F increases, a saddle S_1 and a new stable node Q_2 emerge, as shown in figure 4.5(c). The slow-time equilibrium at Q_1 persists until F further increases to merge Q_1 with S_1. The merger pushes slow-time equilibrium to Q_2, as shown in figure 4.5(d). When F decreases, S_1 re-appears and eventually merge Q_2, causing the slow-time equilibrium to move back to Q_1. The equilibria Q_1 and Q_2 pertain to opposite phases because they are on different sides of the vertical axis. In addition, that Q_2 lies farther from the origin than Q_1 explains the large- and small-amplitude modes. Hence for both phase shift and amplitude jump, the model captures the experimental observations.

4.4 Subharmonic Resonance

The same [2, 0] mode can be triggered as subharmonic resonance with an adequate acceleration within appropriate range of frequency. When a 16-μL drop is vibrated at 147Hz, a small acceleration triggers harmonic [4, 0] mode (figure 4.6(a)). Beyond certain threshold, a sufficiently large acceleration induces half-frequency subharmonic [2, 0] mode (figure 4.6(b)). Note that the [2, 0] modes in figure 4.6(a) and figure 4.4 oscillate with the same frequency, as they all complete roughly 4 periods within 50ms. They only differ in response amplitudes as a result of different forcing accelerations. By comparing the growths of harmonic (147Hz, [4, 0] mode) and subharmonic (74Hz, [2, 0] mode) signals with forcing acceleration, a clear distinction is found: In figure 4.6(c,d), harmonic signals are present at any acceleration, while subharmonic signals are either undetectable or present with a nearly saturated amplitude. In addition, detectable subharmonics dominate the spectrum. Careful inspection of figure 4.6(c, d) further suggests bistability between roughly 1.9g$\sim$3.5g forcing accelerations, as the drop can exhibit either harmonic- or subharmonic-dominant oscillations. The bistability manifests a subcritical bifurcation as the source of subharmonic [2, 0] mode.

The subharmonic amplitude response curve in figure 4.7(a) confirms the subcritical bifurcation. Two stable and two unstable branches exist, and former form a bistable region between $F = 0.009(1.78\text{g}) \sim 0.016(3.47\text{g})$. While the lower branch shows technically zero amplitude, the upper branch apparently saturates around $R = 0.1$. In experiments, the oscillated drop loses axisymmetry around $F = 0.0025(5.5\text{g})$, and a subharmonic, non-zonal mode replaces the subharmonic [2, 0] mode.

The subharmonic response $y(t)$ is modeled with $g(y, y', t) = \alpha y^3 + \beta y^2 +$

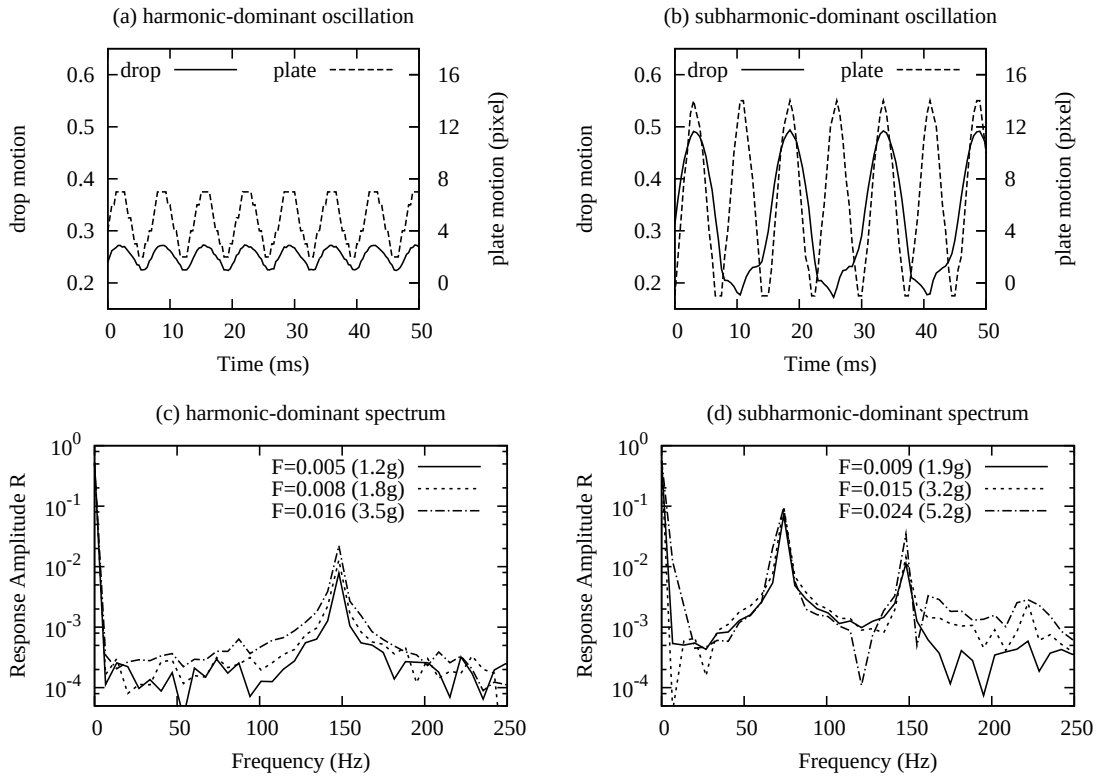

Figure 4.6: Response of drops in experiments for subharmonic [2, 0] mode. Solid (dashed) line represents stable (unstable) branch. Filled (empty) circles are stable nodes (saddle). (a) Small forcing acceleration triggers harmonic [4, 0] mode that oscillates with the same frequency as the forcing. (b) Sufficiently large acceleration induces half-frequency subharmonic [2, 0] mode. (c,d) Frequency spectra of harmonic- and subharmonic-dominant oscillations excited by 3.47g and 7.03g forcings, respectively. While the 74-Hz harmonic signal is always present, the 37-Hz subharmonics is either completely absent as in (c), or excited and dominate the frequency spectrum with a nearly saturated amplitude as in (d).

$\gamma y^2 \cos\omega t$ and $f = F$, i.e.

$$y''(t) + y(t) + \epsilon c y'(t) + \epsilon(\alpha y^3 + \beta y^2 + \gamma y^2 \cos\xi) = F\cos(\omega t) \tag{4.7}$$

Expanding Eq. (4.7) in stretched time ξ and slow time η yields

$$\omega^2\frac{\partial^2 y}{\partial\xi^2} + 2\omega\epsilon\frac{\partial^2 y}{\partial\xi\partial\eta} + \epsilon^2\frac{\partial^2 y}{\partial\eta^2} + y + \epsilon\omega c\frac{\partial y}{\partial\xi} + \epsilon^2 c\frac{\partial y}{\partial\eta} + \epsilon(\alpha y^3 + \beta y^2 + \gamma y^2\cos\xi) = \epsilon F\cos(\omega t) \tag{4.8}$$

To model 1/2-frequency subharmonics, ω is perturbed off of twice the resonance

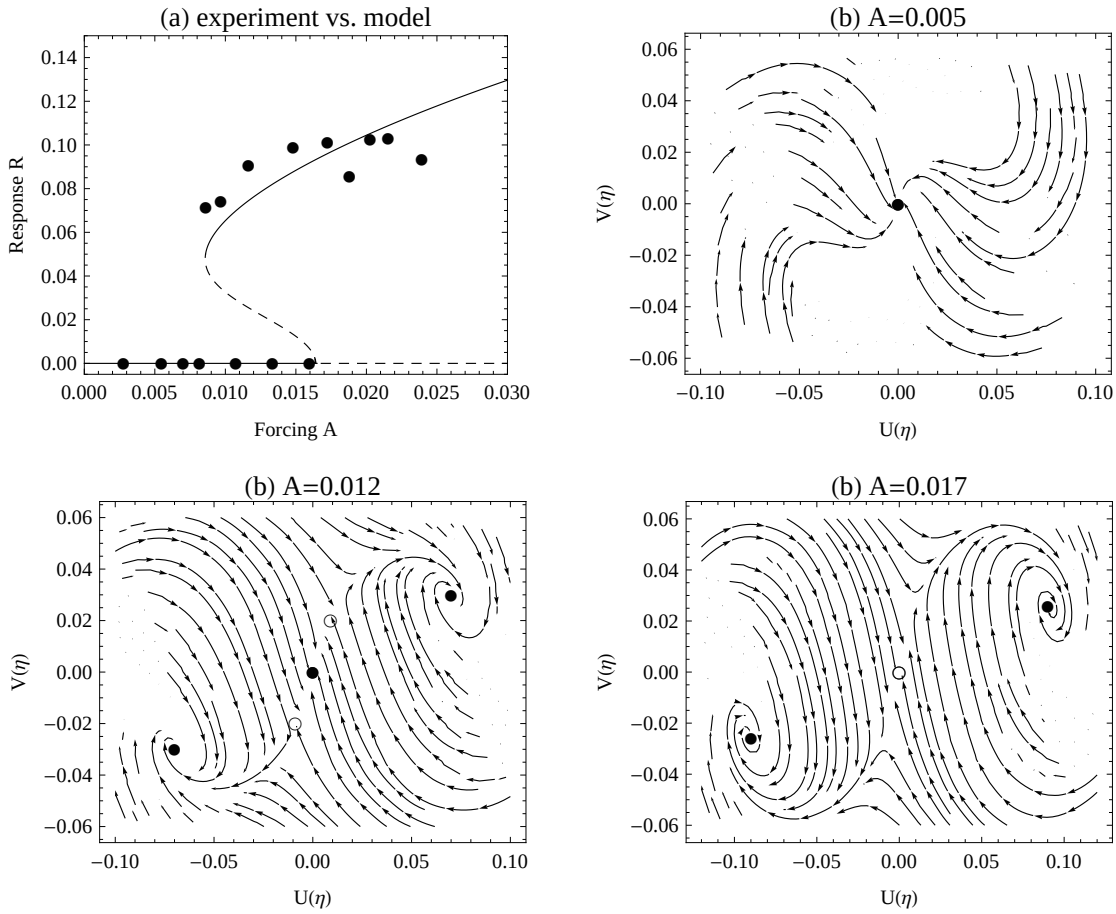

Figure 4.7: Amplitude response of subharmonic [2, 0] mode and the nonlinear subharmonic oscillator model. (a) Comparison of the experimental data and the model with $c = 0.004$, $\alpha = 2$, $\beta = 1.4$ and $\gamma = 1.21$. (b) When F is small, phase portrait of the model shows a stable node Q_3 at the origin. (c) When F increases, a pair of saddles and a pair of stable nodes $\{Q_4, Q_5\}$ with opposite phases emerge, but the state remains equilibrated at Q_3. (d) Further increasing F merges the saddles with Q_3 and drives the state of the system to either Q_4 or Q_5, resulting in the drop's subharmonic-dominant oscillation. The same slow-time equilibrium persists until F decreases so much that the saddles emerge again and merge Q_4 and Q_5.

frequency (= 2) of the system, i.e.

$$\omega = 2 + \epsilon k \tag{4.9}$$

Substituting $y = (y_0 + \epsilon y_1 + \epsilon^2 y_2 + \dots)$ and Eq. (4.9) into Eq. (4.8), the $\mathcal{O}(1)$ equation is obtained as

$$4\frac{\partial^2 y_0}{\partial \xi^2} + y_0 = F\cos\xi, \qquad \Rightarrow y_0(t) = U(\eta)\cos\frac{\xi}{2} + V(\eta)\sin\frac{\xi}{2} - \frac{F}{3}\cos\xi \tag{4.10}$$

Substituting $y_0(t)$ into $\mathcal{O}(\epsilon)$ equation of Eq. (4.8), removing resonance terms $[...]\cos(\xi)$ and $[...]\sin(\xi)$, rearranging the equations yields and neglecting de/tuning (set $k = 0$) yields the force-amplitude response

$$c^2 + \frac{\alpha^2 F^4}{36} + \frac{\alpha^2 F^2 R^2}{4} + \frac{9\alpha^2 R^4}{16} - \frac{\beta^2 F^2}{9} - \frac{F^3 \alpha\gamma}{9} - \frac{F R^2 \alpha\gamma}{2} + \frac{\gamma^2 F^2}{9} = 0 \tag{4.11}$$

With $c = 0.004$, $\alpha = 2$, $\beta = 1.4$ and $\gamma = 1.21$, the response curve is matched to the experiment data, as shown in figure 4.7(a). Again, the model in figure 4.7(a) is manually tuned, without fitting, to match the probed bi-stable region. The chosen set of parameters $(c, \alpha, \beta, \gamma)$ adequately captures the trend of the experiment data.

The model's phase portrait rationalizes the observation in experiments. In figure 4.7(b), small F results in one stable node Q_3 at the origin, suggesting no subharmonic oscillation. As F increases, a pair of saddles $\{S_2, S_3\}$ and a new pair of stable nodes $\{Q_4, Q_5\}$ emerge, as shown in figure 4.7(c). Node Q_3 remains the global equilibrium until F further increases and $\{S_2, S_3\}$ merge Q_3. The merger explains the amplitude jump of the subharmonic oscillation in experiments as now the state must jump to Q_4 or Q_5 to equilibrate. On the phase plane in figure 4.7(d), the behavior is characterized by the destabilized node at the origin and the newly emerged stable nodes. The two stable nodes are oscillations with 180° phase difference and hence equivalent. Decreasing F changes the phase portrait from figure 4.7(d) to 4.7(c): origin re-gains stability and saddles S_2, S_3 emerge.

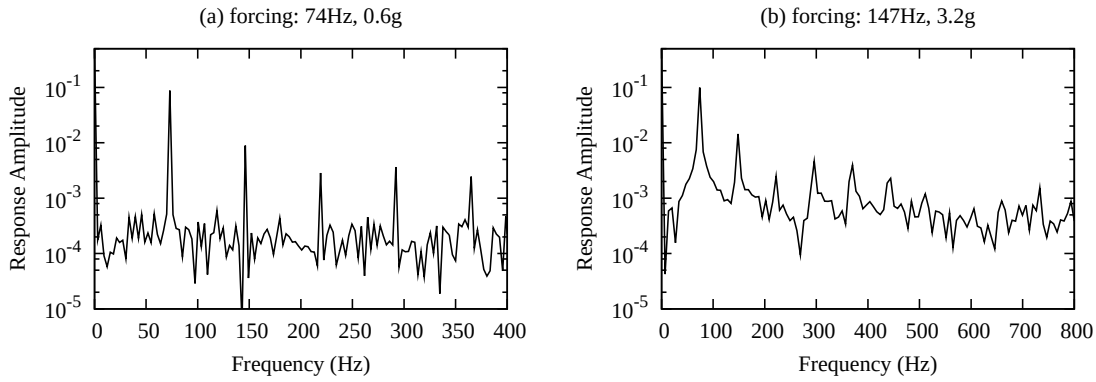

Figure 4.8: Typical frequency spectra from experiments of (a) harmonic and (b) subharmonic resonance showing multiple superharmonic peaks.

However, the subharmonic oscillation persists until F decreases so much that S_2, S_3 respectively merge Q_4, Q_5 and the origin recovers its unique global stability.

4.5 Superharmonic Resonance

The experiments with harmonic and subharmonic resonances motivate the pursuit of a drop's superharmonic modes. Frequency spectra from these experiments (figure 4.8) typically exhibit multiple superharmonic peaks. In addition, any forcing always excites a superharmonics at twice the forcing frequency. Thus the experiment here seeks to trigger the same [2, 0] mode by forcing the drop at 37Hz (= 74Hz $\div$2), thereby matching the double-frequency peak with the resonance frequency of the [2, 0] mode. Note that here a superharmonic [2, 0] mode equally clearly observable as the harmonic and subharmonic [2, 0] modes is sought. Unlike the weak superharmonic peaks in figure 4.8, a clearly observable superharmonic [2, 0] mode must not only be triggered but also dominate the frequency spectrum.

With sufficient forcing acceleration, the proposed frequency-matching technique effectively triggers superharmonic-dominant resonance. The fact that the drop's

central height in figure 4.9(a) maximizes twice in one forcing period manifests the dominant presence of double-frequency superharmonic resonance. The acceleration determines the significance of superharmonics: In figure 4.9(b), harmonic (37Hz) and superharmonic (74Hz) signals respectively dominate for $a < 1.5$g and $a > 1.7$g. While the harmonic signal may achieve 10 times the amplitude of superharmonics for $a < 1.5$, the former remains at least 1/3 the strength of the latter for $a > 1.7$. An example of each is presented in figure 4.9(c). Therefore the superharmonic oscillation only weakly dominates for $a > 1.7$g, since at least one other harmonic oscillation remain clearly distinguishable. Such weak dominance explains the unequal local maxima in figure 4.9(a) as the result of interference by harmonic waves. In addition, [1, 1] mode is triggered whenever superharmonic [2, 0] mode dominates. As harmonic and non-axisymmetric signals together significantly degrade the precision of the probed superharmonic signal, the observation is presented only to demonstrate the frequency-matching technique for triggering a drop's superharmonic-dominant oscillation without modelling.

4.6 Discussion & Conclusion

Different harmonic resonances of sessile drops are now compared in terms of their responses to forcing and their interactions with each other. For observed sub-, super- and harmonic [2, 0] modes at 74Hz, the orders of their amplifications and their extents of spectral dominance are the same, as presented in table 4.3. Consistent with these orders is that of forcing thresholds for triggering these modes. The threshold is discussed in terms of excitation Bond number Bo_a,

$$Bo_a = \frac{\rho r^2 a}{\sigma} \tag{4.12}$$

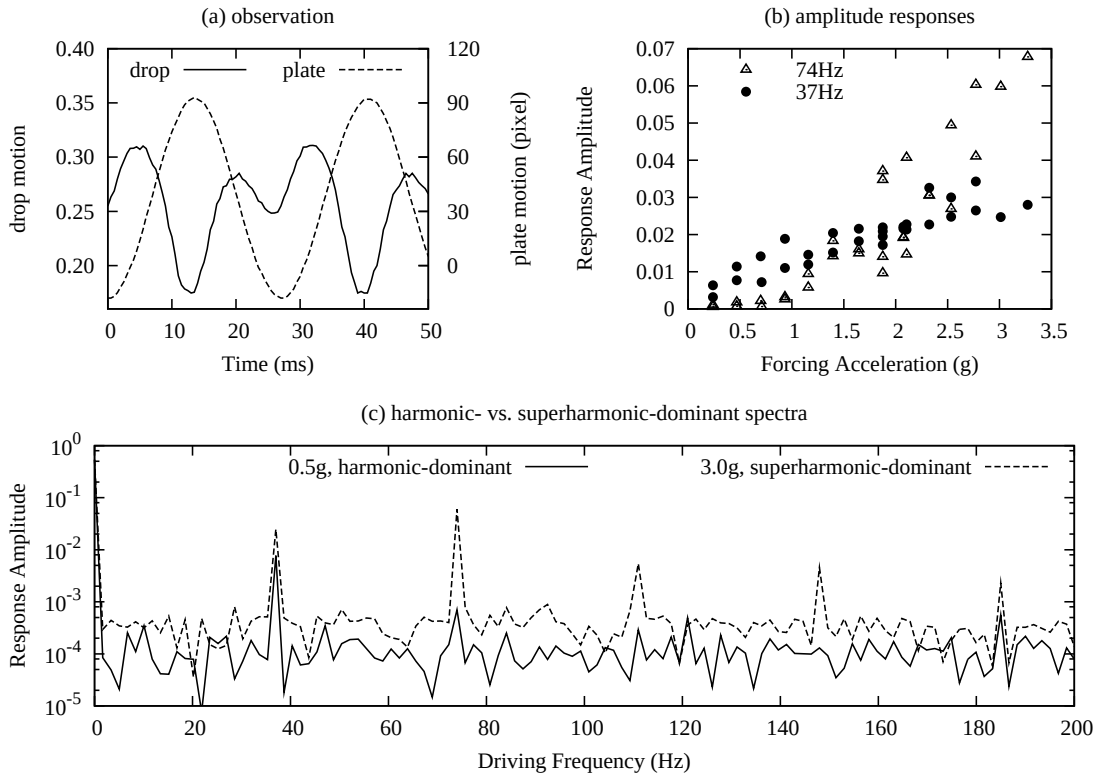

Figure 4.9: Results of probing superharmonic [2, 0] mode. (a) The drop's central height maximizes twice in one forcing period, and hence the dominating [2, 0] mode is double-frequency superharmonic. (b) Probed amplitude response of harmonic (37Hz) and superharmonic (74Hz) oscillations. (c) Frequency spectra at 0.5g and 3g forcing. The harmonic (37Hz) signal may be ten times as large as that of the superharmonics, yet the two dominates remains on the same order when the latter dominates.

where $\rho = 1000kg/m^3$ and $\sigma = 72mN/m$ are density and surface tension of water, $r = 0.0025$m the footprint radius of drops, and a the forcing acceleration measured by accelerometer (cf. Appendix B). The amplification is quantified by ratio J defined as

$$J = \frac{A \times f_r^2}{a}$$

where f_r (= 74Hz) and A are the resonance frequency and response amplitude of [2, 0] mode in experiments. In addition, a parameter is needed to quantify how much stronger or weaker the 74-Hz signal compare to others. As a crude

measure, the extent of dominance p is defined as the ratio of its (74-Hz signal) amplitude to that of the second-largest signal on the frequency spectrum. According to results in table 4.3, harmonics requires the least forcing to trigger, most effectively amplifies the forcing, and most profoundly dominates the spectrum. Thus small accelerations trigger a drop's harmonic oscillations. The overwhelming dominance and significant amplification further make harmonics technically the only observable modes. Sufficiently high forcing acceleration may trigger subharmonic resonance if their frequencies are close to 2:1. The slightly weaker dominance of subharmonics explains the typical observations of their coexistence with harmonic modes(cf. [17][16]). For mixture of harmonic and subharmonic zonal modes, please refer to figure 5.6). In contrast to the strengths of harmonics and subharmonics, superharmonics requires substantial excitation to trigger but weakly dominates spectrum and slightly amplifies forcing. Because the required excitation always exceeds thresholds for some neighboring modes on the spectrum, observed superharmonic [2, 0] modes are always severely interfered. When resonance frequencies of all modes from the previous study[17] are marked on a single frequency axis, one notices that higher-frequency modes are more densely packed. Because [2, 0] mode possesses the lowest resonance frequency among zonal modes and the second-lowest among all modes[72], it is already the best candidate for triggering a least-interfered superharmonic oscillation. The only interference comes from the [1, 1] mode and some harmonic waves. **In fact, superharmonic [2, 0] mode is perhaps the only observable superharmonic resonance.** Any pursuit of other superharmonic zonal modes always induces harmonic and subharmonic modes that dominate the drop's shape oscillation, resulting in the typical absence of superharmonics. Recall that even the subharmonic modes must compete for presence[16], let alone the superharmonic modes!

Table 4.3: Amplification ratio and extent of dominance for different harmonic modes.

Type	harmonics	subharmonics	superharmonics
$\min(Bo_a)$	0.34	1.5	1.2
q	14∼20	2∼4	1.5∼2
p	9.4∼ 12	2.7∼8.3	1.1∼2.5

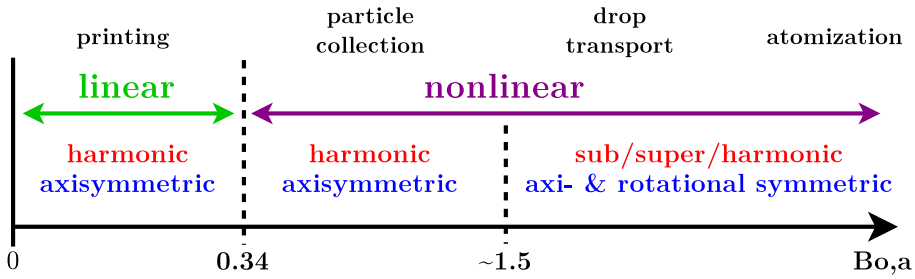

Figure 4.10: Droplet oscillation involved in different applications. While ink-jet printing requires mitigating droplet oscillation and hence a sufficiently small Bond number, atomization requires the largest possible Bond number to break up a large drop into satellite droplets.

In sum, amplitude-response measurements of a drop's harmonic, subharmonic and superharmonic [2, 0] modes are reported, and models for harmonic and subharmonic modes based on nonlinear oscillators are developed. The characterized responses of subharmonic zonal modes will be combined with their mixing with harmonic zonal modes in section 5.1. The integrated discussion will further assimilate subharmonic zonal and non-zonal modes to infer general amplitude response of half-frequency subharmonics.

Superharmonic-dominant oscillations are triggered with the frequency-matching technique. Based on key parameters (cf. table 4.3), the frequent occurrence of subharmonic and harmonic modes and the rarity of superharmonics are rationalized. Note that all modes reported in the previous study[17] are nonlinear and subcritical. Finally, different extents of droplet oscillations for various applications are recommended figure 4.10 for practical reference.

CHAPTER 5

SESSILE DROP IV: MODE MIXING

The content of this chapter has been largely disseminated in Chun-Ti Chang, Joshua B. Bostwick, Paul H. Steen, and Susan Daniel, *Phys. Rev. E, 88:023015, Aug 2013*.

5.1 Observations

In experiments, simultaneous coexistence of different modes is frequently observed. As shown in figure 5.1, all experiments technically start with forcing a drop at a prescribed frequency and and increasing amplitude (a $\rightarrow$ b or e $\rightarrow$ d). Then a frequency scan follows (b $\rightarrow$ c or d $\rightarrow$ c). If the bandwidths of a non-zonal mode and a zonal mode overlap, coexistence of the two modes occurs.

Mixed modes are typical, especially for modes with more complex shapes. The phenomena is illustrated with the image sequence of a relatively pure [5, 3] mode in figure 5.2. In figure 5.2, at $t = 1.75$ ms and 4.47 ms the drop apparently exhibits a Y pattern inside a triangle, which confirms the similarity of the observed pattern with the postulated [5, 3] mode in figure 2.2. Figure 5.3 shows a contrasting example with the mixture of [5, 3] and [8, 0] modes. At $t = 0$, 1.6, 2.0, and 3.8 ms, a rounded triangular wave pattern close to the contact line of the drop is first identified. The image for $t = 1.6$ and 3.8 ms exhibit Y patterns inside their outer triangular azimuthal wave patterns. Consider the common feature of possessing Y patterns inside an outer triangle for the two frames and those for $t = 1.75$ and 4.47 ms in figure 5.2. Apparently the image sequence in figure 5.3 contains [5, 3] as one of its wave components. By visually examining images for $t =$

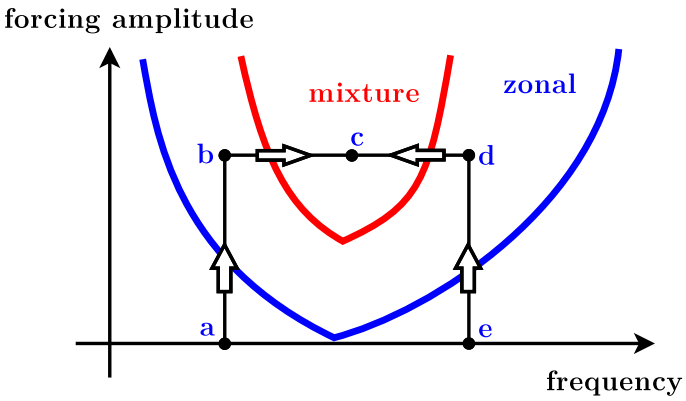

Figure 5.1: Protocol schematic for mode-mixing. Parameters f and A are forcing frequency and amplitude, respectively. The curves of the same color form two Arnold tongues, which represent the bandwidths of two modes at different forcing amplitudes. In practice, the forcing amplitude is first increased (a $\rightarrow$ b or e $\rightarrow$ d) and typically a zonal mode is triggered. Then a frequency scan at the fixed amplitude (b $\rightarrow$ c or d $\rightarrow$ c) may trigger a non-zonal mode. The mixture of the two modes is observed if their bandwidths overlap.

0.8 and 2.8 ms, one observes roughly identical axisymmetric distribution of mesh pattern deformation, which indeed suggests the coexistence a zonal mode with the tesseral, [5, 3] mode. With careful inspection of images for $t = 0.8$ and 2.8 ms, one finds that the zonal mode is [8, 0]. Indeed, such coexistence also explains why the images for $t = 0$ and 2.0 ms in figure 5.3 show a smaller rounded inner pattern instead of a sharper triangular or Y pattern. Furthermore, one finds within approximately 3.8 ms, the [5, 3] mode completes one single period of oscillation, while two roughly identical axisymmetric profiles ($t = 0.8$ ms and $t = 2.8$ ms) appear approximately every 2 ms. The driving frequency is 454 Hz. From the original image sequence of figure 5.3, the (lowest) estimated resonance frequency is 227.27 Hz (cf. Appendix D). Since [8, 0] repeats twice when [5, 3] completes one cycle, the [8, 0] frequency is 454.54 Hz. Therefore figure 5.3 shows that a single droplet, which is oscillated by a sinusoidal signal of one single frequency, simultaneously exhibits two distinct modal behaviors: one being a harmonically generated zonal mode, and the other a subharmonically generated tesseral mode.

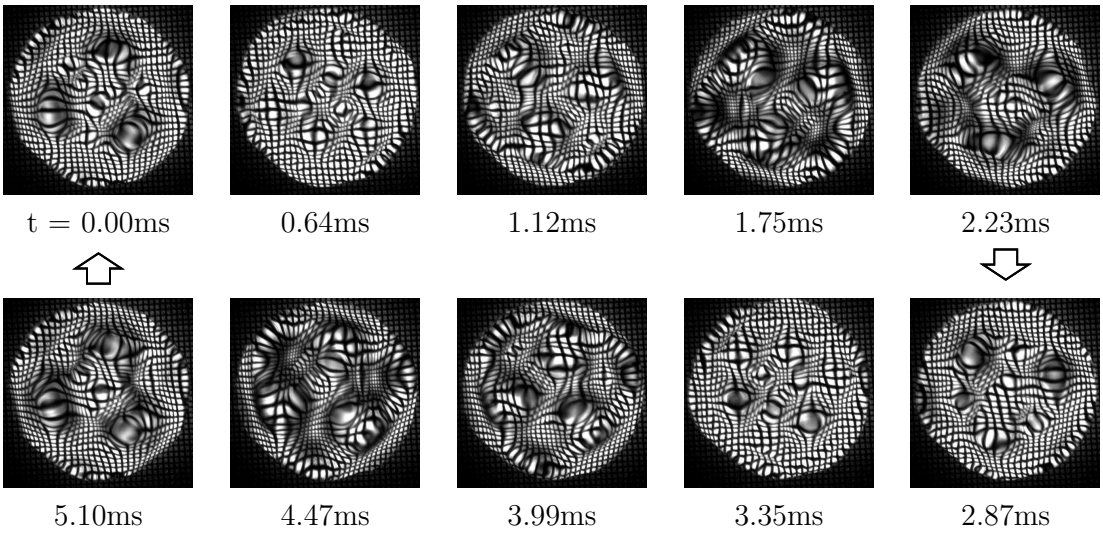

Figure 5.2: Image sequence of a relatively pure [5, 3] mode. The image of $t = 1.75$ ms corresponds to that with (n, l) = (2, 3) in figure 2.3.

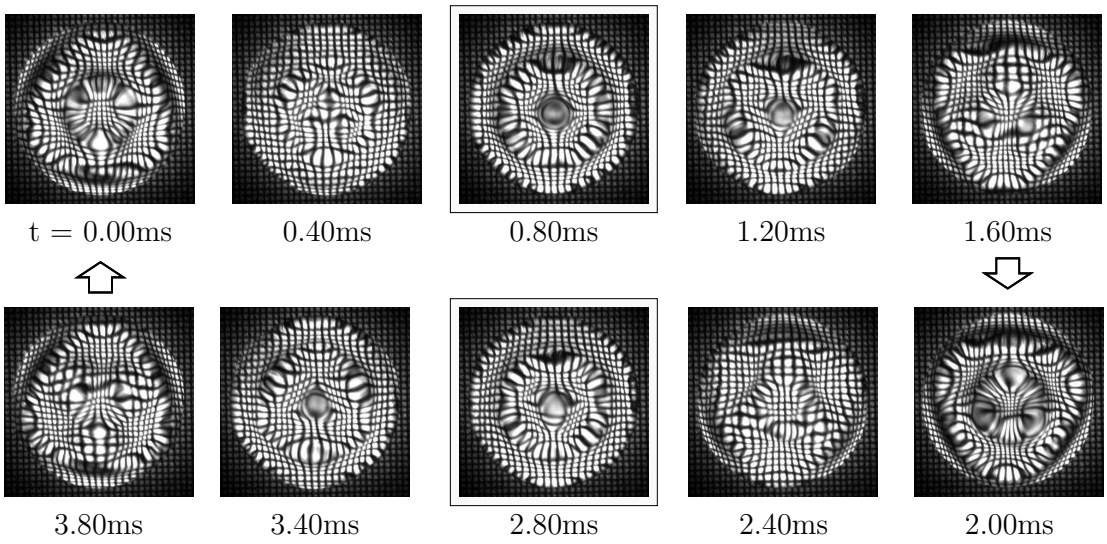

Figure 5.3: Image sequence of a [5, 3] mode mixing with a [8, 0] mode. The [8, 0] appears twice in one period of the [5, 3] and oscillates with the same frequency as the driving signal. The [8, 0] is boxed to highlight that mode. The shape is confirmed by comparing the boxed images to that of (n, l) = (5, 0) in figure 2.3.

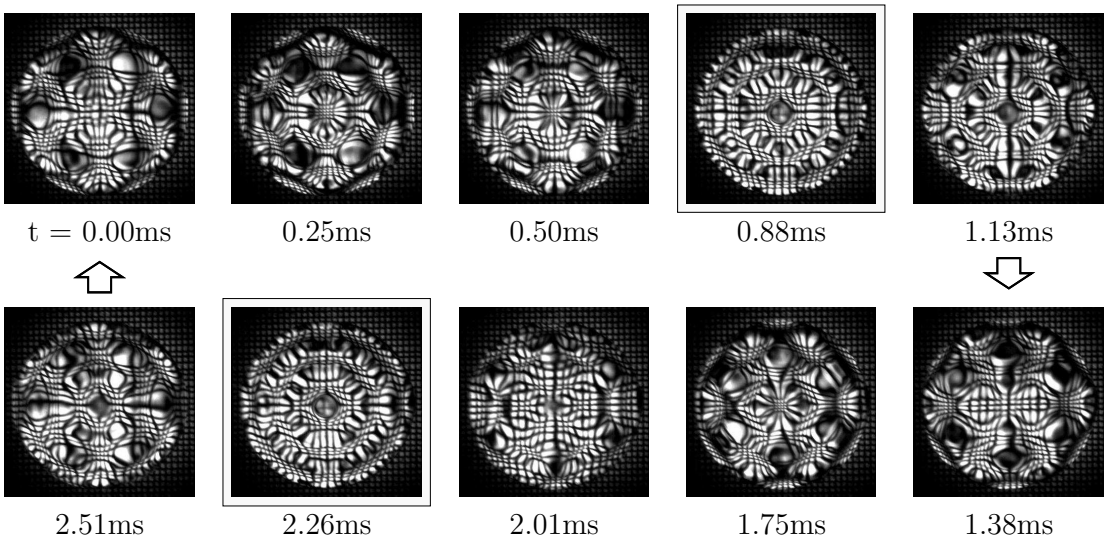

Figure 5.4: Image sequence of a [8, 6] mode mixing with a [12, 0]. The latter is boxed for the same reason as the [10, 0] in figure 5.3. The shape is confirmed by comparing the boxed images to that of (n, l) = (7, 0) in figure 2.3.

To further illustrate the ubiquity of mode mixing, one more example is presented in figure 5.4. For images of $t = 0.88$ and 2.26 ms, similar zonal patterns corresponding to the [12, 0] mode are identified. Since other images all exhibit a hexagonal star confined within a hexagon, a component of the [8, 6] mode is recognized. Therefore figure 5.4 is an example of a tesseral [8, 6] mixing with a zonal [12, 0] mode.

For pure and mixed mode shapes, a qualitative comparison of observations and BS inviscid theory is presented in figure 5.5. For the zonal mode in each mixing pair, superscript "-" or "+" respectively indicates concavity or convexity of the drop's center in the image. In mixture A, for example, the magnified mesh at the drop's center suggests local convexity of the [8, 0] mode, and hence $[8, 0]^+$. Because mixture A shows a concaving center, adding $[8, 0]^+$ to such mixture recovers the pure shape of [5, 3] mode. Similar method apply to all other cases.

Subharmonic zonal and non-zonal modes exhibit similar mixing with harmonic

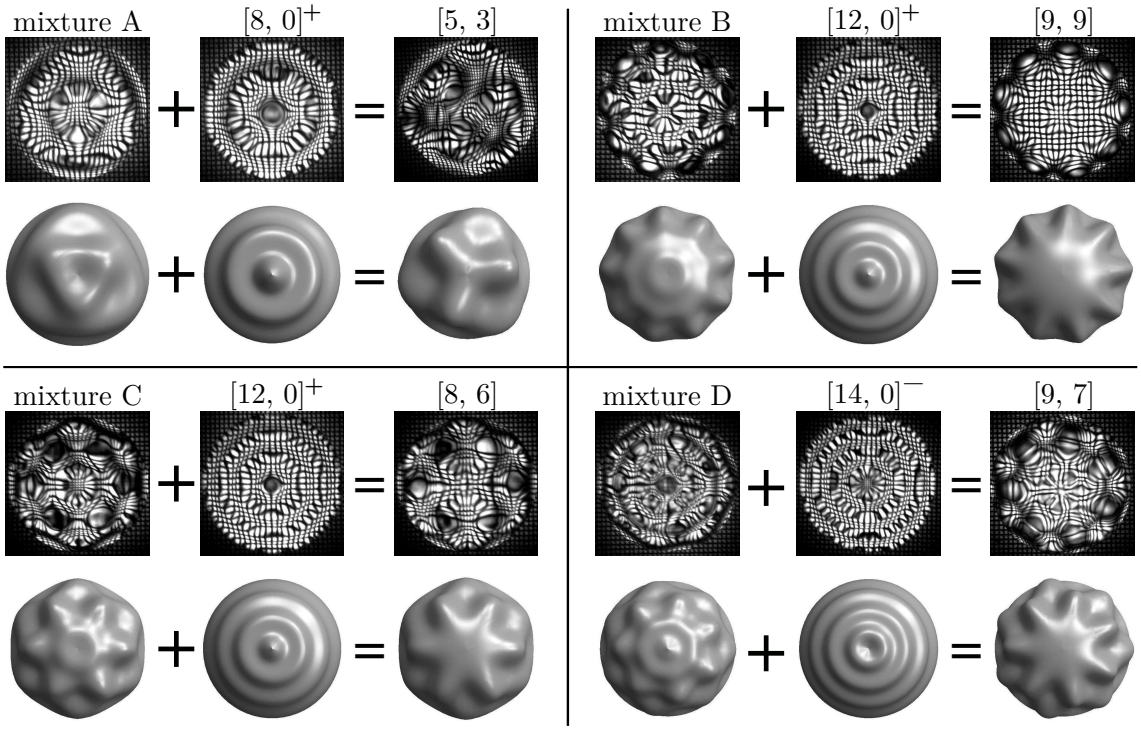

Figure 5.5: Examples of mixed and pure modes. Superscript "-" and "+" of zonal modes respectively indicate concavity and convexity of the drop's center in the image. Take the [8, 0] mode in mixture A as an example: The magnified mesh at the drop's center suggests local convexity, and hence $[8, 0]^+$. Because mixture A shows a concaving center, adding $[8, 0]^+$ to mixture A recovers the pure shape of [5, 3] mode.

zonal modes. Figure 5.6 presents examples of (a) subharmonic [2, 0] mixing harmonic [4, 0] and (b) subharmonic [6, 0] mixing harmonic [12, 0]. The mode shapes are identified with the scheme in the previous study[17]. An image of each mode with the least mixing is presented to demonstrate its presence. Notice that the white circular marks are nodal circles for [2, 0], [4, 0] and [6, 0] modes but troughs for [12, 0] mode. Superscript "-" or "+" respectively indicates concavity or convexity of the drop's center in the image. In figure 5.6(a), for instance, at $t = 14.4$ms the drop mainly exhibits a [2, 0] mode. The drop's center concaves since it locally shrinks the mesh, and hence $[2, 0]^-$. In figure 5.6(b), at $t = 24ms$ the drop exhibits [12, 0] mode whose center magnifies the mesh, and hence $[12, 0]^+$. The examples

illustrate a drop's oscillation within one period of subharmonic modes. As both mixing modes are axisymmetric, it is perhaps not clear from these images that the harmonic mode completes two periods within the same duration. The suspicion is cleared by repeating each test with the same forcing frequency but sufficiently low accelerations. Harmonic [4, 0] and [12, 0] modes are observed in the repeated tests of figure 5.6(a) and (b), respectively.

Although this section focuses on mode mixing, it is interesting to point out that figure 5.6 completes the association of subharmonic zonal modes with other subharmonic modes. In addition to illustrating mode mixing, figure 5.6(b) also confirms that [2, 0] mode is not the only subharmonic zonal mode, nor is it the only subharmonic zonal mode to mix with harmonic zonals as linear superposition. Furthermore, these mixing modes resemble the mixture of harmonic zonal and subharmonic non-zonal modes by linearly superposing their shapes without changing their respective harmonic or subharmonic natures. The existence of a complete family of half-frequency subharmonic [$2n$, 0] modes, where $n = \{1, 2, ...\}$, is therefore speculated. So far this study has shown that both subharmonic zonal and non-zonal modes exhibit hysteretic amplitude response, they mix with harmonic zonal modes in the same way, and together they complete the whole family of modes in figure 2.3. Therefore half-frequency subharmonic zonal modes are recognized as members of the same subharmonic family as the non-zonal modes. Furthermore, the dynamics of the subharmonic [2, 0] mode in §4.4 is speculated to represent the dynamics of all other half-frequency subharmonic modes.

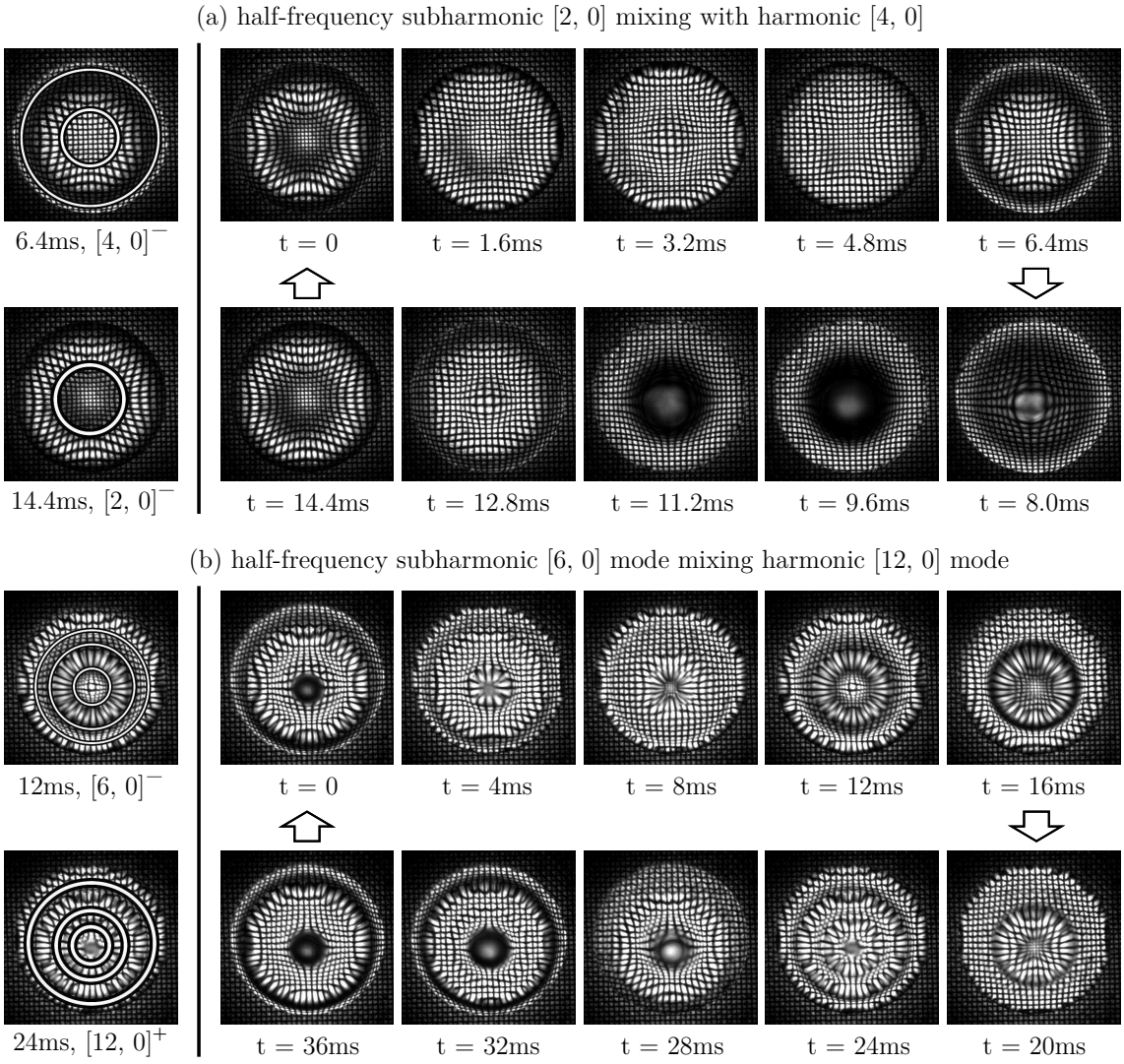

Figure 5.6: Examples of subharmonic zonal modes mixing with harmonic zonal modes. (a) Nodal circles of [2, 0] mode at $t = 6.4$ms and [4, 0] mode at 14.4ms are marked in white. The superscripts "-" for each mode indicate the drop's instantaneous concave center. (b) Nodal circles of [6, 0] mode at 12ms is marked in white. For clarity, troughs of the [12, 0] mode's are marked in white. The superscript "+" of [12, 0] indicate the drop's instantaneous convex center.

5.2 Mode Separation

A practical method of separating mixing modes is presented in this section. Among the first 35 modes with $k \leq 10$ and $l \leq 10$, all but $[k, l] = [10, 4]$ are reported in the first publication of this study[17]. The causes of the mode's absence was unclear at the time of the first publication, yet previously observed [10, 2] and [10, 6] modes presumably suggest the existence of [10, 4] mode. The absence of the [10, 4] is speculated to result from its bandwidth overlap with other modes [22]. In pursuit of this missing mode, a mode separation technique is noticed, and images of other pure modes acquired.

With pinning sites providing effective control over a drop's contact angle, generation of pure modes is readily facilitated. In experiments, resonance spectra of drops are found to depend sensitively upon contact angles and mode separation essentially takes advantage of such sensitivity. The practical mode separation technique is illustrated in figure 5.7, where the Arnold tongues of two modes are depicted. The tongues represent the bandwidth of the two modes at different forcing amplitudes. The technique here seeks to identify pure modes by separating the tongues, and operationally the technique simply utilizes drops of different contact angles. In practice, the finding of a target mode starts with a preliminary frequency scan to locate its resonance band. If the mode mixes with another, such as the situation in figure 5.7(a) where the bandwidth of the target mode overlaps with that of another (interfering) mode, a drop with a different contact angle is tested with the same procedure. Suppose the contact angle of the drop increases from the first to the second trial. In the worst case when both trials produce mixing modes (cf. figure 5.7(a)), a third trial is attempted with a drop of a lower contact angle. Bandwidths of the target and interfering modes should

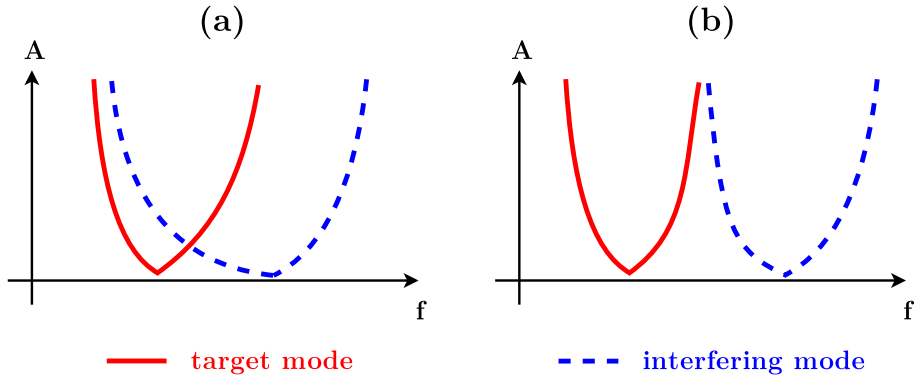

Figure 5.7: Schematic of mode separation technique. Parameters f and A are forcing frequency and amplitude, respectively. The curves of the same color form two Arnold tongues, which represent the bandwidths of two modes at different forcing amplitudes. By varying static contact angles of drops, the tongues can be separated, thereby facilitating acquisition of pure mode shapes.

be effectively separated in the third trial, as depicted in figure 5.7(b). Therefore for any mode already observed, a pure shape reasonably close to predictions by [10] are typically found within three trials. Depending on the target mode, the required forcing acceleration ranges from 10g to 100g. Top-view snapshots of the [10, 4] mode for an excited sessile drop is presented in figure 5.8, where the two images differ by half a cycle of oscillation. The mode is generated with a 16μL drop on a 5-mm (diameter) pinning site on glass. For scientific exploration, the method allows generating pure mode shapes for visualization purposes, while from the engineering perspective, the technique facilitates active patterns for specific applications.

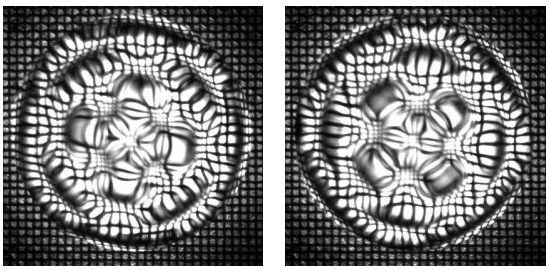

Figure 5.8: Top-view snapshots of the missing [10, 4] mode from previous experiments in [17]. The two images differ by half a cycle of oscillation. The drop is 16μL and confined within a 5-mm (diameter) pinning site on glass (substrate A).

5.3 Comparison with Bostwick-Steen Viscous Potential Flow Theory

To properly describe observed mode mixing phenomena, the observations are compared to Bostwick-Steen viscous potential flow (VPF) theory. In experiments seeking modes with $k \leq 10$ and $l \leq 10$, totally 188 mixing modes are observed. These experiments are conducted with type C substrates (cf. Appendix F) and contact angles are roughly $60^\circ \sim 80^\circ$. Recall that predictions from VPF theory based on forcing case D reasonably agrees with the experiments for $60^\circ \leq \alpha \leq 80^\circ$. A similar reasonable agreement is therefore expected for the mode mixing.

In experiments, different views of a drop are recorded for various purposes. Before and after applying mechanical oscillation, static side-view images of a deposited drop are recorded for measuring contact angles. Once the driving signal is applied, the shape of an oscillating drop is recorded from the top (top view I), left and then right. To check whether the observation from side views pertain to the same mode as the first top view, another top-view image sequence (top view II) is recorded. In most cases, two mixing modes can be clearly identified from the top. In cases when mode identification is difficult, side views are particularly useful for

identifying the zonal mode of a mixing pair. To relate to the VPF theory, contact angles measured from static side views before and after oscillation are related to top views I and II, respectively. Contact angles are manually measured using open source software `ImageJ`.

5.3.1 Assumptions & Definitions

The following comparison is based on several assumptions and definitions. If both top views I and II exhibit mode mixing, they are regarded as two different mixing pairs regardless of whether the modes are the same, since the contact angle is typically changed by the forcing. Pinned contact lines are assumed since drops typically exhibit little contact line motion on type C substrates. Instead of truncating response curves at the valleys, a 1-% bandwidth is adopted here since any observable mode must exhibit slightly stronger intensity then its neighbors. Finally, without being able to precisely quantify the effect of evaporation, a constant 20-μL volume is assumed.

Given a pair of mixing modes and the corresponding static contact angle, the VPF theory is tested by checking whether the predicted bandwidths overlap. A simple measure, denoted as degree of overlap H, is defined to quantify how much two bandwidths overlap. As illustrated in figure 5.9, let bandwidths of mode I and mode III span (f_1, f_2) and (f_3, f_4), respectively. The degree of overlap is defined in terms of the total span P and the overlap Q of the two bandwidths, such that $(i = 1, 2, 3, 4)$

$$P = \max(f_i) - \min(f_i), \quad Q = (f_4 - f_3) + (f_2 - f_1) - P, \quad \Rightarrow H = \frac{Q}{P} \tag{5.1}$$

According to Eq. 5.1, $Q > 0$ if the bandwidths overlap. The choice of normalizing

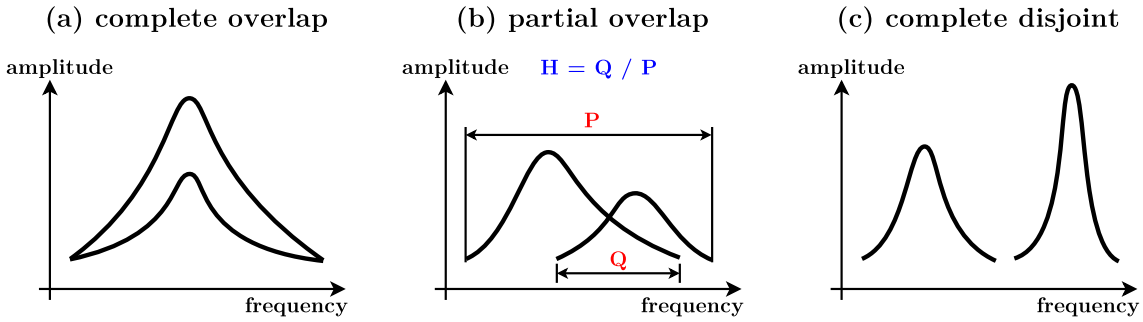

Figure 5.9: Different degrees of bandwidth overlap. The overlap H is normalized by the total spread P of the two mode's frequency bands. Here $H = 1$ means complete overlap as in (a), $0 < H < 1$ if frequency bands overlap as in (b). Otherwise $H \leq 0$ means complete disjoint bandwidths, as depicted in (c).

overlap Q by total span P is meant to map the cases with completely overlapping bandwidths (i.e. $f_1 = f_3$ and $f_2 = f_4$) to $H = 1$. For partially overlapping bandwidths, $0 < H < 1$, while disjoint bandwidths yield $-1 < H \leq 0$. Since the comparison only considers observed mixing pairs, a match between the VPF theory and experiments means that the predicted bandwidths yield $0 < H \leq 1$ for a particular observation. Because the non-zonal modes under consideration are half-frequency subharmonic, their predicted frequencies are doubled as their driving frequencies. In practice, it is these doubled driving frequencies that are compared to the frequencies of the harmonic zonal modes, for which the driving and oscillating frequencies identical.

5.3.2 Results

Results of comparison for the 188 mixing pairs are presented in figure 5.10. According to the definition, two predicted bandwidths with zero degree of overlap $H = 0$ indicate no mode mixing. Therefore for the histograms in figure 5.10 all data sets with $H \leq 0$ correspond to mismatching cases (i.e. mixing observed but

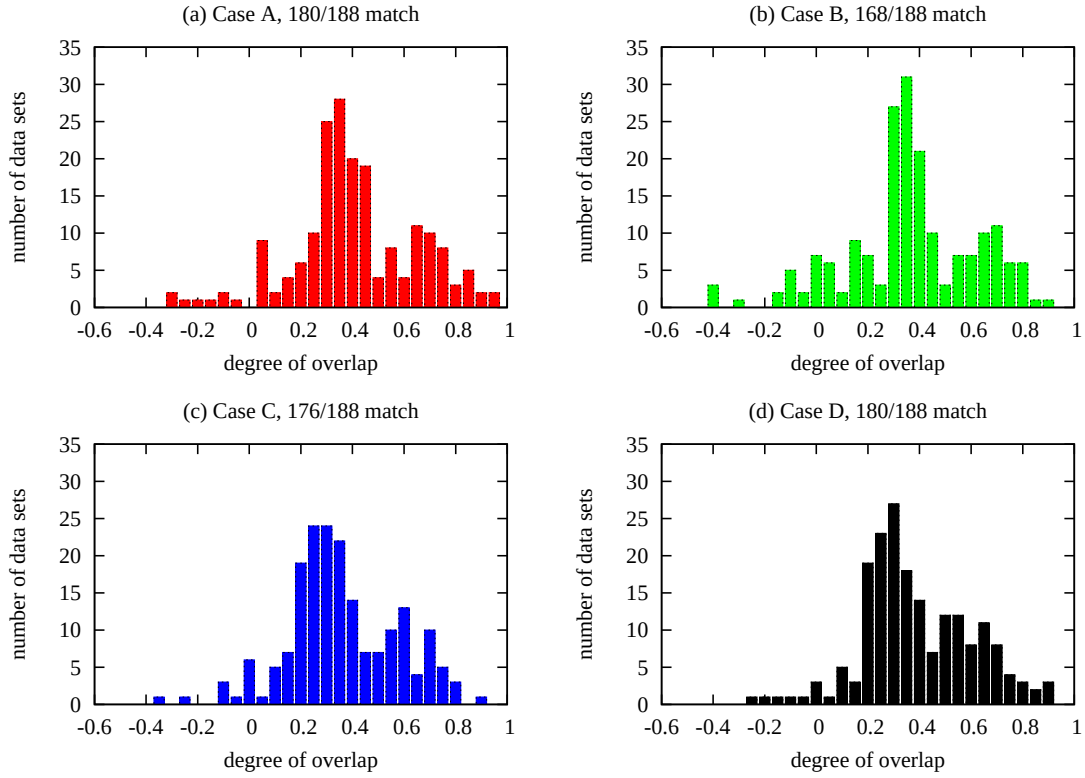

Figure 5.10: Results of comparing observed mixing modes to predicted bandwidths based on scheme III. Because H is rounded up, therefore the data sets with $H = 0$ are mismatching cases. Interpretation of the VPF theory in terms of scheme III yields at least 89% of matching between predictions and observations.

not predicted). Among different forcing cases, at least 89% of the observed mixing pairs are predicted. In the best cases (A & D) the matching rate is higher than 95%.

Despite the high percentage of matching between the VPF theory and experiments, the 5%∼10% mismatching cases are discussed as follows. Possible causes of the mismatch are:

a. neglecting contact-line mobility

b. neglecting evaporation

c. imprecision of contact-angle measurement

d. incorrect identification of mode shapes

e. presence of frequency hysteresis

Because contact-line motion is typically undetectable, zero mobility is assumed. Accordingly, the VPF theory predicts the highest possible resonance frequencies. On the other hand, because no length scale is available for keeping track of a drop's volume after vibration, a constant 20-μL volume is assumed and evaporation ignored. For data acquired at the end of each test, evaporation increases the resonance frequencies in experiments, yet the constant-volume assumption forces the theory to predict the same lower frequencies as if the drop remains 20-μL. In addition, because all images are recorded on the mechanical oscillator where no leveling device is installed, static side views used for contact-angle measurement may be slightly tilted. Manual measurement from these images using `ImageJ` further increases the uncertainty of contact angles, thereby affecting the predicted bandwidths. At the end of each test, both volume and contact angle of the drop are reduced. Although variation of contact angle can be quantified, that of the volume cannot with the experimental setup. Roughly half of the mismatch comes from observations at the end of a test, and these are most likely due to causes **a.**$\sim$**c.**. While comparing mismatching cases to the matching, a few (< 3) observations are found to be inconsistent. For example, [9, 1] mode is identified to mix with [12, 0] at contact angle $\alpha = 61^\circ$ but with [14, 0] at $\alpha = 63^\circ$. According to the observations, harmonic zonal modes reside far apart on the frequency spectrum. Although resonance frequencies sensitively vary with contact angle, a 2-degree difference is unlikely to cause such dramatic change of mode shapes. Therefore such mismatching cases are better interpreted as the results of incorrect mode identification. The larger the wave indices k and l, the more complicated the

mode shapes, and hence the more difficult to identify. In particular, $l = 0$ modes have a center peak at the north pole, and $l = 1$ modes have two alternating peaks close to the north pole. Distinguishing these mode shapes thus becomes tricky. Finally, the nonlinear experimental observations are compared to a linear theory that provides amplitude-independent bandwidths and truncates hysteresis. While the true bandwidths of modes overlap and broaden with forcing amplitude, the VPF theory is interpreted to ignore both by truncating response curves close to the valleys. Although the effect may be minor, such intrinsic distinction may also add to the possibility of misprediction.

The presented scheme of comparison indeed facilitates an adequate association of the VPF theory to experiments. Despite all these issues, only a small percentage of mismatch is encountered. Even though possible causes are identified for any mismatch, experimental results, such as mode shape identification, are not intended to be revised. This is because the comparison is meant to both properly relate theory to experiment and to test theory with experiments, but never to 'calibrate' experimental results with the theory. Without such false 'calibration', one may confidently expect to use the presented scheme as a useful means to interpret predictions from the VPF theory and then to anticipate the predictions to be realized in experiments.

As a final remark, the comparisons of mode crossing and mode mixing suggest that the forcing of case D most adequately describes the observations. Recall that case D assumes that the forcing acts upon a drop as a uniform acceleration. The assumption of acceleration provides adequate bandwidths for $k = 5$, 7 and 9 modes, and assuming uniform forcing achieves the highest percentage of matching for mode mixing. Although the exact mechanism of forcing remains unknown,

the implication from the comparisons may serve as useful guidance for further exploration.

CHAPTER 6

COMPOUND DROPS: STATICS & DYNAMICS OF LIQUID BALLOONS

6.1 Introduction

Motivated by various scientific and engineering interests, mechanics of water balloons is investigated from different aspects. The basic setup is depicted in figure 6.1(a), where hydrostatic force is applied on one side of an elastic membrane to inflate it into a balloon. One may consider the membrane as a capacitor, a separator, or a surface armor. Polymer balloons are excellent flexible capacitors for absorbing volume in response to pressure in microchannels[1]. As a separator, the membrane isolates the drop from contacting other materials. Such balloons have been used as transducers for exerting forces or providing geometric constraints in microfluidic channels[113]. Balloons are also used as substitute probes[37, 65] of purely solid hemispheres in Johnson-Kendall-Roberts test which measures surface adhesion of solid surfaces[55]. In addition, a more delicate application may be to allow active control of surface property. Suppose only the deformable part of the membrane is hydrophobic. Inflating the balloon enlarges the hydrophobic surface area, thereby changing the wetting property of the surface. If an array of such balloons with microns in diameter can be implemented on a substrate, then an active surface with locally adjustable wettability can then be implemented.

From the scientific perspective, it is interesting to compare statics and dynamics of sessile drops and balloons. For statics, the pressure-volume (P-V) response curves of different materials are depicted in figure 6.2. These P-V curves are typical predictions of various models[43], such as neo-Hookean[74], Mooney-Rivlin[91, 73]

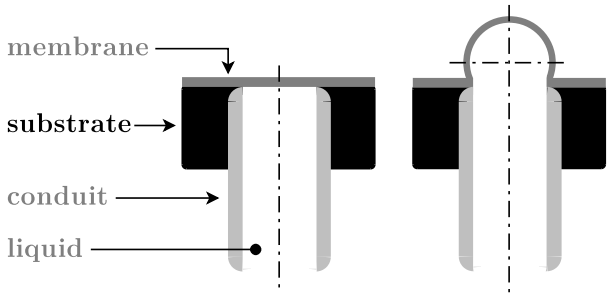

Figure 6.1: Schematics of a compound drop. The membrane forms a balloon when liquid in the conduit is pressurized. Suppose only the deformable part of the membrane is hydrophobic, inflating a balloon increases surface hydrophobicity by increasing the proportion of hydrophobic area.

and Ogden[79]. While the P-V curves of liquid drops possess one turning point, those of balloons either possess none or two turning points. A question is then raise: for balloons, how can these turning points and the unstable (descending) branch in between be created/destroyed? These unstable branches are scientifically interesting because the resulting spontaneous expansion under constant-force loading is a shared mechanical feature between certain balloons and liquid drops. Furthermore, when several balloons with such feature are connected and inflated[74], behavior of the system resembles the coarsening of capillary drops[104], such that only one balloons may change from sub- to superhemispherical at a time. Note that since the P-V curves of drops possess no ascending branch beyond the turning point, only one superhemispherical drop may survive, while multiple superhemispherical balloons can persist. All these similarities and differences between drops and balloons motivate the further pursuit of quasi-static experiments with balloons.

For dynamics, since inflated balloons can sustain a much larger liquid volume without collapsing, the membrane essentially 'adds' tremendous 'surface tension' to the drop. It is therefore interesting to see how such reinforced drops behave when subject to mechanical oscillation, and whether any mode shapes similar to those of sessile drops can be triggered. In fact, oscillatory motion of elastic membrane

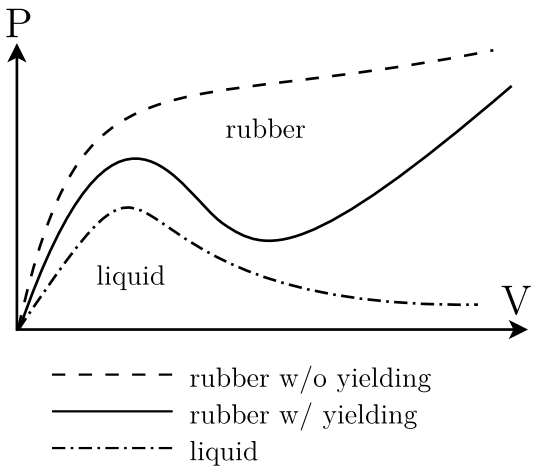

Figure 6.2: Typical $p - r$ curves for different continuum

similar to that of liquid drops and puddles has been reported. Fox and Goulbourne presented observations of axisymmetric deformations for a dielectrically actuated circular membrane[38, 39]. Zhu *et al.* predicted the resonance modes of a spherical balloon. Similar to the experiments with pinned water ring[57], Soares and Gonclalves[97] predicted the mode shapes of stretched annular membrane. These reported similarities between balloons and drops motivate the inquiry of how much more similar they may be. In fact, if balloons are dynamically similar to drops, they might be excellent experimental substitute for visualizing mode shapes of drops since these membrane-covered drops preserve partial spherical profiles up to centimeter scales. Motivated by these inquiries, rubber balloons are tested with the same vibration platform for drops.

6.2 Balloon statics: pressure-volume characteristics

The statics of balloons is probed and compared to drops in terms of the pressure-volume (P-V) response. While Young-Laplace equation (Eq.6.1) describes the P-V

responses drops, Mooney-Rivlin model (Eq.6.2) is commonly used for of rubber balloons:

$$p = \sigma\Big[\frac{1}{r_1} + \frac{1}{r_2}\Big] \tag{6.1}$$

$$p = 2s_+\frac{d_0}{r_0}\Big[\frac{r_0}{r} - (\frac{r_0}{r})^7\Big] \times \Big[1 - \frac{s_-}{s_+}\big(\frac{r}{r_0}\big)^2\Big] \tag{6.2}$$

where in Young-Laplace equation 6.2, σ is the surface tension, and r_1 and r_2 the principal radii of curvature of the droplet. In Mooney-Rivlin model[73, 91] (Eq. 6.2), p is the pressure, r_0 and r the balloon's undeformed and deformed radii, d_0 the thickness of the undeformed balloon, s_+ and s_- the elastic constants of the material. In this section, PDMS is the material of all rubber balloons in experiments. Note that the model requires a finite r_0 to predict finite pressure, the model is applicable to balloons with a curved undeformed configuration. In experiments, balloons are inflated from flat membranes. Therefore, Eq. 6.2 need to be revised before comparing to experiments. The P-V curves based on these models are depicted in figure 6.3. Note that Eq. 6.1 applies to the pressure jump across any liquid-gas interface. To be compatible with liquid balloons, the discussion here is restricted to sessile drops extruded out and remain on top of a needle, as shown in figure 6.4. According to Young-Laplace equation, pressure within a drop is inversely proportional to the drop's radius of curvature. Therefore a drop's pressure maximizes when the drop is hemispherical. In figure 6.4, the drop on the first column, second row possesses the highest pressure. In contrast, the response of balloons is more diverse: the P-V curves of balloons can possess either two, one or no turning point. Motivated by the scientific perspective of how turning points on P-V curves of balloons can be created and/or destroyed, the following investigation examines quasi-static responses of balloons with different geometric conditions and compare to those of drops.

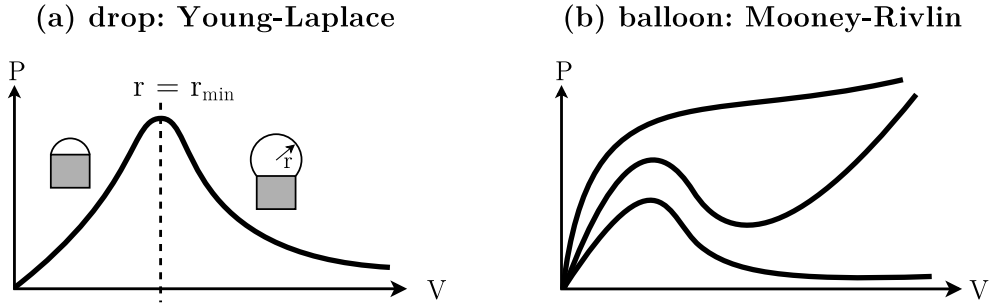

Figure 6.3: Pressure-volume response curves for liquid drops and rubber balloons

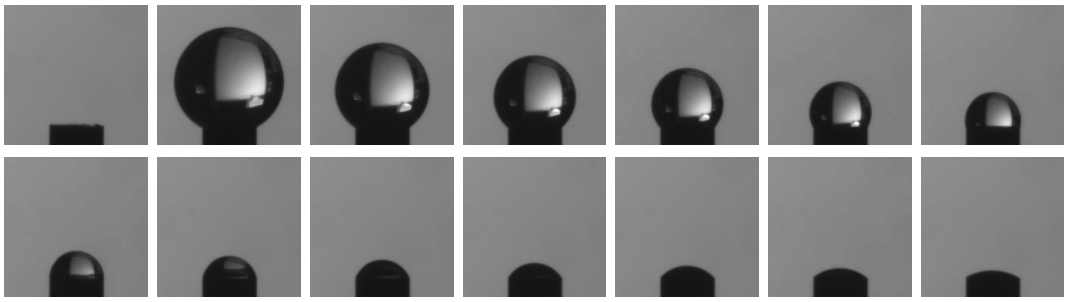

Figure 6.4: A sessile drop extruded from and stays on a needle. The outer diameter of the needle is 0.635mm.

More specifically, experiments of quasi-statically inflated balloons test a linear superposition model for a balloon's effective surface tension. The postulated model is depicted in figure 6.5. The model considers the liquid-membrane interface and the membrane as two springs. As the balloon inflates, the two springs deform by roughly the same amount. Therefore they are in parallel. Accordingly, the model postulates the effective surface tension of the balloon as the sum of elasticity and surface tension. Thus according to figure 6.5, covering a drop with the thin membrane is mechanically equivalent to summing up their response curves. Suppose a thicker membrane of the same rubber exhibits a monotonic pressure-volume curve, and its thickness can be reduced so that the effects of elasticity and surface tension are on the same order. A response curve with either no turning point (for strong elasticity) or two turning points (for weak elasticity) can then be created by simply adjusting the membrane thickness. To test the postulated model, the experiments

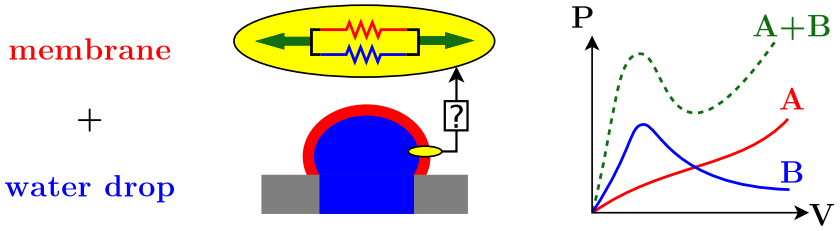

Figure 6.5: Postulated model: effective surface tension of a membrane-covered drop (balloon) as the sum of the solid elasticity and liquid surface tension

here require sufficient sensitivity of apparatus for measuring capillary pressure of droplets.

The response curves of drops and balloons are acquired from direct measurement. Schematics of the hardware setup is illustrated in figure 6.6. The pressure is measured by a piezo pressure sensor (part number 4262A2D5ARB05B0, by Kistler Instrument Corp., Waddington, NY). For water drops, a needle (outer diameter 0.635mm) is installed on the manifold. The drop is extruded from the needle. As the drop slowly evaporates, side-view images are captured and pressure readings recorded. Volume of drops are calculated from images and associated with measured pressure. For balloons, the volume is directly controlled by a glass syringe (model: Gastight 1700, 250μL, RN termination, by Hamilton Company, Reno, Nevada). A balloon is inflated manually in discrete steps and the pressure is recorded for each step of inflation. Snapshots of an inflating balloon are presented in figure 6.7. The balloon consists of a PDMS membrane covalently bonded to a PDMS substrate. Hydrostatic pressure is applied from a glass tubing from the bottom to inflate the balloon upwards. Detailed preparation protocol of PDMS balloons is reported in Appendix G.

Results of measurement are presented in figure 6.8. For a superhemispherical drop evaporating on a needle (diameter = 0.635mm), the volume decreases and

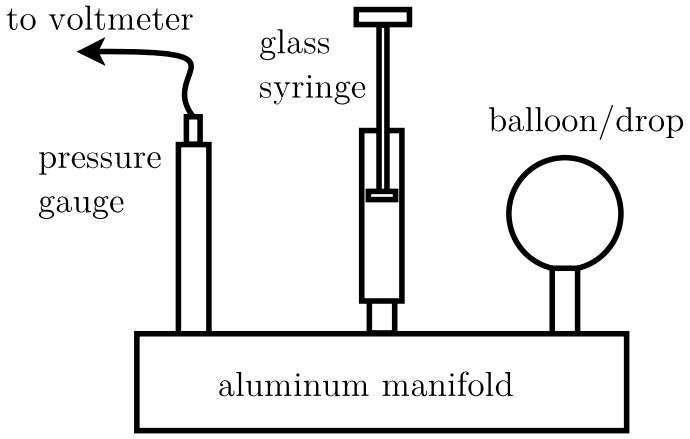

Figure 6.6: Experimental setup for measuring pressure-volume response curves.

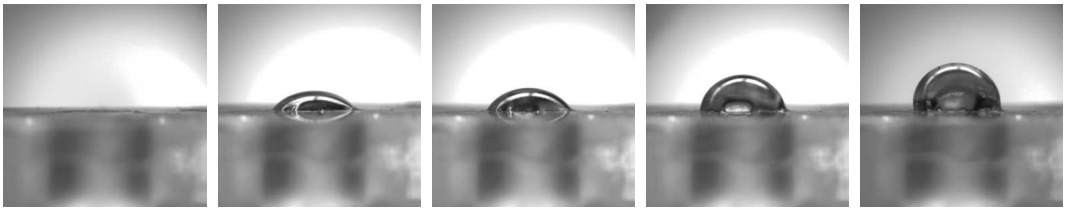

Figure 6.7: Side-view images of a PDMS balloon inflated by water. The pressure grows monotonically with the volume. The pinned edge of the balloon is roughly 5mm. From left to right, the volumes are 0mL, 0.05mL, 0.1mL, 0.15mL and 0.2mL.

the pressure increases. The pressure maximizes when the drop roughly becomes hemispherical. In figure 6.4, the drop in the bottom row, left-most column exhibits the maximum pressure among others. The pressure of subhemispherical drops decreases with volume. The result suggests that the apparatus possesses the sufficient precision for testing the postulated model of balloons.

To probe the sufficient membrane thickness for the postulation, PDMS balloons with different thicknesses are tested. Consequently, the P-V curves of rubber balloons change over time. Results are presented in figure 6.8. To be consistent, only the P-V curve from the first inflation of each brand new sample is reported here. This is because elastomeric material typically exhibit Mullins effect[80, 30, 75, 27], in which the material softens when loaded repeatedly. From the results, thicker

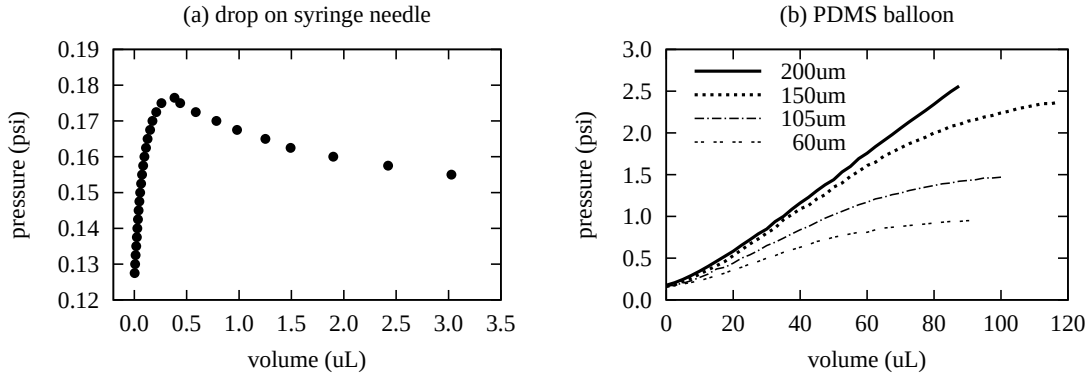

Figure 6.8: Measured pressure-volume response curves for (a) drop and (b) PDMS balloon.

samples exhibit monotonic P-V curves. While P-V curves remain monotonic for thinner balloons, these curves begin to exhibit inflection points. The investigation here is certainly incomplete, and further exploration requires reduction of membrane thickness. However, further reducing membrane thickness is technically impossible since it inevitably results in defective samples. Hence further investigation has been discontinued.

6.3 Balloon dynamics: resonance

From the dynamical perspective, mechanics of balloons are characterized in terms of the resonance result from mechanical vibration. Specifically, the investigation tests whether balloons exhibit mode shapes similar to those of vibrated drops and if so, how the resonance frequencies of balloons and drops compare.

The experiments of balloon dynamics test the resonance of natural latex rubber balloons. Rubber membrane samples are prepared by spin coating (Appendix H). Once a membrane is clamped between two orifices (diameter $\approx$ 15.6mm) and inflated with water into a balloon, it is vibrated on the mechanical oscillator (Ap-

pendix A). Volume and pressure are not precisely prescribed in these preliminary experiments. However, balloons are always superhemispherical. The maximal diameter of balloons is approximately 18mm. Such physical size allows direct visual inspection of mode shapes by naked eyes. As presented in the following context, totally six zonal modes, two sectoral and one tesseral are observed.

6.3.1 Zonal modes of balloons

Zonal modes of balloons can be generated with small forcing accelerations. Side-view images of mode shapes are presented in figure 6.9. Extended exposure time is adopted to accumulate all lobes and nodes of an oscillating balloon. Because of the long exposure time, ambient light in the room is sufficient and hence no extra lighting is employed. Bandwidths of these modes are typically 20 Hz. The mode shapes in figure 6.9 are identified with the same scheme as the mode shapes of sessile drops, with [2, 0], [4, 0], ..., [12, 0] possessing 2, 4, ..., 12 nodes in their side views.

Note that all modes but [2, 0] are slightly defective. In figure 6.9, only [2, 0] exhibit flat profiles under the center peaks. However, perfectly axisymmetric modes must exhibit a flat outline under the center peak, as the side view of nodal circles is a horizontal flat line. If viewed from an angle, the side view of the nodal circle may appear to be slightly convex, but not concave. The concaving outlines imply warping of the axisymmetric rings of other modes. A comparison of such convexity/concavity of the shapes is provided in figure 6.10. Such warping possibly implies the presence of certain non-axisymmetric modes. The speculation motivates further pursuit of non-axisymmetric mode shapes of balloons, as presented in the following context.

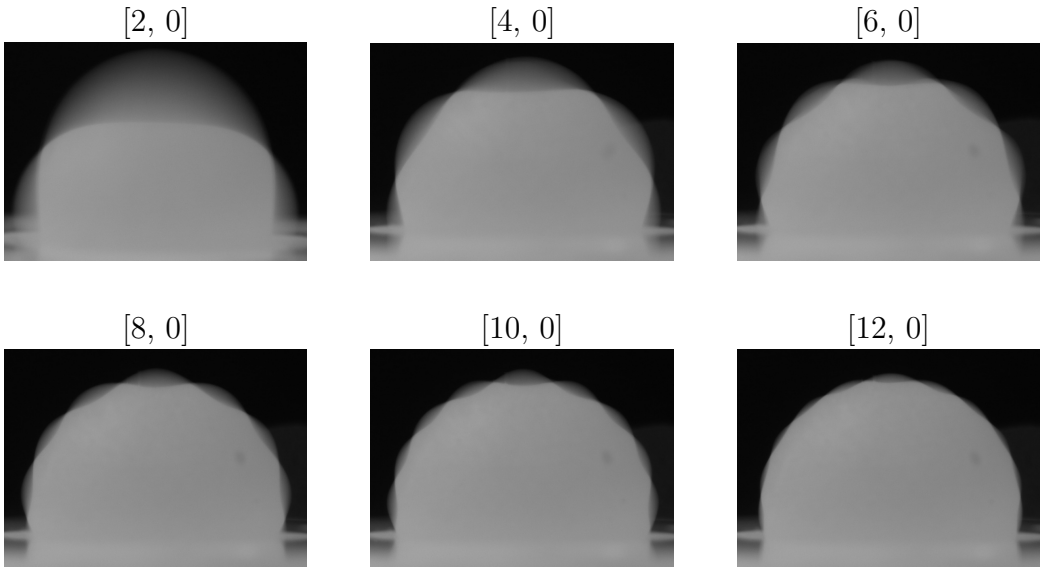

Figure 6.9: Zonal modes of an oscillating balloon.

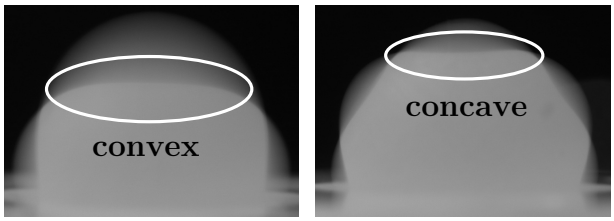

Figure 6.10: Comparison of the balloon's [2, 0] and [4, 0] modes. While [2, 0] mode shows a convex base line under the center peak, the [4, 0] mode shows a convex base line. The concavity in the latter possibly motivates the speculated presence of certain non-zonal modes.

Compared to others in figure 6.9, [2, 0] mode most effectively amplifies the forcing. From figure 6.9, the maximum displacement of [2, 0] roughly equals the balloon's pinning radius, while the forcing itself is visually undetectable. As [2, 0] mode massively amplifies the forcing, it is an excellent candidate for implementing mechanical amplifier.

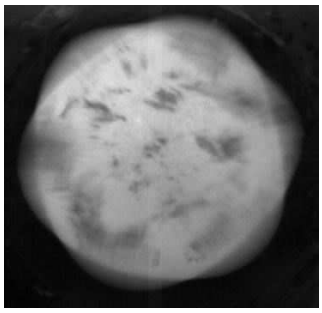

Figure 6.11: An oscillating drop exhibiting a six-vertex start pattern from the top view.

6.3.2 Non-zonal modes of balloons

Similar to vibrated sessile drops, rubber balloons also exhibit non-zonal modes. For example, figure 6.11 shows a six-vertex star pattern of an oscillating balloon. Again, the 18-mm diameter of the balloon makes the shape clearly visible by naked eye. To further acquire snapshots of the mode by high-speed imaging, however, lighting with sufficient intensity must be provided.

Subsequent experiments with non-zonal modes of balloons adopt an auxiliary light source. Because latex rubber balloons are opaque and contain water, projecting light upwards from inside the balloon is ineffective and impractical. Consequently, an auxiliary lighting is designed to illuminate a balloon from multiple sides for acquiring top-view snapshots. As depicted in figure 6.12, multiple LEDs are employed to illuminate from different sides of a balloon. An image sequence acquired at 5000 frames per second for the same 6-vertex mode is presented in figure 6.13. The alternating triangular shape in these snapshots clearly indicate a sectoral [3, 3] mode. The arbitrary patches of patterns on the balloon are those painted with water-resistant ink, originally meant to help identifying mode shapes.

For vibrated balloons, in total three non-zonal modes are observed. In addition

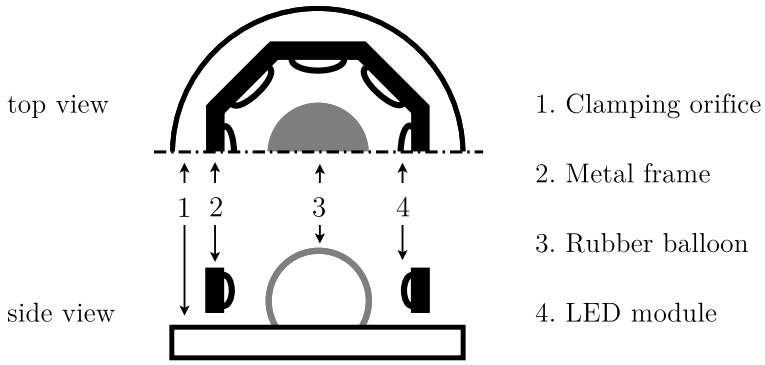

Figure 6.12: Light source and resulting top-view snapshot of a balloon's non-zonal mode.

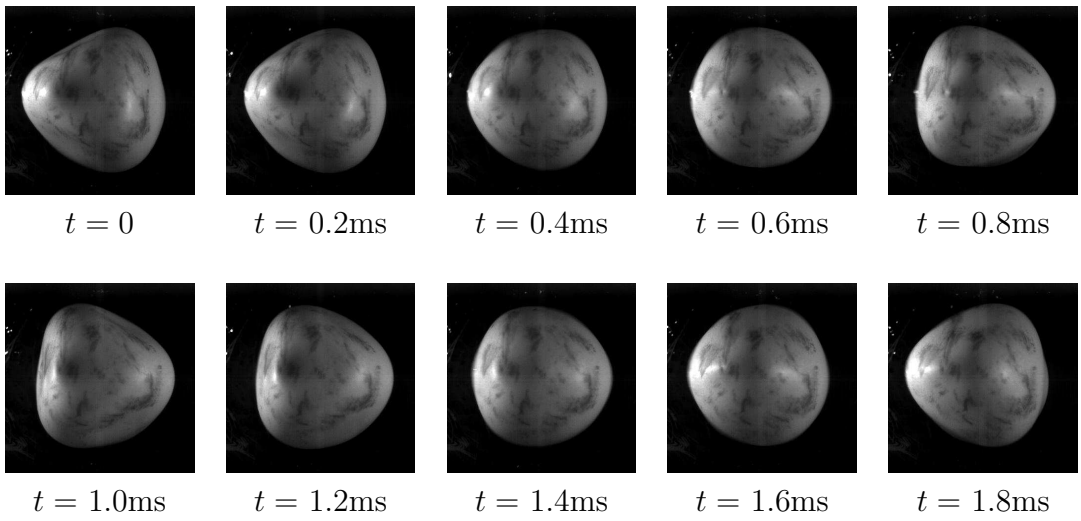

Figure 6.13: Shape evolution of a balloon's [3, 3] mode. Forcing frequency: 855 Hz.

to the [3, 3] mode already presented, the other sectoral mode is [4, 4], as presented in figure 6.14. The mode shape is identified from the alternating pair of squares at $t = 0$ and 1.0ms. The third mode is [4, 2], a tesseral mode. The mode features two pairs of alternating bar patterns. Oscillation of the [4, 2] within one period is presented in figure 6.15. Although all these shapes are clearly recognizable to the naked eyes, the snapshots for [4, 2] possibly don't clearly illustrate the bar on the upper layer. Top- and side-view schematics of [4, 2] mode are depicted in figure 6.16 to clarify the observation.

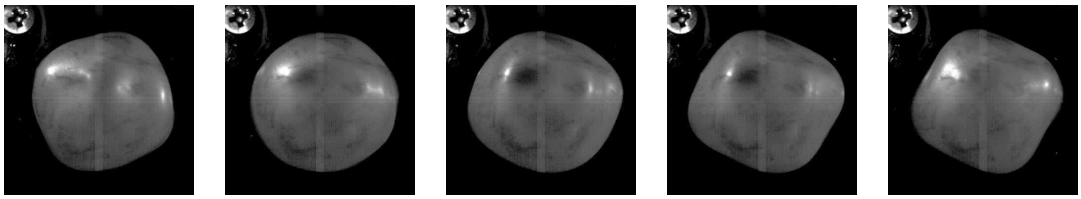

$t = 0$ $t = 0.2$ms $t = 0.4$ms $t = 0.6$ms $t = 0.8$ms

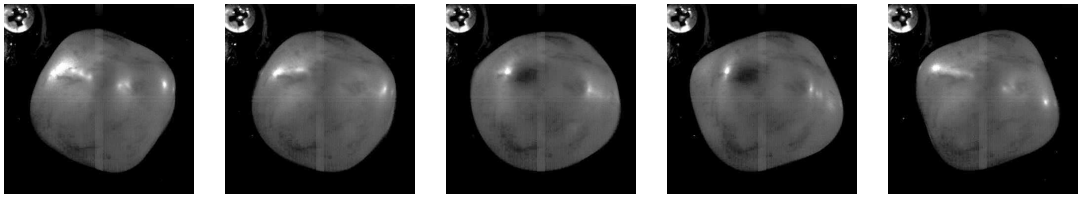

$t = 1.0$ms $t = 1.2$ms $t = 1.4$ms $t = 1.6$ms $t = 1.8$ms

Figure 6.14: Shape evolution of a balloon's [4, 4] mode. Forcing frequency: 900 Hz.

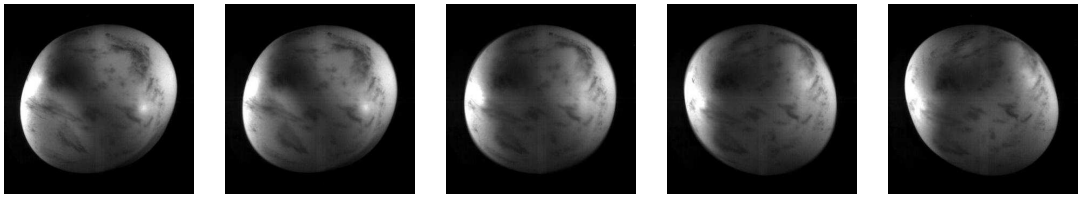

$t = 0$ $t = 0.2$ms $t = 0.4$ms $t = 0.6$ms $t = 0.8$ms

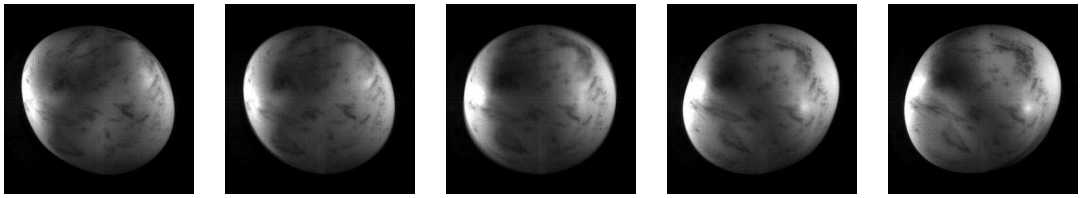

$t = 1.0$ms $t = 1.2$ms $t = 1.4$ms $t = 1.6$ms $t = 1.8$ms

Figure 6.15: Shape evolution of a balloon's [4, 2] mode. Forcing frequency: 1113 Hz.

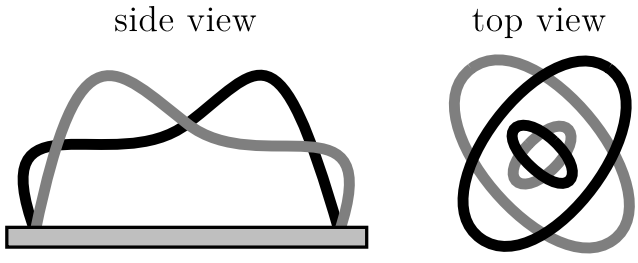

Figure 6.16: Schematic of a [4, 2] mode

The experimental observations indicate various similarities between drops and balloons. First of all, both exhibit zonal and non-zonal modes. In addition, a one-to-one correspondence apparently exist between the mode shapes of balloons and drops. Furthermore, compared to tested sessile drops, the balloons are much larger yet the same modes resonate at much higher frequencies. Therefore from the dynamic perspective, balloons can simply be regarded as drops with a much higher effective surface tension. In these experiments, hydrostatic pressure and equatorial diameter of balloons are roughly 2.5 psi ($\approx 17 \times 10^3 N/m^2$) and 18mm. Based on these parameters, the effective surface tension σ_e can be obtained by

$$\pi \times 0.009^2 \times 17 \times 10^3 = 2\pi \times 0.009 \times \sigma_e, \qquad \Rightarrow \sigma_e = \frac{1}{2} \times 0.009 \times 17 \times 10^3 \approx 76.5 \quad (6.3)$$

Note that the surface tension of water is 0.072 (N/m). Therefore from the dynamic perspective, the tested balloons are drops with an effective surface tension roughly 1000 times higher than that of water.

CHAPTER 7

FUTURE WORK

7.1 Footprint dependence of sessile drops' resonance

From a scientific perspective, it is interesting to explore how a drop's footprint geometry influences its resonance. Because liquid drops naturally exhibit circular or elliptical footprints on solid surfaces, previous experiments primarily investigate drops with circular/spherical geometry. Results are compared to theories modeling spherical (Rayleigh-Lamb theory) or partial spherical (Bostwick-Steen inviscid and VPF theories) drops, as presented in previous chapters. For resonance of drops with circular footprints (circular drops), these experiments fully characterize the mode shapes, frequency and amplitude responses, and VPF theory reasonably agrees with observations. Recall that pinning sites on substrates effectively impose prescribed shapes on footprints of drops. The technique allows exploring the resonance of, for example, drops with square footprints (square drops). A qualitative comparison of mode shapes for circular and square drops is presented in figure 7.1. Each column associates similar mode shapes of the two kinds of drops. For example, the square footprint deforms the axisymmetry of [6, 0] mode into a square-symmetric shape. For [4, 2] mode, the square footprint 'rectifies' the original θ-shape into an H-shape aligned with the sides. From these results, square and circular drops apparently exhibit similar mode shapes. In addition, the square symmetry for square drops is equivalent to the axisymmetry for circular drops: once the symmetry is lost, the mode is subharmonic. Among all modes in figure 7.1, only [6, 0] is harmonic. Based on these observations, a one-to-one correspondence of resonance modes between square and circular drops is speculated.

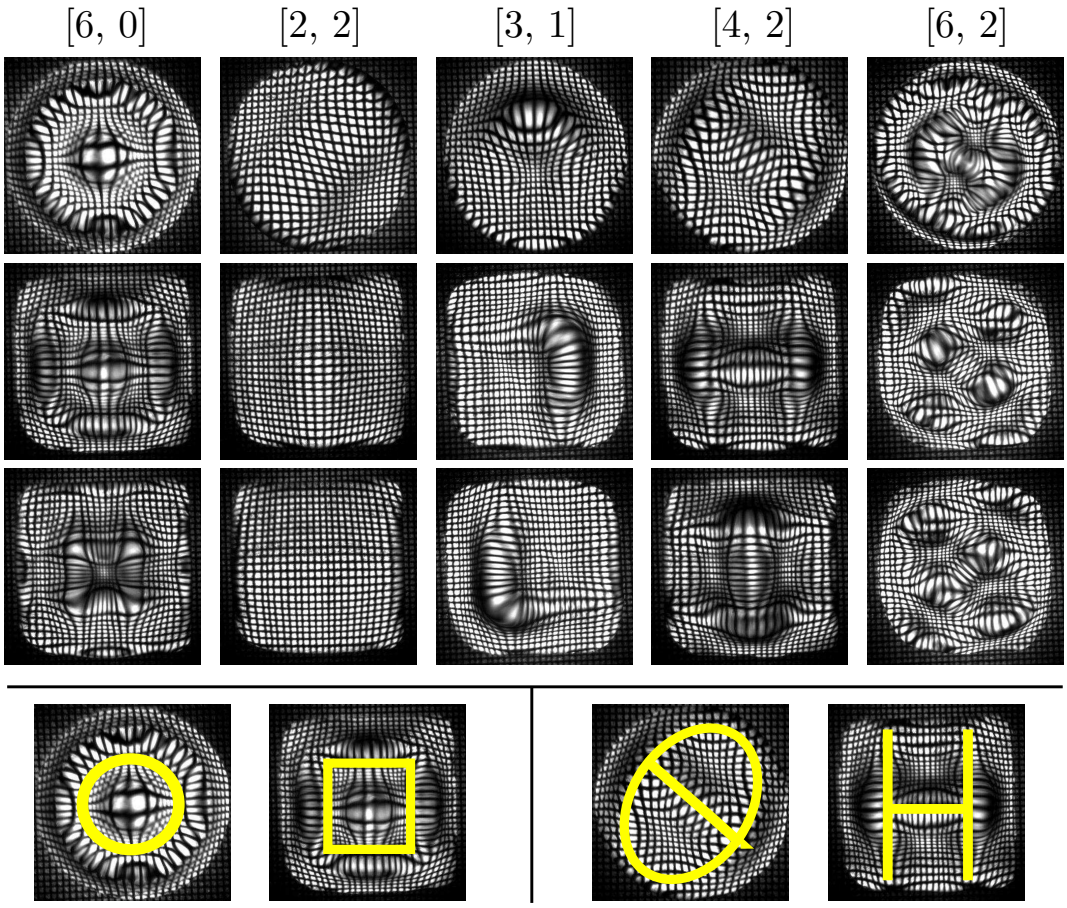

Figure 7.1: Comparing mode shapes of 'square' and 'circular' drops. The square footprint of a drop apparently deform the axisymmetric [6, 0] mode into a square symmetric shape. The θ-shaped [4, 2] mode is deformed into an H shape with patterns aligned with the sides. While non-axisymmetric modes of the circular drop are subharmonics, so are the ones without square symmetry for the square drops.

Therefore from the experimental perspective, it is interesting to further characterize exactly how a drop's footprint geometry affects its resonance. For modeling with theories, it is important to investigate how BS inviscid and VPF theories compare with observed resonance of drops with non-circular footprints and further implement schemes, if possible, to extend the theories to such drops.

7.2 Resonance of Sessile Drops and Faraday Waves

Resonance of sessile drops resembles Faraday waves of cylindrical liquid baths in several aspects. For example, both exhibit harmonic and subharmonic waves, and the emergence of subharmonics typically follow certain symmetry breaking phenomena. In fact, a one-to-one correspondence is expected to exist between mode shapes of sessile drops and Faraday waves, since both are standing waves on liquid-gas interfaces with circular boundaries. Obviously the two phenomena are closely related. From the scientific perspective, it is interesting to further quantitatively associate the equivalent mode shapes of drops to Faraday waves.

Comparing Faraday wave and resonance of sessile drops is equivalent to investigating the resonance of liquid puddles with different equilibrium profiles. In general, a liquid puddle may possess finite curvature and depth. As depicted in figure 7.2, sessile drops are special cases of puddles with zero depth below contact lines. Consequently, drops always possess finite curvature because of their zero depths below the contact lines. The other family of special cases is puddles with flat free surfaces. The resonance of flat free surfaces is Faraday wave. Therefore by varying the free-surface curvature and depth of a puddle and probing their resonance, Faraday wave and modes of sessile drops can be related. For sessile drops with circular footprints, effects of a drop's curvature on its resonance frequencies is fully investigated as presented chapter 3. Future exploration shall start with the effects of puddle depth upon resonance to generalize the results of the current study to Faraday waves of cylindrical liquid puddles. To further generalize to other geometries, a similar parametric study can be conducted to compare resonance of 'square' drops in section 7.1 to liquid puddles with rectangular reservoirs of different depths. From the scientific perspective, these future explorations

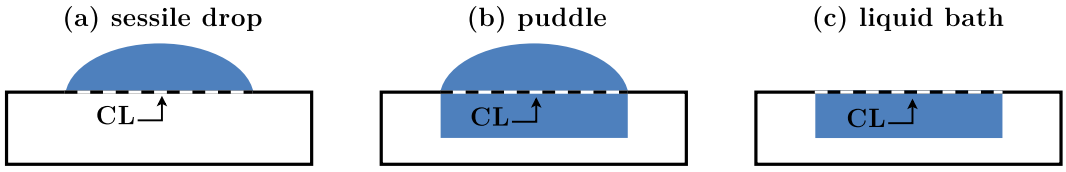

Figure 7.2: Schematics of a sessile drop and a liquid bath: The former and the latter are liquid puddles with zero and finite depth below the contact line. CL ≡ contact line.

link the separate studies of drops and Faraday waves in the literature and provide more insight to resonance of free surface waves in general. For engineering applications, these studies may facilitate more active control of pattern selection for liquid atomization[105], suspension collection[109] and ordered self-assembly of nanoparticle on free surfaces[6].

7.3 Dynamics of pinned superhemispherical drops

The implementation of substrate B (Appendix F) allows exploring dynamics of pinned superhemispherical drops. In practice, vibrated superhemispherical drops tend to randomly translate if the drop is not pinned. Also because superhemispherical drops bring the underlying mesh out of focus, their mode shapes are difficult to identify. While the identification issue is pending, pinning sites on substrate B effectively secure superhemispherical drops for preliminary investigation. Various phenomena unique to superhemispherical drops are observed. Indeed, the insistence[1] of carefully examining vibrated superhemispherical drops shed light on scientifically interesting families of dynamics which possibly has never been explored.

[1]Thanks to Prof. Steen's guidance

7.3.1 Anticipated phenomena

Originally, mode mixing phenomena similar to those for subhemispherical drops are anticipated for superhemispherical drops. Recall that for subhemispherical drops, the most typical mode mixtures are those of a harmonic zonal mode and a half-frequency subharmonic nonzonal mode. Superhemispherical drops exhibit similar behaviors and, in fact, they almost always do so: It is apparently inevitable that superhemispherical drops mix nonzonal modes with at least one zonal mode. In other words, it is quite difficult to trigger any pure non-zonal mode for superhemispherical drops. A typical observation is presented in figure 7.3, where an oscillating superhemispherical drop is exhibiting the mixture of a [5, 5] mode and an unknown zonal mode. Take images at $t = 0.8$ and 3.2ms as examples. The pentagonal pattern is the signature of [5, 5] mode, while the convex center suggests the presence of a certain zonal mode. From $t = 0.8$ to 3.2ms, the convex center of the drop implies that the zonal mode completes one period. However, the [5, 5] mode completes only half a period, since the two images exhibit pentagons rotated by 180°. Therefore the zonal mode oscillates at twice the frequency of the [5, 5] mode. It remains to identify the harmonic types of these modes by examining the lower-frequency signal from these top-view snapshots.

The lowest frequency conveyed by figure 7.3 is estimated according to Appendix D. The estimated lowest frequency f_o is, according to $N_c = 8$ and $N = 179$ in figure 7.4,

$$f_o \approx 5000 \div 179 \times 8 \approx 223.46(Hz) \tag{7.1}$$

which means that with respect to the 447-Hz forcing, [5, 5] is a half-frequency subharmonic mode, while the unknown zonal mode is harmonic. The detail in figure 7.4 resembles the typical results for subhemispherical drops. Although the

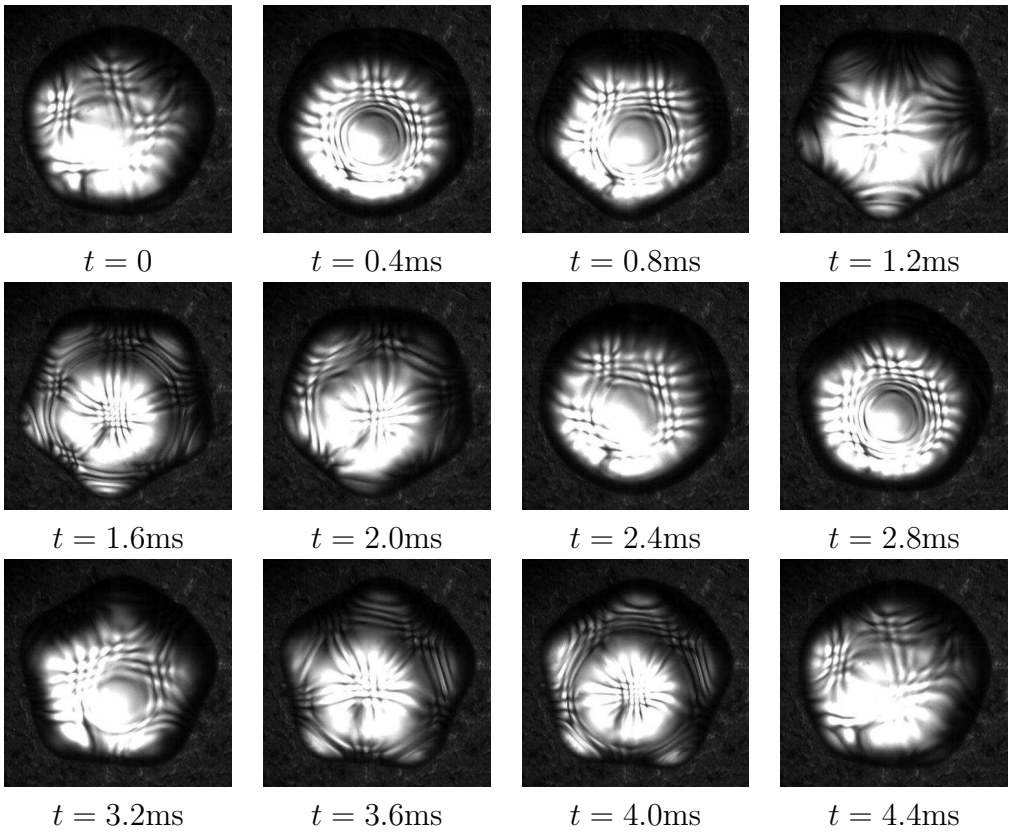

Figure 7.3: Top-view snapshots of an oscillating superhemispherical drop exhibiting the mixture of a [5, 5] mode and an unknown zonal mode. Drop volume: 18μL. Forcing: 447Hz, 12g. Frame rate: 5000fps.

difference norm z (cf. Appendix D) alone fully resolves the drop's motion in figure 7.3, it becomes insufficient for more complex mixing phenomena of superhemispherical drops. It turns out that these more complicated mixing modes in the following context may require both frequency analysis (FFT) and a much longer data sequence to fully decipher.

7.3.2 Harmonic sectoral mode

While nonzonal modes of subhemispherical drops are always half-frequency subharmonics, one harmonic sectoral mode is observed for superhemispherical drops.

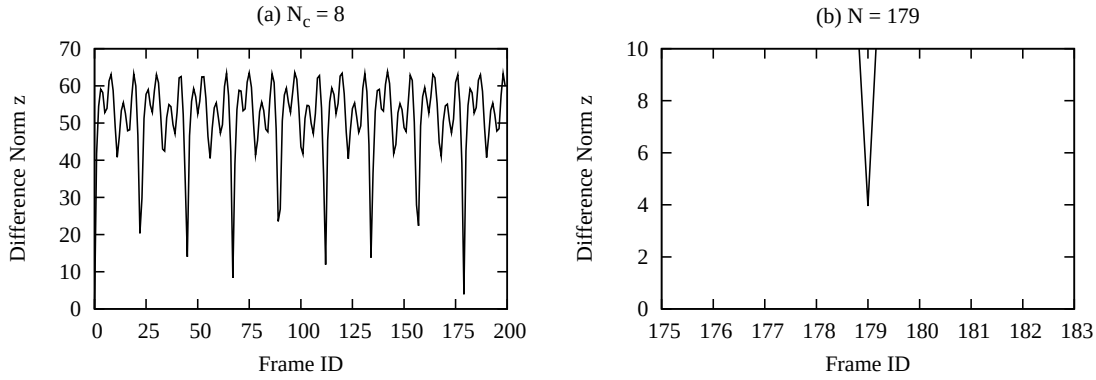

Figure 7.4: Evolution of difference norm for the image sequence of figure 7.3.

The observation is presented in figure 7.5, where a [7, 7] mode is mixing with an unknown zonal mode. Among the snapshots, those for $t = 0.4$, 0.8 and 1.2ms possess a heptagonal shape, while those for $t = 2.0$, 2.4 and 2.8 ms exhibit conjugate heptagons of the former. The heptagons are signatures of a sectoral [7, 7] mode. Further inspection suggests that the center part is convex for the first four snapshots but concave for the latter four. The concave/convex deformation at the drop's center suggests the presence of a zonal mode. It is typical for a sectoral mode to mix with a zonal mode. However, the mixing modes in figure 7.5 apparently oscillate at the same frequency. This is manifest from the fact that the two conjugate heptagons respectively synchronize with the concave and convex phases of the zonal mode. Recall that for subhemispherical drops, subharmonic modes typically compete colonize the bandwidths of one another hysteretically, and only zonal modes exhibit harmonic oscillation. Accordingly, figure 7.5 suggests one of the two anomalous phenomena: either a pair of subharmonic zonal and non-zonal modes coexist without competition, or a harmonic sectoral mode is triggered. It remains to detect the lowest frequency in the image sequence. Figure 7.6 shows the result of frequency estimation, according to which the lowest frequency in the

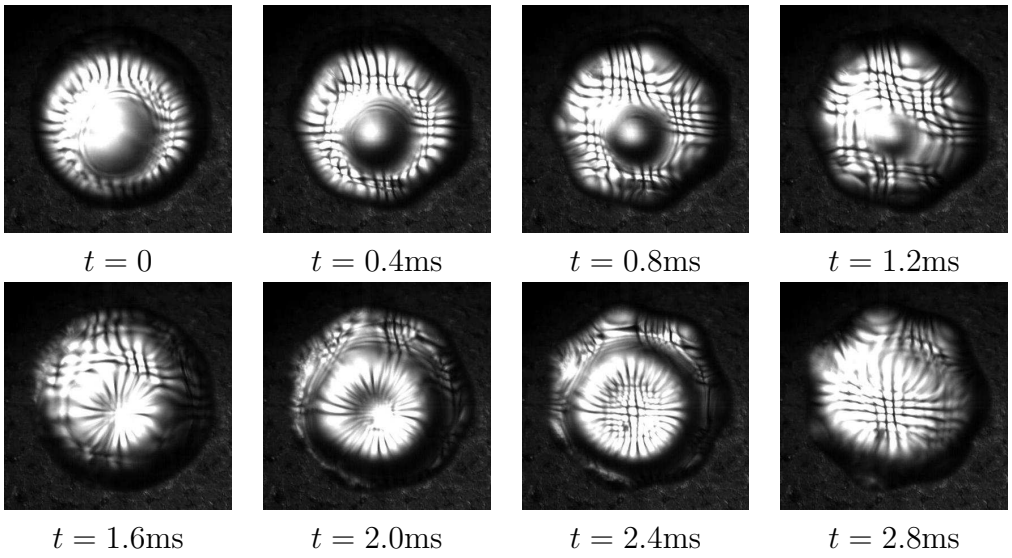

Figure 7.5: Top-view snapshots of an oscillating superhemispherical drop exhibiting a harmonic (7, 7) mode mixed with a harmonic zonal mode. Volume: 26μL. Forcing: 309Hz, 10g. Frame rate: 5000fps.

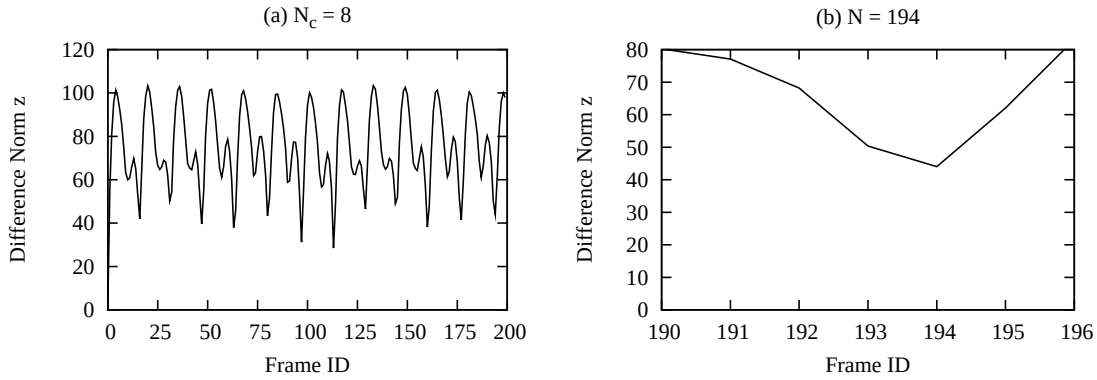

Figure 7.6: Evolution of difference norm for the image sequence of figure 7.5.

image sequence is, with $N_c = 12$ and $N = 194$,

$$f_o = 5000 \times 12 \div 194 \approx 309.28 \tag{7.2}$$

which is technically identical to the forcing frequency. Therefore both [7, 7] and the unknown zonal modes are harmonic. The harmonic zonal mode is common in all experiment. However, the [7, 7] mode is the only harmonic non-zonal mode observed in any experiment, and only triggered for superhemispherical drops.

7.3.3 1/14-Frequency subharmonic zonal mode

In addition to half-frequency subharmonic modes, superhemispherical drops also exhibit at least one other type of subharmonic zonal mode. The new type of subharmonic zonal mode is discovered when a vibrated superhemispherical drop simultaneously exhibit oscillatory motions with two distinct time scales. From the top view, axisymmetric fine ripples oscillates at a higher frequency on the drop surface, while the drop periodically brightens and darkens at a much lower frequency. A careful inspection of the latter reveals that the brightness variation is associated with the expansion and contraction of the drop's equator, such that the drop becomes brightest (darkest) when its equator expands (contracts). Recall that one image sequence of ten frames is sufficient for illustrating the mixture of a harmonic and a half-frequency subharmonic modes (cf. figure 5.3). For the new type of subharmonic zonal mode, however, the same image sequence must be examined by re-sampling with two different time scales. For the axisymmetric fine ripple which oscillates faster, snapshots for approximately one period of oscillation are presented in figure 7.7. Among the images, those at $t = 0$, 0.125, 0.878, 1.00 and 1.13ms clearly exhibit convexity at drop's center, while those at $t = 0.376$, 0.501 and 0.627ms show a concave shape. Within 1.13ms and at 0.125-ms time scale, the apparent size of the drop remains unchanged, and the only observable deformation is the axisymmetric fine ripple, which is the signature of a zonal mode.

A different oscillatory motion is noticed when the image sequence is investigated at a longer time scale. By examining the image sequence at a 1-ms time scale for 14ms, a slower oscillation is identified. In figure 7.8, the drop starts at $t \approx 0$ with a relatively small apparent size from the top view, gradually grows and maximizes at $t \approx 7$ms, and then shrinks and minimizes again at $t \approx 14$ms. The snapshots

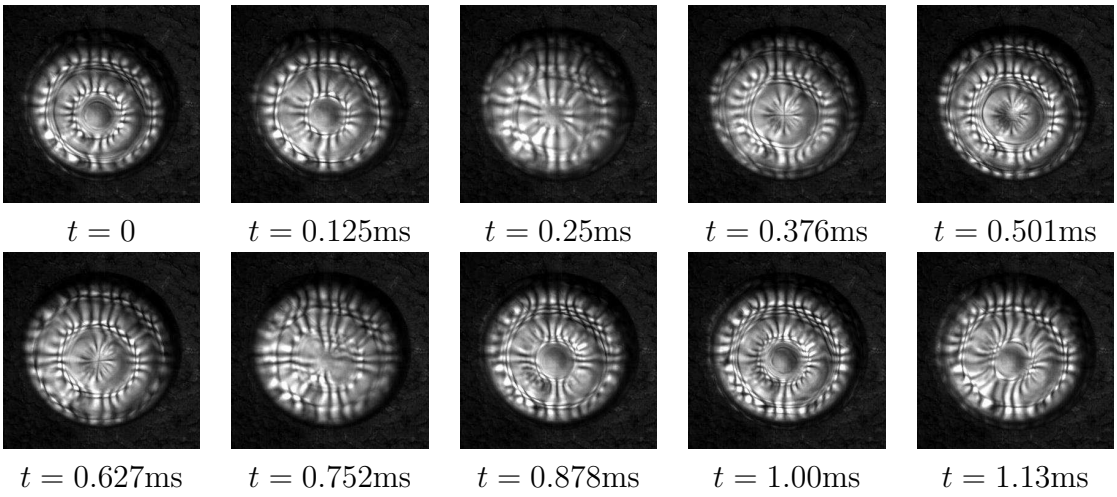

Figure 7.7: Top-view snapshots showing the axisymmetric fine ripples oscillating on the surface of a superhemispherical sessile drop. The ripples are the signature of a zonal mode. Within 1.13ms, little variation of the drop's apparent size is noticeable, and only the oscillation of the fine axisymmetric ripple is observed. Drop volume: 14μL. Forcing: 958Hz, 20g. Frame rate: 7975fps.

of $t = 0$ and $t = 14$ms are relatively dark, while those of $t = 5$, 6 and 7ms are much brighter. These snapshots suggest the coupling between the oscillations of a drop's apparent size and its brightness, with the maximum size correspond to the maximum brightness. In experiment, it is the vigorous oscillation of brightness that attracts the attention and motivates further investigation. However, what is the drop doing when it exhibits such significantly slower oscillation?

Side view snapshots of the drop answer the question. As shown in figure 7.9, the drop starts up with a flat 'crouching' pose at $t = 0$, gradually grows in height which maximizes around $t =$7ms with a 'standing' pose, and subsequently decreases back to the 'crouching' pose. According to the side view, obviously the 'crouching' and 'standing' of the drop cause the variation of its apparent size from the top view. The variation of drop's shape necessarily changes transmission of projected light from below, thereby causing the oscillation of overall brightness in figure 7.8. With evidence presented in figure 7.8$\sim$ 7.9, the coexistence of (at least) two modes is

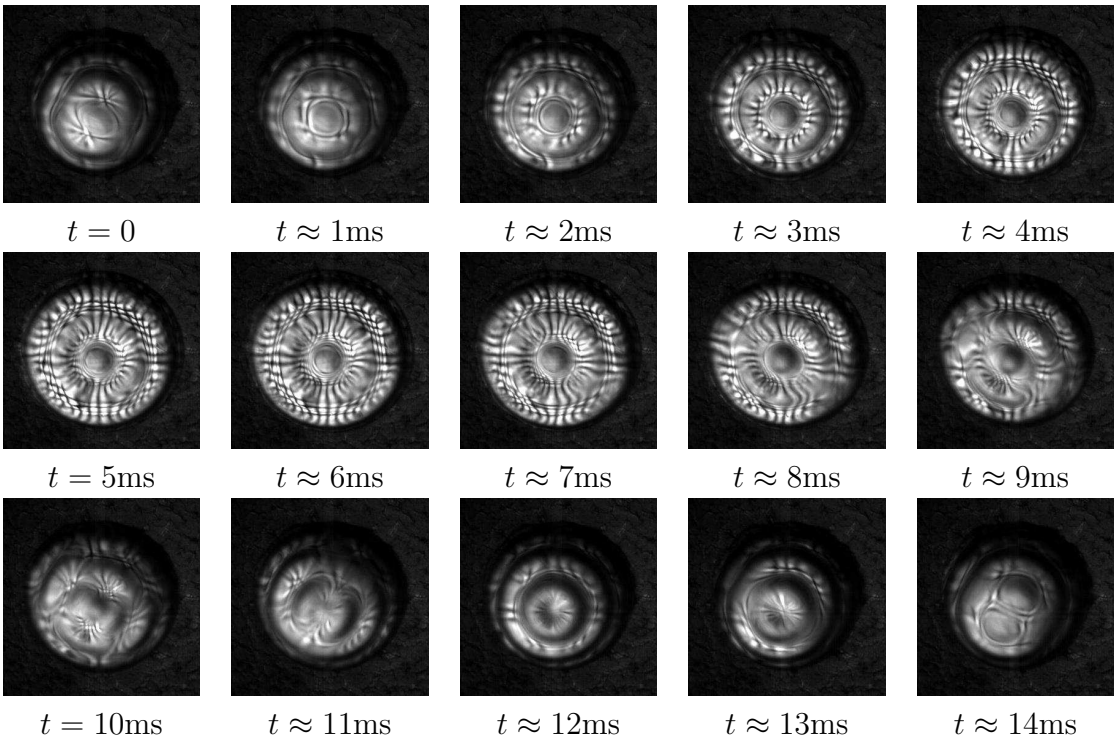

Figure 7.8: Top-view snapshots of a drop exhibit varying apparent sizes. Within the 14-ms time period, noticeable variation of the drop's apparent size is found together with the change of overall brightness.

justified.

Again, the interesting aspects here are both the extremely slow crouching-standing motion, and its mixture with the much faster axisymmetric fine ripples. For sessile drops of millimeter scales and mechanically oscillated at 958Hz, zonal modes similar to those in figure 7.8 are typical. However, the crouching-standing oscillation has never been observed. A first natural inquiry then is how the faster and slower modes synchronizes with the driving signal. Therefore it remains to identify the harmonic type of the axisymmetric fine ripple and the crouching-standing oscillation of the drop. Results of frequency estimation with z norm (Appendix D) is shown in figure 7.10(a). Together with the 7975-Hz frame rate,

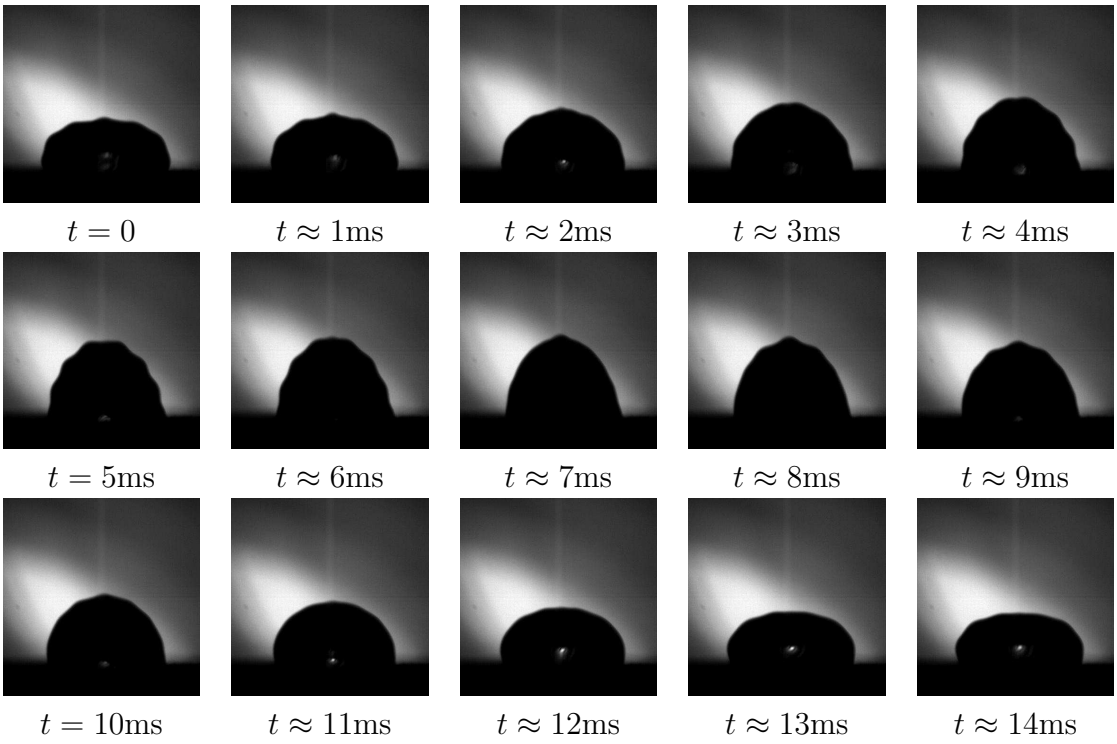

Figure 7.9: Side-view snapshots showing 'crouching' and 'standing' poses of an oscillating superhemispherical sessile drop. Within the 14-ms time period, the drop completes roughly one cycle of 'crouching-standing-crouching', which is the slower shape oscillation of the drop.

the frequency f_s of the slower mode is found to be

$$f_s = 7975 \times 3 \div 350 \approx 68.36Hz \tag{7.3}$$

If one compares the 68.36Hz estimation to the 958-Hz driving frequency, then

$$958 \div 68.36 = 14.014... \approx 14$$

and hence for the first time since the beginning of the project, a 1/14-frequency subharmonic mode is observed in experiments. By comparing image sequences in figure 7.7 and 7.8, one finds that the fast mode roughly completes one period within the first nine snapshots in figure 7.7 and hence the period is approximately 1ms. The slower mode takes all 15 frames in figure 7.8 to complete one cycle and hence its period $\approx$ 14ms. Since the slower mode is a 1/14-frequency subharmonic

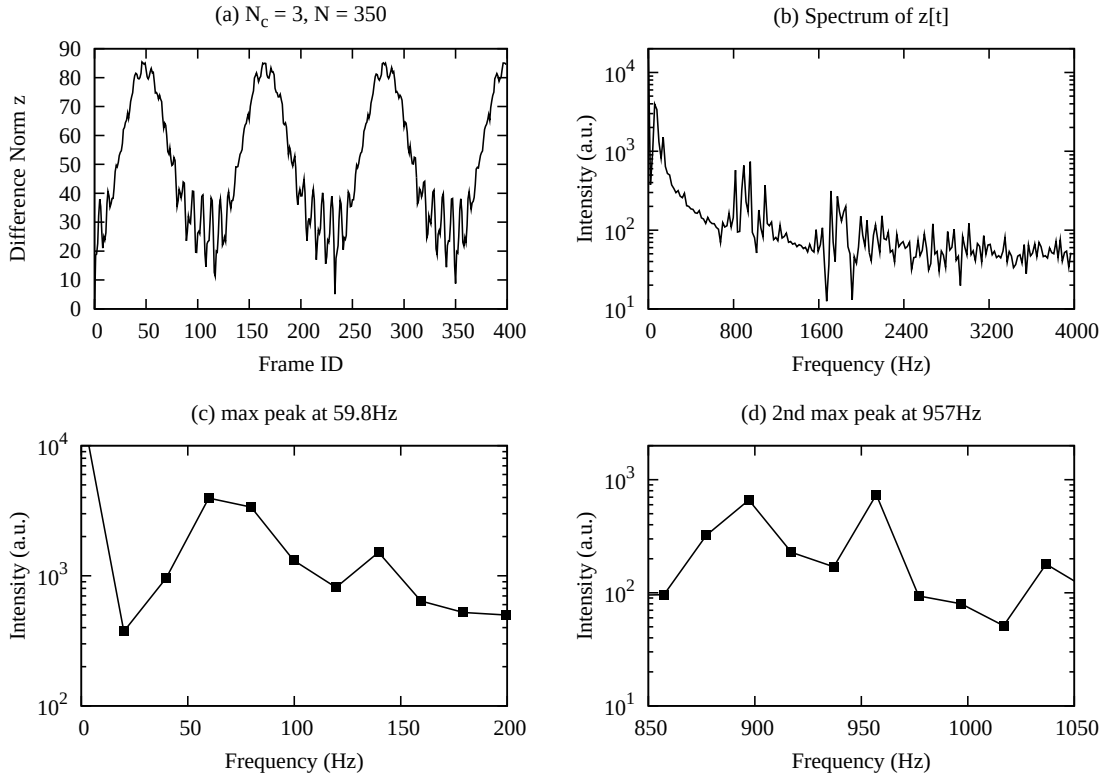

Figure 7.10: Evolution of difference norm and its frequency spectra for the image sequence of figure 7.7 and 7.8.

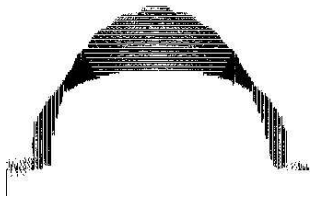

Figure 7.11: Accumulated side-view profile of the oscillating drop showing the drop's crouching-standing motion as a [2, 0] mode.

mode, the faster is expected to be a harmonic mode.

Identification of the faster and slower modes is incomplete without characterizing their shapes. By accumulating the side-view profiles in one single image, the slower mode can be identified. The accumulated side-view profile for 400 snap-

shots is shown in figure 7.11. Only the shape of the slower mode can be identified, since its larger amplitude essentially swamps the fine ripple of the faster mode. Two nodes can be identified from the accumulated side-view profile, and hence the slower mode is identified as a 1/14-frequency subharmonic [2, 0]. Note that without a reference block for motion tracking (cf. Appendix C), substrate motion cannot be backed out. Hence the nodes are not as obvious as one might expect.

For both faster and slower modes, their oscillating frequencies are further tested by frequency analysis. The frequency spectrum of the difference norm in figure 7.10(a) is presented in figure 7.10(b)-(d). The two maxima (not counting the DC signal) are zoomed in and plotted in figure 7.10(c) and (d). The maxima are located at 59.81Hz and 957Hz. By comparing the 59.81Hz peak to the 68.36Hz based on figure 7.10, one finds a deviation of more than 10%. The more credible estimation is chosen based on their uncertainty as follows. For the estimation based on the difference norm $z[t]$, the maximum error ϵ_z can be as large as

$$\epsilon_z = 7975 \times 3 \times \left[\frac{1}{349} - \frac{1}{351}\right] \div 2 \approx 0.195(Hz)$$

which is based on the assumption of miscounting (on average) ± 1 snapshot of the number of frames completing the 3 periods. For the FFT computation, which is based on 400 snapshots recorded at 7975 frames per second, the maximum error ϵ_f is

$$\epsilon_f = \frac{1}{2} \times \Delta f = \frac{1}{2} \times \frac{7975}{400} \approx 10(Hz)$$

where Δf is the spectral resolution of 19.94Hz, and ϵ_f is based on the worst-case scenario where the 'true' frequency equals the average of its two closest sampled frequencies. Since ϵ_z is less than ϵ_f by more than one order, the measurement based on difference norm deserves more credibility. In fact, the credibility can be further confirmed by the number of cycles completed in the 400 snapshots. Visual

inspection of the original 400 frames suggests more than 3 complete periods of the slower, crouching-standing motion. With $f_1 = 68.36$Hz and $f_2 = 59.81$Hz, the number of cycles N_1 and N_2 completed within 400 frames recorded at 7975 frames per second should be

$$N_1 = \frac{400 \times 68.36}{7975} \approx 3.429, \quad N_2 = \frac{400 \times 59.81}{7975} \approx 2.999$$

Visual inspection is qualitative yet intuitive and self-evident, and N_2 clearly contradicts it. Therefore $f_1 = 68.36$Hz is confirmed to be the better estimation of the slower, crouching-standing frequency. However, f_2 should not be interpreted as a wrong estimation. Note that the ± 10 Hz uncertainty of $f_2 = 59.81$Hz technically means $49.81 \leq f_2 \leq 69.81$Hz. If $f_1 = 68.36$Hz is a good estimate, then f_s covers it too. In fact, 59.81Hz is already the closest frequency to the 'target' frequency of $\approx$ 68Hz and hence the optimal estimation with the spectrum. The imprecision results from the unfortunately short (only 400 frames) image sequence, which degrades the resolution of frequency spectrum.

Frequency analysis provides the only quantitative estimation for the faster mode's frequency. Recall that the difference norm provides no relevant frequency estimation, and visual inspection suggests that it is close to the driving frequency. From the spectrum, the second peak is found at 957Hz. Despite the ± 10Hz uncertainty already mentioned, in this case the 957-Hz estimation seems consistent with results based on comparison of figure 7.8 and figure 7.7. It cannot be confirmed by counting the number of periods the faster zonal mode undergoes due to the absence of the faster zonal mode from many snapshots. However, it can be rationalized by considering how a mode can synchronize with the driving signal. Given the range of 957 ± 10Hz and driving frequency at 958Hz, it is hardly imaginable that a wave can synchronize with a forcing by oscillating with an approximately 1% difference in frequency without being a traveling wave. This is obviously not the case in

figure 7.7. Therefore the frequency of the faster mode is expected to be around 957∼958Hz, and hence the mode is harmonic. Note that to acquire a precise frequency estimation, the same experiment must be repeated with a lower sampling frequency (frame rate for high-speed imaging) and a longer data sequence.

In sum, the mixture of a harmonic and a 1/14-frequency subharmonic zonal mode is identified. While the difference norm provides a precise estimation of the slower mode's frequency, the FFT-based method offers the frequency of the faster mode. These estimations complete the preliminary frequency analysis. Prior to entering the next section, note that chronologically, the bi-zonal mode mixing documented in this section is a later observation. The phenomenon is purposely captured after witnessing tri-modal mixing to be introduced in the following section, as the bi-zonal case is a similar yet simpler case for facilitating discussion of the tri-modal.

7.3.4 Lower subharmonic non-zonal mode

An observation similar to section 7.3.3 is presented in this section. Again, a superhemispherical drop simultaneously exhibits two wave patterns with distinct frequencies from the top view. The faster wave is a non-axisymmetric, fine ripple around drop's center. The slower wave is a oblate-prolate shape oscillation of drop's bulk and equator. The two oscillatory motions are illustrated with two different time scales. Unfortunately, no experimental parameter is recorded. The time scale τ used for illustration purposes here is defined as the reciprocal of the (missing) frame rate for high-speed imaging. For the faster wave pattern, snapshots are presented in figure 7.12. The snapshot at $t = 0$ shows a tesseral mode with two azimuthal peaks ($l = 2$) and 5 layers, suggesting that the shape is possibly $[10, 2]$.

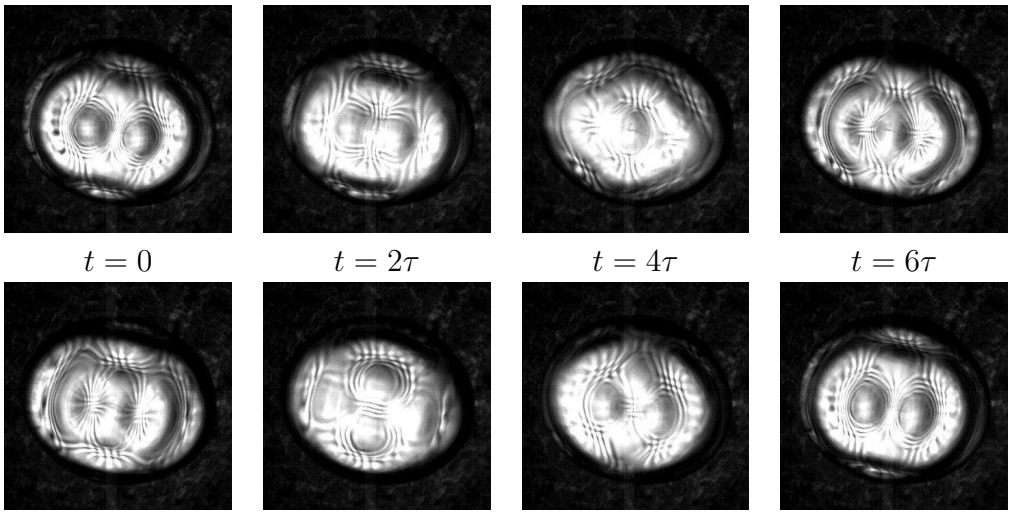

Figure 7.12: Top-view snapshots of an oscillating superhemispherical sessile drop presented at a shorter time scale exhibiting the oscillation of a tesseral mode with $l = 2$. Experimental parameters not recorded.

Because the mode shape conjugate to that at $t = 0$ is absent from figure 7.12, the number of layers truly pertaining to this faster mode is unclear. From these snapshots, however, at least the azimuthal wave number $l = 2$ is identified.

At a longer time scale, the drop exhibits the oblate-prolate shape oscillation. As shown in figure 7.13, the drop starts with an oblate shape at $t = 0$, gradually becomes prolate at $t = 75\tau$, and eventually evolves back to the oblate shape at $t = 177\tau$. Such shape oscillation resembles the sectoral [2, 2] mode. Because of mode mixing, again, it is unclear as to what this slower mode is. To further clarify why the individual shapes cannot be identified, the snapshots at $t = 0$ and $t = 82\tau$ are presented in figure 7.14. At these moments, the shapes of the drop truly conjugate. However, no similar pattern to that in the snapshot of $t = 82\tau$ is observed in any image for $t \leq 14\tau$. Presumably the equatorial shape oscillation influences the faster tesseral mode by interfering the two innermost wave peaks, such that the latter emerge only when its orientation aligns with the former. More

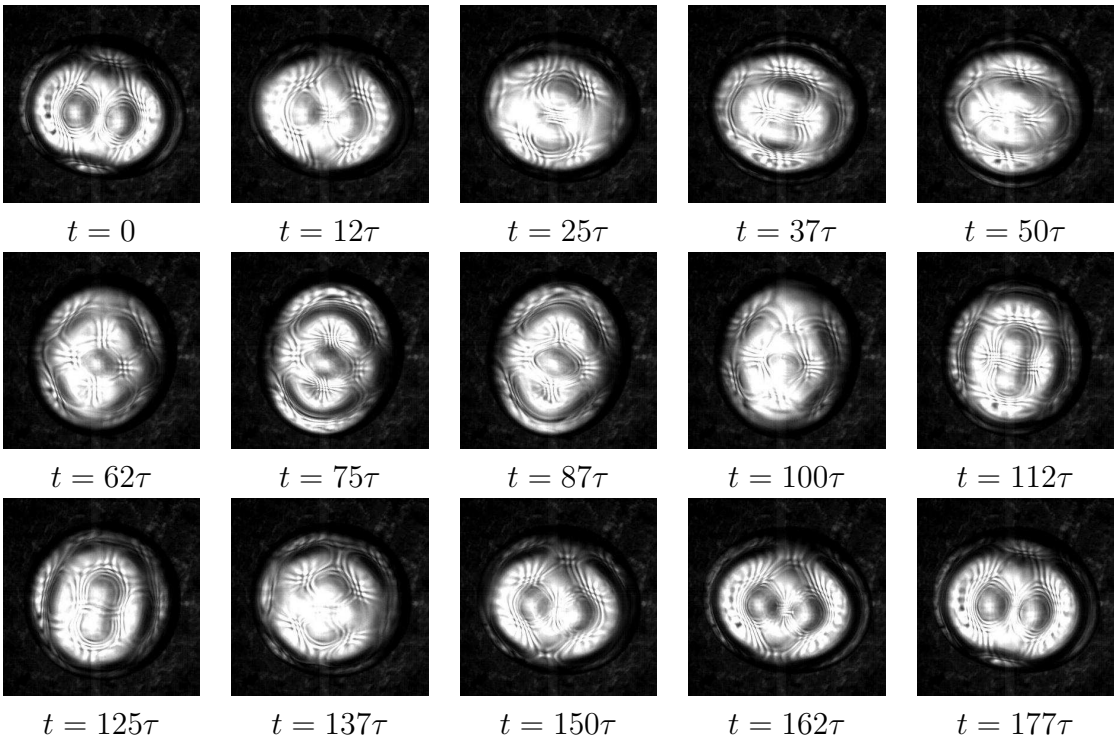

Figure 7.13: Top-view snapshots of an oscillating superhemispherical sessile drop presented at a longer time scale exhibiting the oblate-prolate oscillation.

specifically, the two innermost azimuthal peaks become clearly visible only when they are roughly horizontally (vertically) aligned and the drop is oblate (prolate). Recall that all non-zonal modes with $l \geq 2$ possess a flat region around the top-center portion of the drop, and the more the number of layers, the smaller this flat region. The observation suggests that the slower mode possibly possesses multiple layers so that it is able to effectively interfere the faster mode all the way to the drop's apex.

7.3.5 Tri-modal mixing

In experiments, superhemispherical drops are observed to simultaneously exhibit three visually distinguishable modes. While the drop exhibits mixing of a zonal

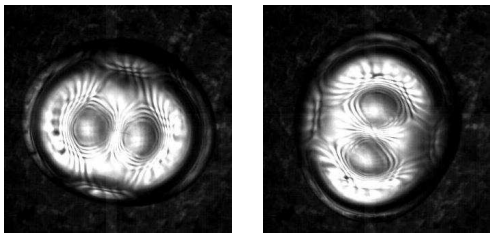

$t = 0$ $t = 82\tau$

Figure 7.14: Two conjugate shapes of an oscillating sessile drop exhibiting the mixture of two $l = 2$ non-axisymmetric modes.

and non-zonal mode similar to that in section 7.3.1, the size of the mode shape also scales periodically at a sensibly lower frequency. Similar to the observation in sections 7.3.3 and 7.3.4, the size scaling causes a slower oscillation of brightness and hence attracts the attention. The phenomenon, which involves three mixing modes, is tentatively designated as tri-modal mixing. The observation is illustrated by re-sampling and presenting with two different time scales. At the shorter time scale, the drop in figure 7.15 exhibits a 2-layer triangular pattern. The pattern clearly indicates [5, 3] as one of the mixing modes. At the drop's center, the alternating convex-concave deformation implies the presence of a zonal mode. The latter oscillates at a higher frequency, since the former and the latter respectively complete one period around $t = 6.6$ms and $t = 3.0$ms in figure 7.15. Based on these rough estimations, the faster zonal mode oscillates with $f_z \approx 1 \div 0.003 \approx 333.3$Hz. Therefore the faster zonal mode is harmonic, while the [5, 3] is half-frequency subharmonic.

In addition to a zonal and a [5, 3] mode, a low-frequency, high-amplitude mode participates the mixing in figure 7.16. The inner triangular pattern shrinks as the shape evolves, and the drop shows a larger and brighter triangle than at $t = 6.6$ms. Such size variation is more clearly illustrated in figure 7.16. Starting from $t = 0$, the size gradually diminishes and minimizes at $t = 10.4$ms. Afterwards

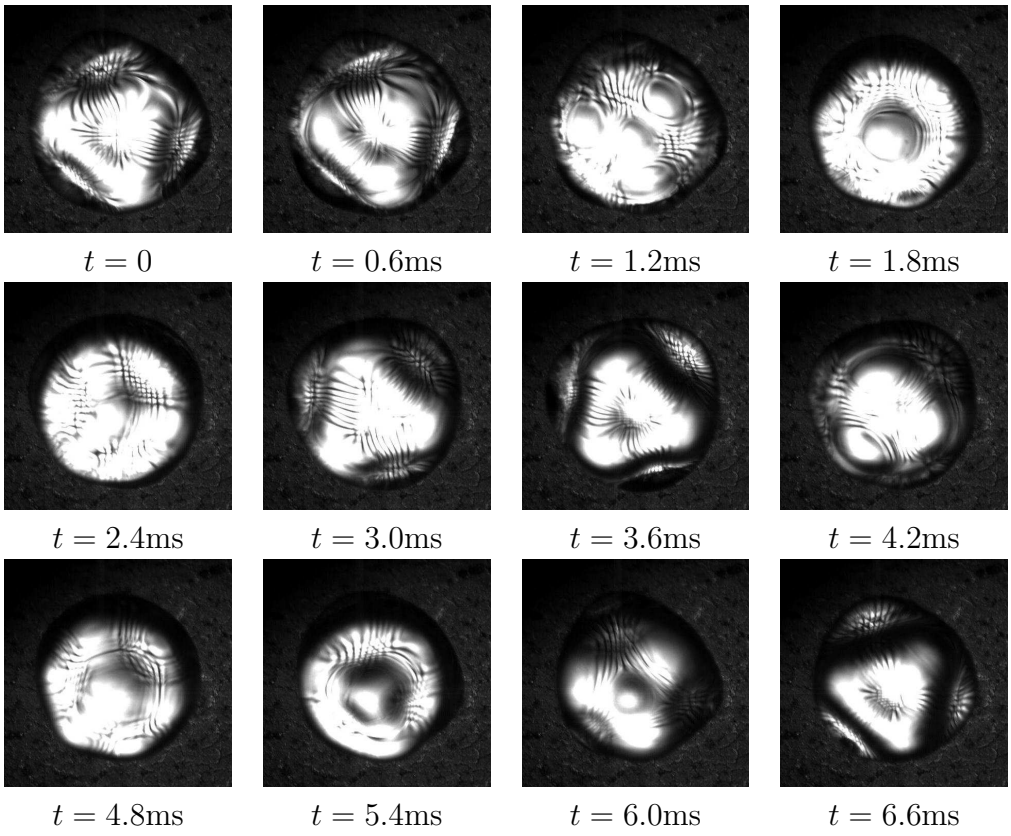

Figure 7.15: Top-view snapshots of an oscillating superhemispherical sessile drop presented at time scale $\Delta t \approx 0.6$ms exhibit a [5, 3] mode and an unidentified zonal mode. Drop volume: 24μL. Forcing: 335Hz, 10g. Frame rate: 5000fps.

the size increases. At $t = 24.4$ms, the pattern returns to approximately the same size as $t = 0$. From figure 7.16, the 'crouching-standing' mode oscillates at $f \approx 1 \div 0.0244 \approx 40.98$Hz, while the [5, 3] mode at $f_{[5,3]} \approx 1 \div 0.0066 \approx 151.52$Hz.

Side-view snapshots in figure 7.17 suggest that the periodic scaling of the mode shape results from the 'crouching-standing' motion of the drop. The drop is tallest at $t = 6.8$ms and shortest at $t = 15.3$ and 18.7ms. Since the scaling is isotropic, the lowest-frequency mode is speculated to be zonal. Frequency estimation from top-view snapshots suggests that the slowest frequency in the image sequence $f_{\min}$ in figure 7.18 is

$$f_{\min} = 5000 \times 1 \div 120 = 41.67Hz \tag{7.4}$$

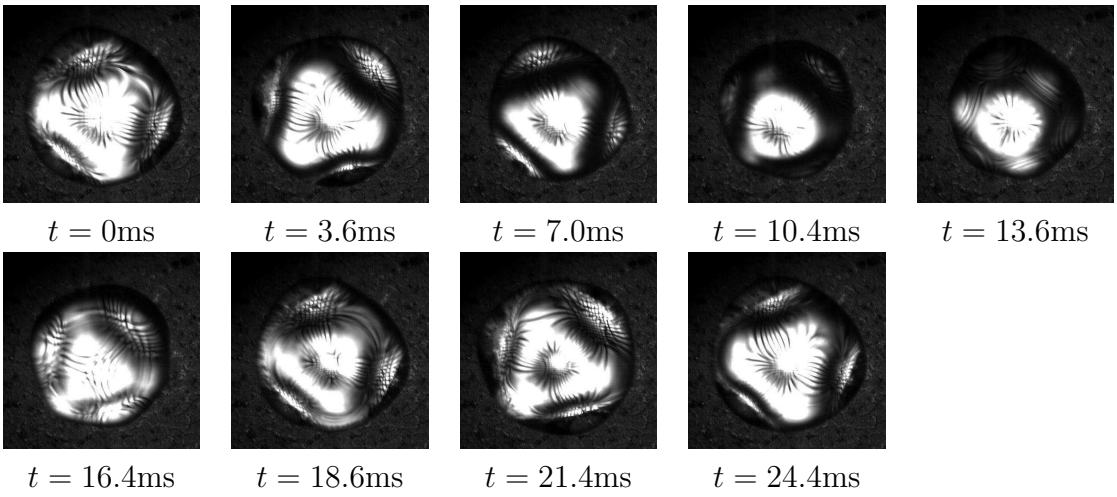

Figure 7.16: Top-view snapshots of an oscillating superhemispherical sessile drop presented at time scale $\Delta t \approx 3.5$ms exhibit a periodic shape scaling of the [5, 3] mode.

which, if compared to the driving frequency $f_d = 335$Hz, yields

$$\frac{335}{41.67} = 8.04... \approx 8 \tag{7.5}$$

Therefore lowest-frequency oscillation is 1/8-frequency subharmonic. Although the side-view profile provides little information about the mode shape, the mode is speculated to be [2, 0] because of its low frequency and large deflection.

Frequency analysis of the difference norm z provides a crude estimation for the frequencies of all modes. The estimation is crude since it is only based on 200 snapshots acquired at 5000 frames per second. The corresponding spectral resolution is $5000 \div 200 = 25$ Hz. The spectrum is shown in figure 7.18(b). The maximum peaks locate at 50, 175 and 350Hz. The 50-Hz peak possibly pertains to the crouching-standing motion. The 175-Hz peak may indicate the [5, 3] mode as a half-frequency subharmonic mode since $335 \div 175 = 1.91... \approx 2$. Finally, the 350-Hz peak possibly suggests the faster zonal mode as a harmonic mode, because $335 \div 350 = 0.957... \approx 1$. A more precise frequency estimation requires a longer image sequence and perhaps also a lower frame rate. In addition, the faster

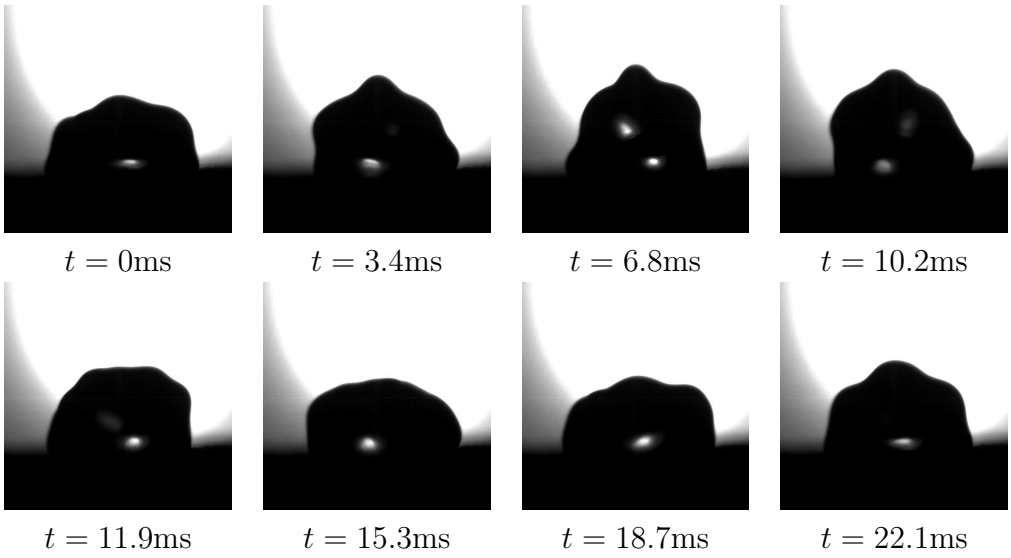

Figure 7.17: Side-view snapshots of an oscillating superhemispherical sessile drop presented at time scale $\Delta t \approx 3.4$ms exhibiting a periodic 'crouching-standing' oscillation.

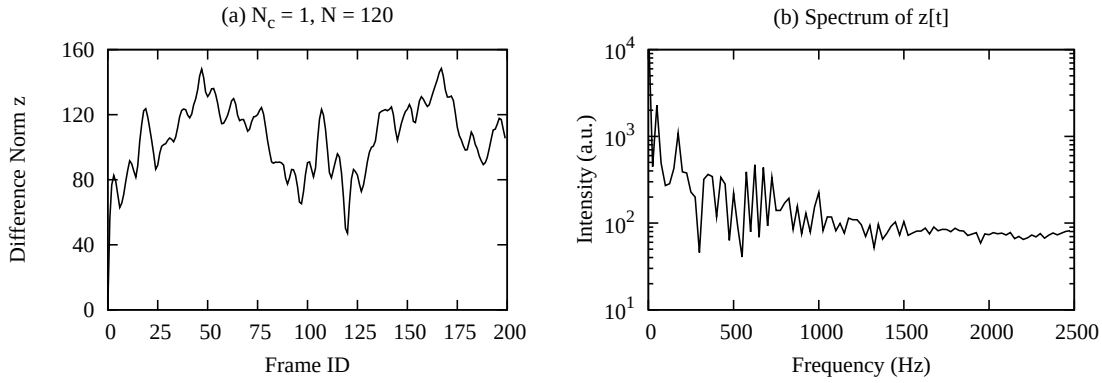

Figure 7.18: Evolution of difference norm and its frequency spectrum for the image sequence of figure 7.15∼ 7.16. Peaks in the spectrum are located at (1) max: 50Hz, (2) second max: 175Hz and (3) third max: 350Hz.

zonal mode can be separately investigated by applying sufficiently small forcing acceleration.

Tri-modal mixing is commonly encountered in experiments with superhemispherical drops. Another example of the mixture of a [7, 5], a faster zonal and a 'crouching-standing' mode is presented with two time scales in figure 7.19 and

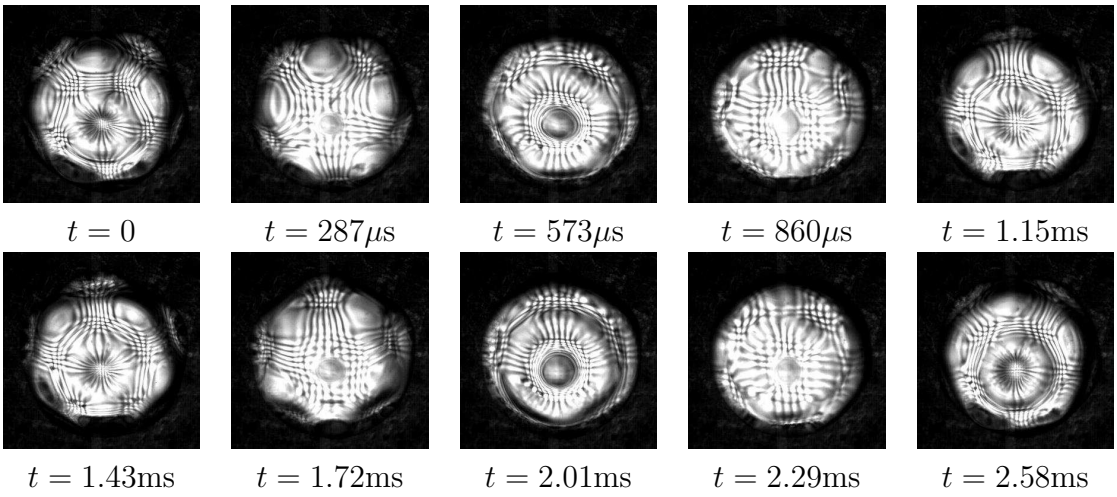

Figure 7.19: Top-view snapshots of an oscillating superhemispherical sessile drop presented at time scale $\Delta t \approx 293\mu$s exhibiting a periodic shape scaling of the [7, 5] mode. Drop volume: 18μL. Forcing: 693Hz, 20g. Frame rate: 10470fps.

7.20. According to figure 7.19, the drop exhibits two layers of pentagons mixed with a zonal mode of fine axisymmetric ripples. While the [7, 5] completes one period within 2.58ms, the zonal mode finishes approximately two cycles within the same duration. The size scaling of the mode is hardly noticeable, since figure 7.19 adopts the faster time scale.

To demonstrate the 'crouching-standing' motion, the same top-view snapshots are presented with a longer' time scale in figure 7.20. Here the slower mode completes one period in approximately 19.20ms, which is much longer than the periods of other two modes. Note that figure 7.19 and 7.20 are presented only to qualitatively demonstrate this example. No quantitative result of frequency estimation is provided due to inconsistency between the documented forcing frequency and imaging frame rate. Without more information about the data set, all relevant results need repeated in future exploration.

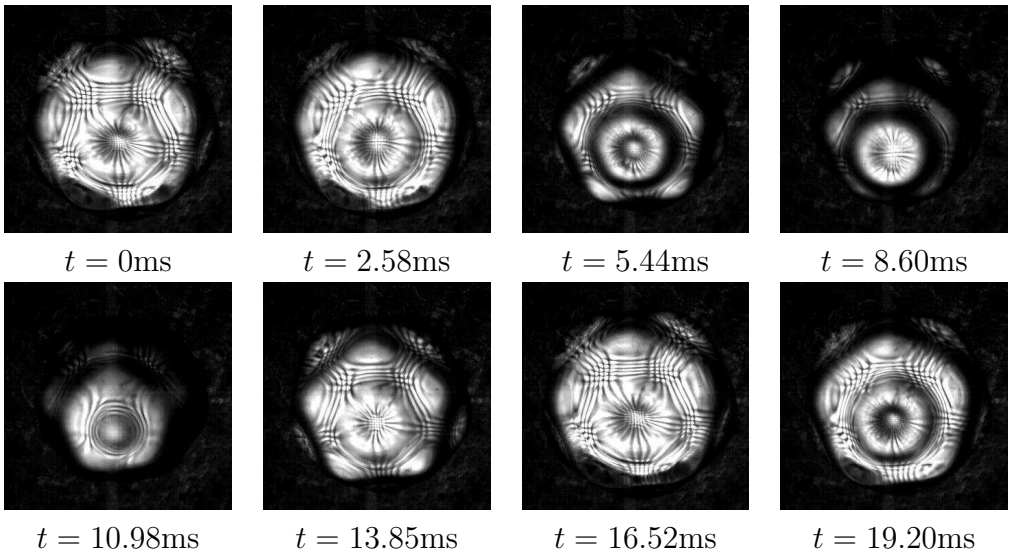

Figure 7.20: Top-view snapshots of an oscillating superhemispherical sessile drop presented at time scale $\Delta t \approx 2.75$ms exhibiting a periodic size scaling of the [7, 5] mode.

7.3.6 Further exploration

The preliminary results reveal a rich collection of dynamics for future exploration. Investigating these phenomena may or may not directly benefit any engineering application. From the scientific perspective, however, it is interesting to categorize all families of harmonic modes and further characterize forced resonance of superhemispherical drops. Different aspects for future exploration include the pursuit of all families of subharmonic modes, a more precise measurement of their resonance frequencies, and a formal characterization of the amplitude responses.

APPENDIX A

MECHANICAL PLATFORM I: DESIGN OF OMNIVIEW PLATFORM

To optimize observability of resonating sessile drops, a simple and economic mechanical platform is implemented. Designated as `OmniView`, the platform allows retrieval of images for resonating drops from any directions with one single quasi-stationary high-speed camera. Currently the platform is installed to provide top, left and right views. Effectiveness of the platform is demonstrated with various example images.

In experiments, image acquisition starts by observing the surface pattern of an oscillating drop from the top. Drops are deposited on a substrate and vibrated by a mechanical vibrator (VTS-100, by Vibration Test Systems, Aurora, Ohio). Top views of drops' mode shapes are visualized by the underlying grid pattern (woven metal mesh, 85385T875, by McMaster-Carr, Aurora, Oh). Deformation of a drop's free surface results in refraction of light rays passing through it, which in turn results in visually deformed mesh pattern. Once any target pattern is observed, an image sequence is recorded using a high-speed camera (RedLake HG-XL, by DEL Imaging Systems, LLC., Cheshire, CT). Side views are acquired by imaging from one side and projecting light from the other. Therefore *OmniView* integrates the camera, light sources and the mechanical vibrator. Design constraints of `OmniView` are

a. only one high-speed camera is available in experiments

b. the camera's resolution is insufficient for splitting into sections and recording different views simultaneously

c. the camera weighs 15lb/6.5kg and must be installed horizontally

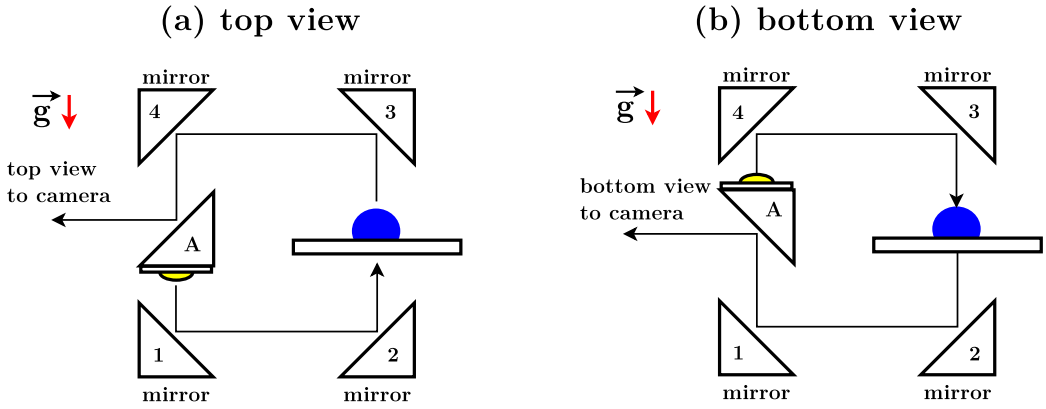

Figure A.1: OmniView platform: observing top and bottom views of drops (blue) with light source (yellow)

Accordingly, a model of `OmniView` is conceived as shown in figure A.3. In figure A.1(a), light is emitted from an LED device under mirror A, reflected by mirrors 1 and 2, passing through the drop, reflected by mirrors 3, 4 and A, and eventually transmitted into the camera. By re-orienting mirror A as shown in figure A.1(b), bottom view of the drop can be obtained in a similar way. Ideally, with the setup in figure A.1, different views of a drop are acquired by rotating mirror A and no re-positioning and not even any re-focusing of the camera is needed. Moreover, by rotating the structure 90° along its center axis, side views are readily available, as shown in Fig A.2. Notice that Fig A.2 is the top view of `OmniView`, whereas figure A.1(a) and (b) are its side views.

Among all mirrors in Fig A.1∼ A.2, mirrors 2, 3, 6 and 7 must stay fixed in space because otherwise complicated dismounting and re-installation is required, as below the drop the solid substrate is surrounded by the plastic legs holding the solid substrate. However, since `OmniView` provides only one view at any time, only one among mirrors 1, 4, 5 and 8 is needed. Therefore the platform depicted in figure A.1 can be reduced as shown in figure A.3.

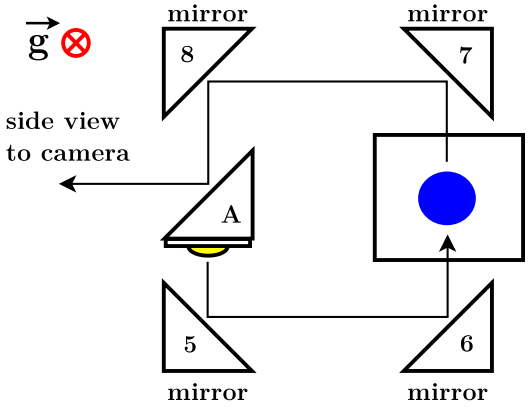

Figure A.2: OmniView platform: observing side (left) view of drops (blue) with light source (yellow)

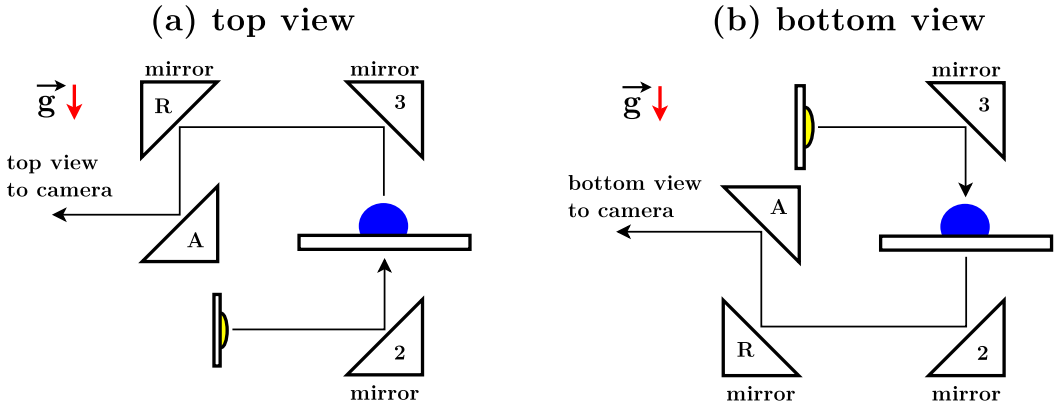

Figure A.3: `OmniView` platform: reduced structure for observing drop (blue) using light (yellow)

Whereas the original structure in figure A.1 and figure A.2 requires 9 mirrors, that in figure A.3 needs only 6. mirrors 2, 3, 6 and 7 remain fixed at any time, while mirrors A and R are mobile mirrors to be aligned and rotated together with the LED lighting device. Notice that during numerous preliminary tests, little contact line motion of a drop is observable. In these cases only the top and side views need to be captured so that the bottom static mirror (mirror 2) can be removed and replaced by a static LED device for improving lighting for the top view.

A.1 Design of Mechanical Parts

According to figure A.3, `OmniView` consists of two parts:

a. static mirror set, the four mirrors reflecting top (3), bottom (2), left (7) and right (6) views of a drop

b. mobile mirror set, two mirrors (A & R) and a LED device directing and illuminating droplet image into camera

During experiments, **a.** is fixed in the space once aligned, while **b.** is rotated to switch from one view to another. To provide sufficient flexbility of positioning and aligning mirrors on each frame, structures with two translational degrees of freedom are adopted. A schematic of the basic component for **a.** is shown in figure A.4, where a mirror is installed on a straight guiding rod attached to a corner block.

In figure A.4, the mirror is free to slide on the horizontal straight guiding rod, which is fixed onto the corner block. The vertical rod guides the vertical motion of the corner block and hence the mirror. Therefore the mirror can be moved horizontally by sliding on the horizontal rod and vertically by moving the corner block. A 90° rotationally symmetric frame consisting of four identical corner blocks, to each a guiding rod is attached, is adopted for the structure of the static mirror set, as shown in figure A.5(a). Together with the installation of mirrors shown in figure A.4, complete assembly of the static mirror set is shown in figure A.5(b).

Notice that the mirror and guiding block in figure A.4 are mirror 2 and block Y in figure A.5(b), where motions allowed for each mirror are tabulated in table. A.1.

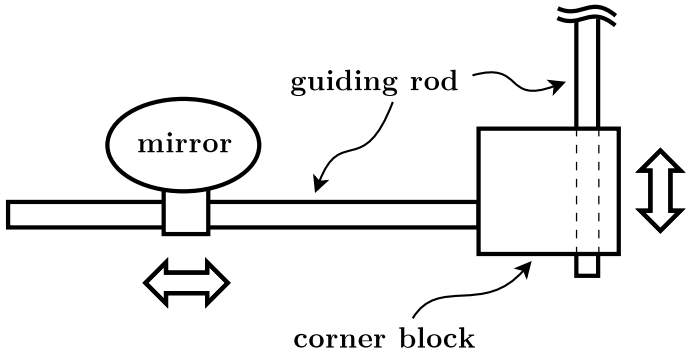

Figure A.4: Basic component of static mirror set

Mirror	Horizontal Motion	Vertical Motion
2	slide on guiding rod	slide corner block Y
3	slide on guiding rod	fixed to main frame
6	slide corner block Z	slide on guiding rod
7	fixed to main frame	slide on guiding rod

Table A.1: Allowed motions of static mirrors

Three-dimensional drawings of the static mirror set is shown in figure A.5.(a) and (b). The mechanical drawing is constructed using `SolidWorks 2011`.

The mobile mirror set is designed with the same structure as the static set. The set consists of a center mirror A fixed to a shaft, a rotary mirror R, reflecting image from one of the static mirrors to mirror A, and a LED lighting device illuminating drops. To avoid mechanical interference of solid parts, LED lighting device and the two mirrors in the mobile mirror set must be placed on different sides of the shaft. Distance of the mirror R and LED lighting device from the center axis of the shaft can be adjusted by sliding blocks `a.` and `b.` on the guiding rods, respectively. To help direct the LED's light, a metal cup is designed and placed in front of the device. Schematic of complete assembly of mobile mirror set is depicted in figure A.6:

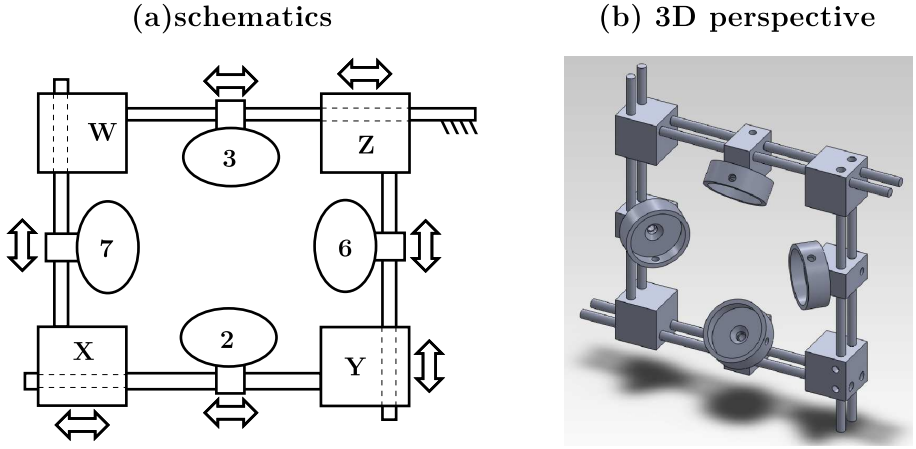

Figure A.5: Static mirror sets

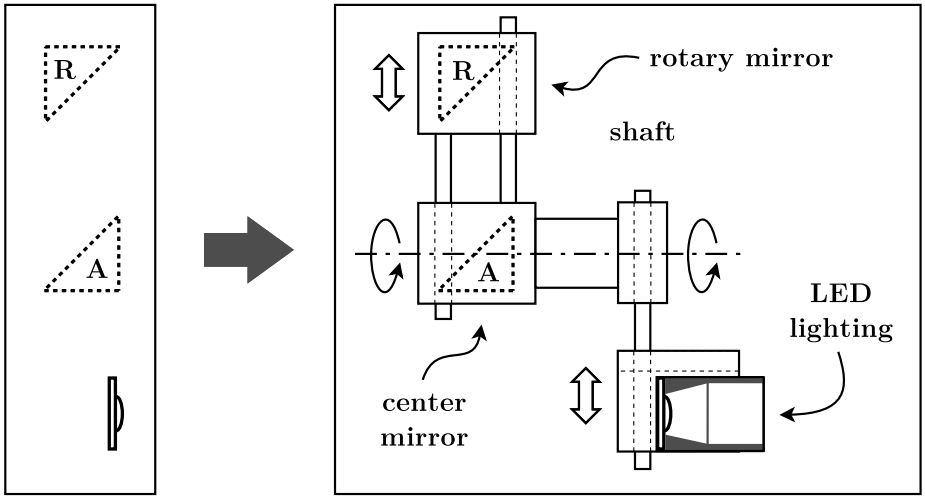

Figure A.6: Schematic of complete assembly of mobile mirror set

To illustrate the mobile mirror set, a drawing of front, side and back views and a 3D perspective are shown in figure A.7:

A 3D drawing and a picture of the `OmniView` set up for observing top view of oscillating drops are shown in figure A.8. In figure A.8(b), multiple motion stages and stainless steel rods are utilized for stablizing `OmniView`, as during experiments, the platform must withstand the vibration and remain stationary. Installation of the rods essentially constrains the vibration of the platform in any direction.

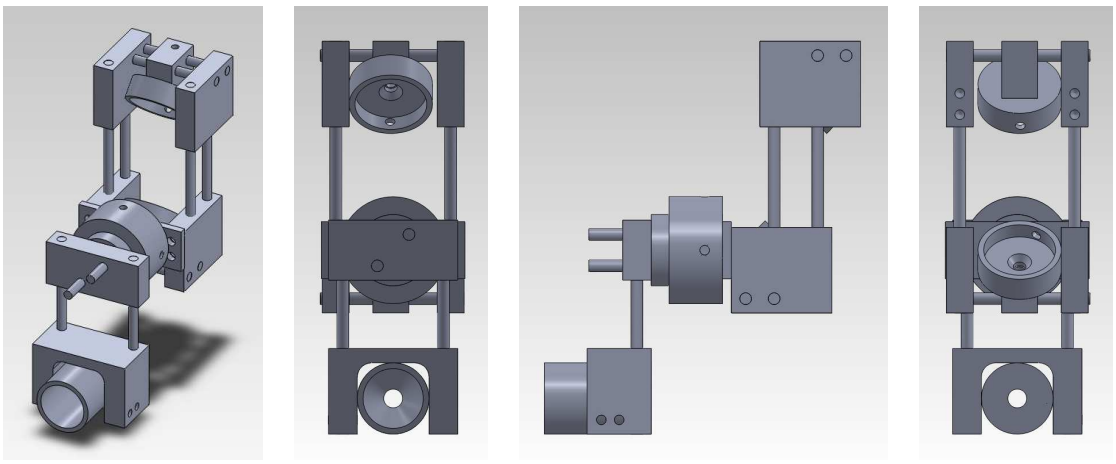

(a) 3D perspective (b) front view (c) side view (d) back view

Figure A.7: 3D drawings for mobile mirror sets

During the testing period, it is found that both static and mobile mirror sets need be mounted from both left and right. Otherwise, with these frames installed from only one side, frames vibrate together with the shaker. Consequently the acquired image sequence exhibits lateral vibration even when the shaker is oscillating only vertically. Notice that while effectively securing the platform, these stabilizing structure also prohibit the any adjustment of the platform. Therefore the platform must be adequately positioned and aligned to provide the optimal image quality and ease of operation beforehand.

A.2 Standard Operating Procedures & Preliminary Results

During the testing period, a standard operating procedure is implemented for `OmniView`. All experiments start with capturing side-view images of a static drop. For different extents of contact line motion, two different procedures are adopted:

(a) 3D perspective **(b) assembled platform**

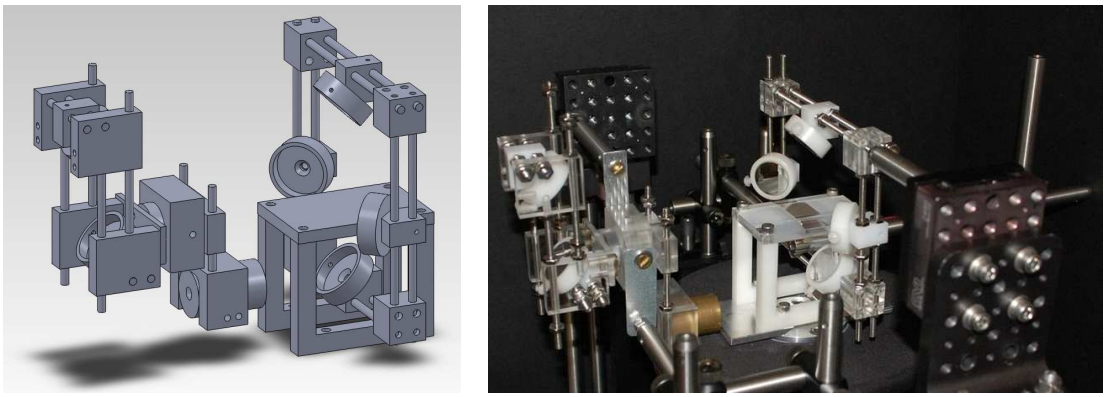

Figure A.8: Assembled `OmniView` observation platform

A. little contact-line motion: capture top, left and right views of an oscillating drop

B. significant contact-line motion: capture top, bottom, left and right views of an oscillating drop

The experiment ends after capturing another side view image of static drops. The static side views before and after oscillation provide the maximum and minimum contact angles, respectively. By default, **A.** is adopted to observe any mode. Procedure **B.** is executed only if any significant contact line motion for a particular mode is observed.

In experiments, it is empirically found that a reasonable temporal resolution of image sequence is achieved if at least ten frames of images are recorded within one cycle of a zonal modes oscillation. For non-zonal modes which lack axisymmetry, ten frames of images are needed for each half cycle of oscillation. Considering that zonal and non-zonal modes are harmonic and half-frequency subharmonic modes, respectively, frame rates (frames per second) for high-speed imaging are chosen to be at least ten times the driving frequency of the mechanical vibrator. Rather than

Frame rate (fps)	5000	6270	7975	9100	10470
Resolution (pixel^2)	512^2	480^2	416^2	384^2	352^2

Table A.2: Optimal frame rate and the corresponding maximal spatial resolution

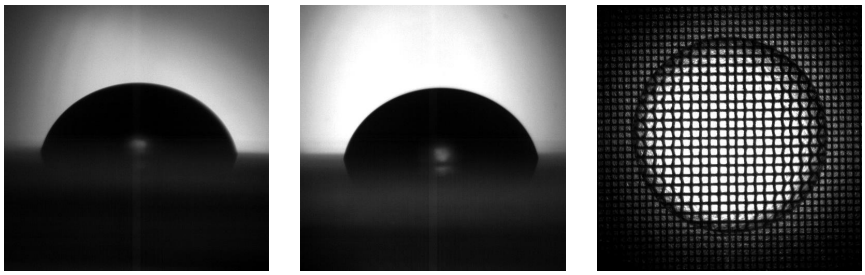

(a) left view (b) right view (c) top view

Figure A.9: Images of a 20μL static drop

simply recording images at ten times the driving frequency of mechanical oscillation, the frame rates are chosen among the set of optimal frequencies dictated by the HG-XL high-speed camera utilized in experiments. For this camera, the frame rates are partitioned and associated with a particular optimal spatial resolution as shown in table. A.2.

Preliminary results of executing procedure **A.** is shown in the following. First of all, static side and top views of a drop are captured, as shown in figure A.9. These images provide information for (1) measuring contact angle and (2) estimating droplet volume. After the static images are recorded, oscillation is started. Top view images are captured first, from which the mode shape of a drop is identified. An example image sequence is shown in figure A.10, where the polar and azimuthal wave numbers (k, l) of the mode are (5, 5). The mode features a pattern with 5 azimuthal peaks distributed in one horizontal layer. The peaks are identified from both the contour of the halo and the inhomogeneously magnified mesh pattern. The image sequence is captured with a static LED device placed right below the mesh pattern under the drop. Background of the drop is a stainless steel wire mesh

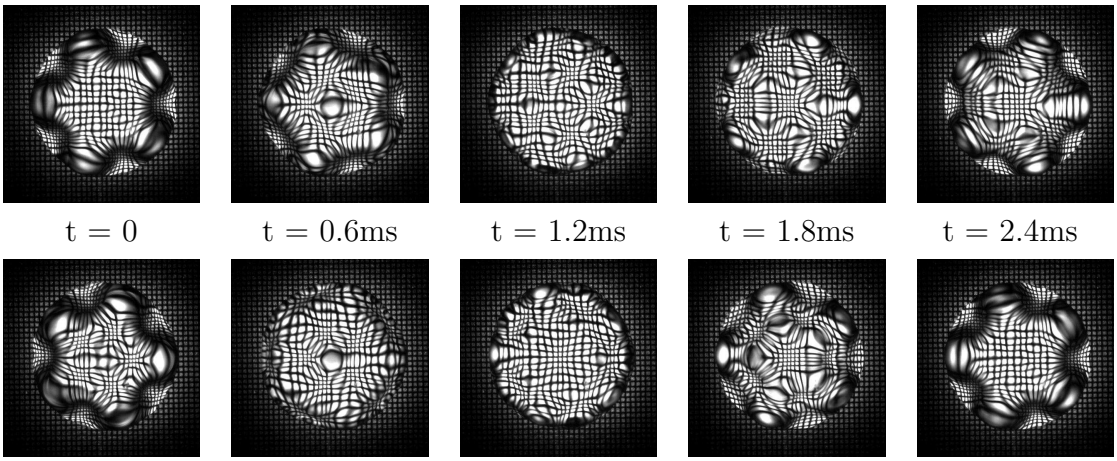

Figure A.10: Top view images of a (5, 5) mode over one period of oscillatory response.

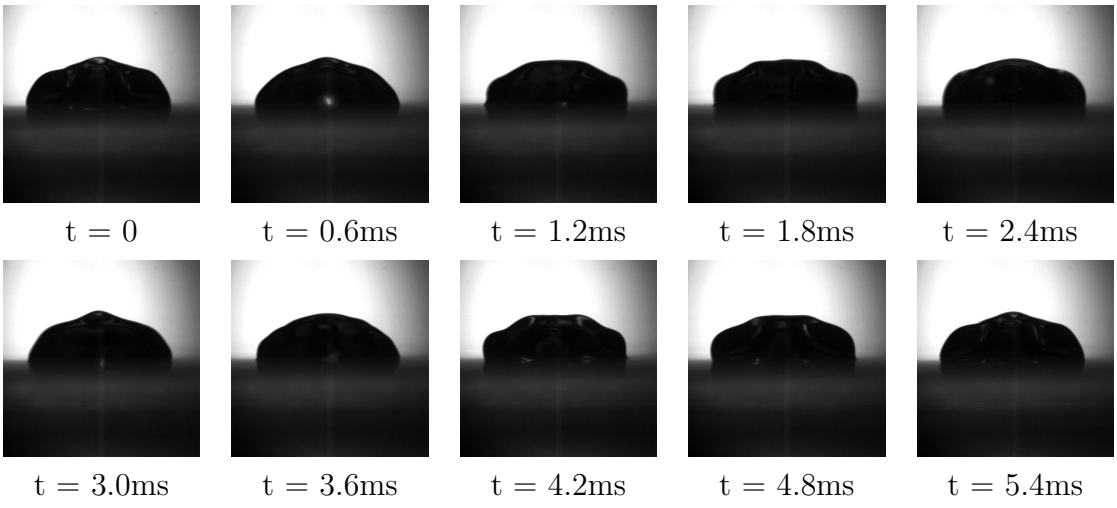

Figure A.11: Right view images of a (5, 5) mode over one period of oscillatory response.

with a 66μm line width and 103.3μm line spacing.

Subsequently, side views of an oscillating drop are captured. First, the right view, as shown in figure A.11. Lighting for side view images are provided by the LED attached to the mobile mirror set. From figure A.10, apparently the azimuthal wave completes one cycle while the polar (figure A.11) undergoes two periods within the same 5.4ms period.

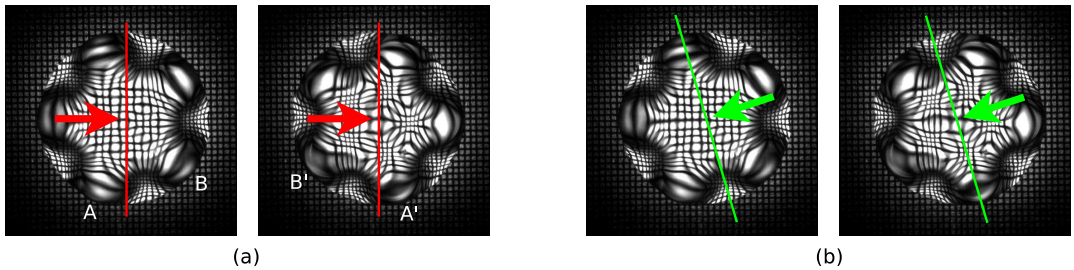

Figure A.12: Schemes of projecting oscillating drops' polar wave pattern

In fact, no frequency doubling is occurring. This illusion is an artifect of image projection. If the polar pattern is projected onto planes normal to the arrow shown in figure A.12(a), apparently the same projection appears within one cycle since the projections of peaks A and B are the same as those of A' and B', respectively. However, if projected as shown in figure A.12(b), no such overlapping as that in figure A.12(a) exists, therefore polar wave pattern then exhibits the same frequency as the azimuthal.

Another sequence of side view images is captured from the left, as shown in figure A.13. While images in figure A.11 are projected more like those as figure A.12(a), for figure A.13 the projection is more like figure A.12(b), as the latter shows less mirror symmetry at any time. Ideally both of the side views should yield the same images. The difference between figure A.11 and figure A.13 is due to the slight misalignment of the mirrors, as the cold-rolled threaded rods employed in `OmniView` are not perfectly straight. However, such misalignment is not considered a disadvantage, as this feature facilitates retrieval of more geometric information by offering views from slightly different angles. From either the top, left or right view, contact line motion is insignificant. Therefore the same test is not repeated for retrieving the bottom view.

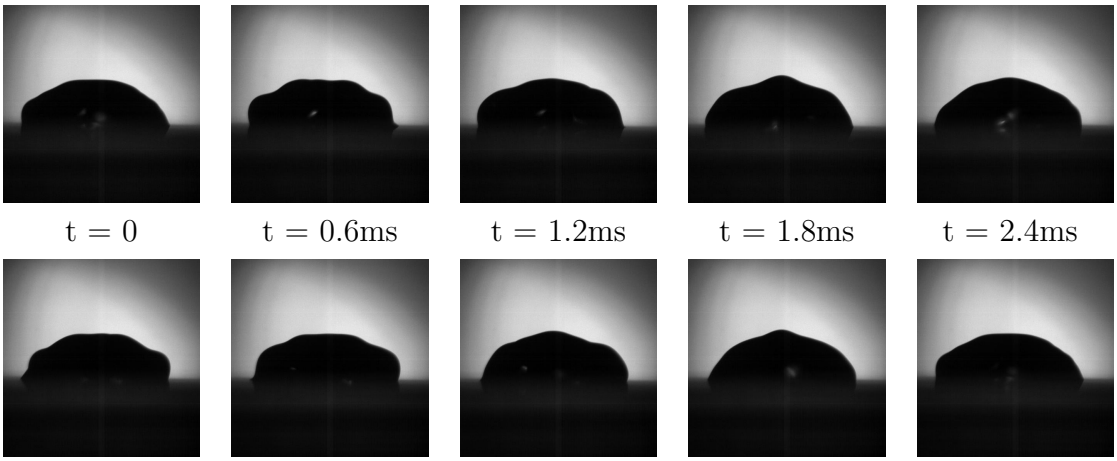

Figure A.13: Left view images of a (5, 5) mode over one period of oscillatory response.

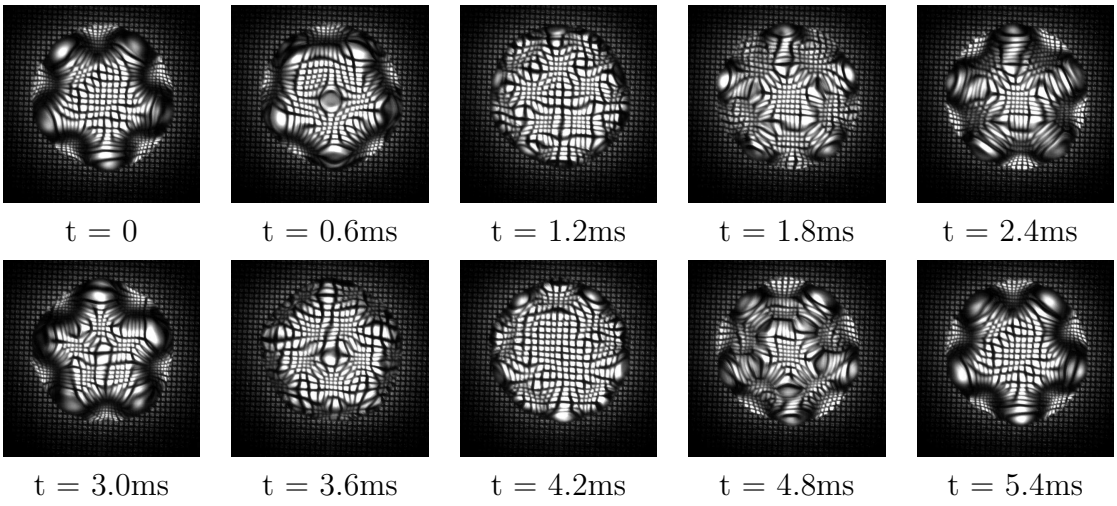

Figure A.14: Confirmatory top view images of a (5, 5) mode over one period of oscillatory response.

Because of evaporation, a drop losses volume during an experiment, which can result in the disappearance of a mode shape. To ensure the same mode persists, and hence that the side views are indeed those of the same mode as that in the first top view image sequence, a confirmatory sequence of top view images is captured, as shown in figure A.14.

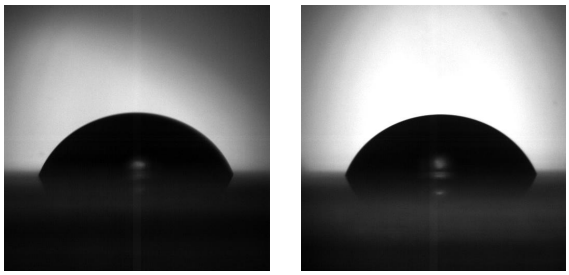

(a) left view (b) right view

Figure A.15: Images of the 20μL static drop after oscillation

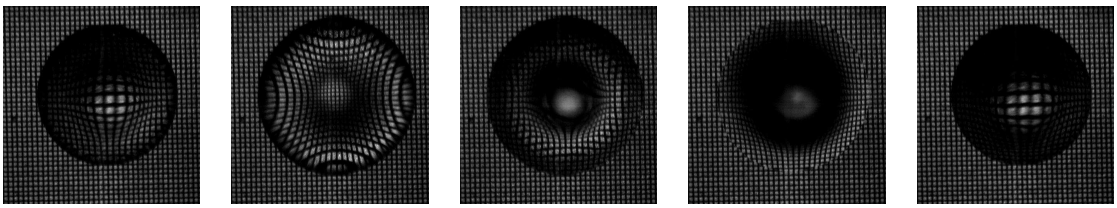

t = 0 t = 4.2ms t = 8.4ms t = 12.6ms t = 16.8ms

Figure A.16: Top view images of a (2, 0) mode.

According to figure A.14, the same mode shape persists. Time duration of a typical experiment is 6 to 8 minutes. Depending on each particular mode, some persist and others decay. Finally, static side views of the drop are captured again, as shown in figure A.15. Significant evaporation is expected to occur for the drop, as the decrease in its contact angle is obvious. By comparing figure A.10 and figure A.14, apparently the mode is unaffected by such extent of evaporation.

For procedure **B.**, image sequences are shown in figure A.16∼24. These images are captured for a low-frequency mode resonating at 58Hz. Because of its significant contact line motion, acquisition of bottom view is necessary. First of all, the mode shape is identified from its top view, as shown in figure A.16:

Notice that to capture the bottom view, the static LED device right under the drop is removed since the physical space is occupied by a static bottom mirror. Therefore the lighting in figure A.16 is lower than that in figure A.14 or figure A.10.

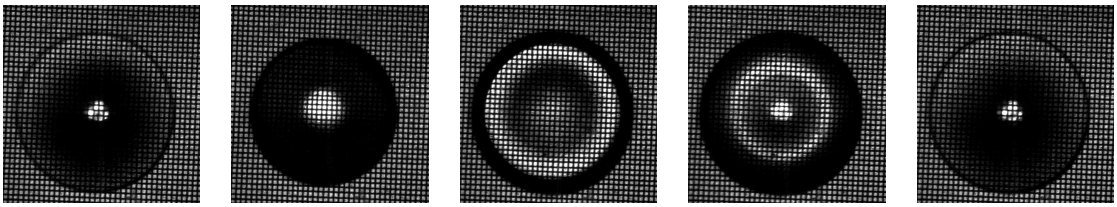

t = 0 t = 4.2ms t = 8.4ms t = 12.6ms t = 16.8ms

Figure A.17: Bottom view images of a (2, 0) mode.

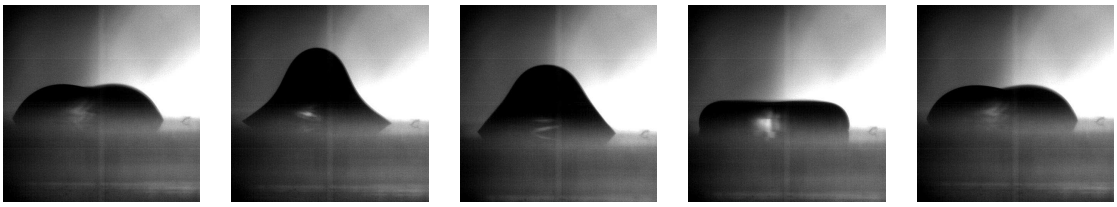

t = 0 t = 4.2ms t = 8.4ms t = 12.6ms t = 16.8ms

Figure A.18: Left view images of a (2, 0) mode.

For figure A.16, however, since the mode shape is simply axisymmetric, even without intense lighting the mode shape is recognizable. As an example of detectable contact line motion, figure A.17 shows the bottom view of the same resonating drop with each drop shown in an identical field of view:

In the bottom view, the halo around the drop's edge clearly indicates the contact line. Typically, such detectable contact line motion occurs only for modes corresponding to frequencies lower than 100Hz. Finally, the side view images are presented in figure A.18 and figure A.19. These images further confirm the drop's axisymmetry to good approximation.

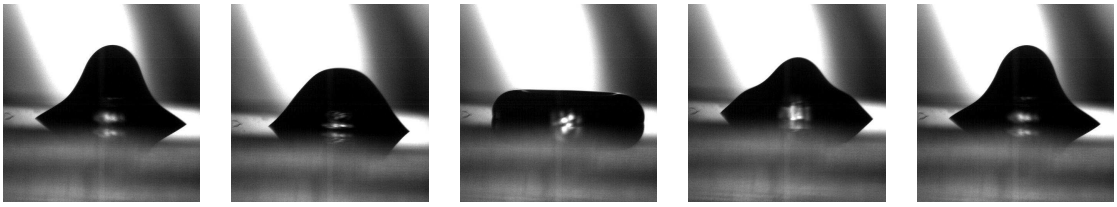

t = 0 t = 4.2ms t = 8.4ms t = 12.6ms t = 16.8ms

Figure A.19: Right view images of a (2, 0) mode.

A.3 Summary

To enhance observability in experiments, the `OmniView` observation platform is fully implemented and tested. Standard operating procedures for experiments with different contact line motions are implemented. Results presented in this document demonstrate the designed functionalities of the platform, with which experiments are currently in progress.

APPENDIX B

MECHANICAL PLATFORM II: ACCELERATION MEASUREMENT

All mechanical forcing amplitudes are measured in terms of accelerations. The measurement system consists of an accelerometer (model #8704B100, by Kistler, Amherst, NY), a proprietary signal cable (model #1761B3 by Kistler, Amherst, NY), a signal conditioner (model #5114, by Kistler, Amherst, NY) and a digital oscilloscope (model GDS-1102-U, by GW-Instek, Taipei, Taiwan) as depicted in Fig. B.1. To measure forcing acceleration of mechanical vibrator, the accelerometers is directly mounted onto the `OmniView` platform and then connected to the signal conditioner and oscilloscope. To ensure accuracy of measurement, accelerometers are installed according to their rated torque using a torque wrench. The oscilloscope saves measured digital signal to a USB flash drive.

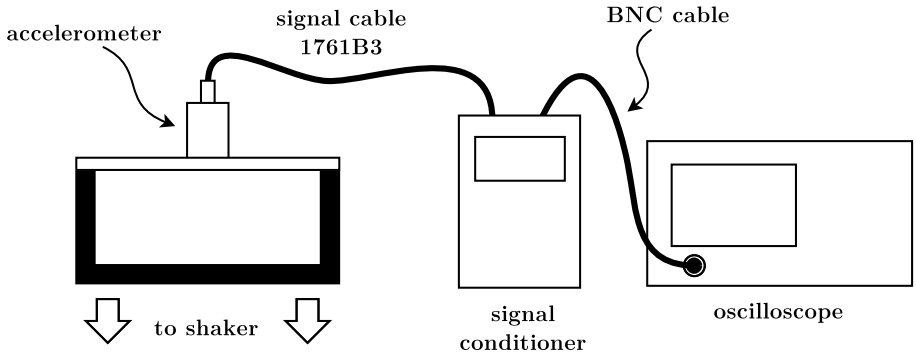

Figure B.1: Hardware setup for measuring mechanical acceleration

APPENDIX C

IMAGE ANALYSIS I: MOTION TRACKING

For experiments with vibrated sessile drops when substrate motion needs analyzed from the side view, a method based on cross-correlation is adopted. Given functions $f(x)$ and $g(x) = f(x - d)$ defined for $a \leq x \leq b$ (figure C.1(a)), the method estimates the displacement d by finding the $y = d$ that maximizes the cross-correlation function $H(y)$:

$$H(y) = \int_{x=a}^{b} f(x + y)g(x)dx \tag{C.1}$$

The cross-correlation in Eq. C.1 is computed with forward and inverse Fourier transforms specified in Eq. C.2.

$$H(y) = \mathcal{F}^{-1}\Big\{\mathcal{F}(f) \times \mathcal{F}^{*}(g)\Big\} \tag{C.2}$$

where the superscript $*$ means complex conjugate. Because Fourier transform implicitly assumes periodicity of $f(x)$ and $g(x)$, if $H(y)$ maximizes at $y = Y$, it actually means either $d = Y$ or $d = (b - a) - Y$. Therefore the values of $V_1 = f(x) \times g(x - Y)$ and $V_2 = f(x) \times g(x - (b - a) - Y)$ are compared: $V_1 > V_2$ means $d = Y$, while $V_1 < V_2$ suggests $d = (b - a) - Y$. Because the method only applies to tracking displacement of non-monotonic functions, a reference block is

(a) motion tracking scheme **(b) example image**

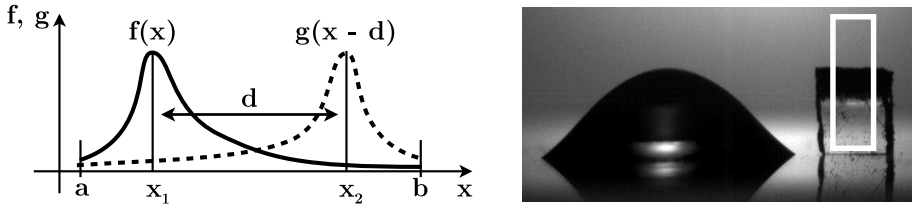

Figure C.1: Schematics of motion tracking d and its application to a real experimental image.

placed on the substrate to mimic the peak, as shown in figure C.1(b). For any side-view image sequence, substrate vibration is tracked by comparing the position of the reference block in any frame to that in the first frame. Functions $f(x)$ and $g(x)$ are the greyscale values pixels summed horizontally within the same rectangular regions. Note that no sub-pixel interpolation is adopted and hence the resolution is 1-pixel in all motion-tracking computations.

APPENDIX D

IMAGE ANALYSIS II: FREQUENCY ESTIMATION

For all observed modes of vibrated sessile drops, the resonance frequencies f_r are estimated from image sequences as

$$f_r \approx f_s \times \frac{N_c}{N} \tag{D.1}$$

where f_s is the frame rate or sampling frequency for recording an image sequence and N the number of frames within which the drop completes N_c cycles of oscillation. For image sequences with $a \times b$ pixels in each frame, denote k and j the horizontal and vertical coordinates of pixels, and $M_r[k,j]$ and $M_i[k,j]$ as matrices of greyscale values of pixels in the reference frame and a dynamic snapshot, respectively. A norm $z[i]$ quantifying difference between the i-th and the reference image is defined as

$$z[i] = \Big\{ \sum_{j=0}^{a} \sum_{k=0}^{b} \Big(M_i[k,j] - M_r[k,j] \Big)^2 \Big\}^{1/2} \tag{2.1.2}$$

The norm $z[i]$, which is essentially the the $\mathcal{L}-2$ norm of the difference between two images, sensitively reflects any slightest variation of one image from the other. As compared in figure D.1, $z[i]$ provides a broader coverage of variation detection than, say, a norm based on inner product (i.e. only the difference in M_r and M_i's orientations), since $z[i]$ does not only detects motion (e.g., translation, rotation, distortion, etc.) be detected and quantified, but also any flickering of lighting for perfectly static scenes.

An example of frequency estimation is illustrated in figure D.2. The image sequence is recorded at 5000 frames per second. From figure D.2(a), $z[i]$ minimizes twice and hence $N_c = 2$. From figure D.2(b), the second local minimum of $z[i]$

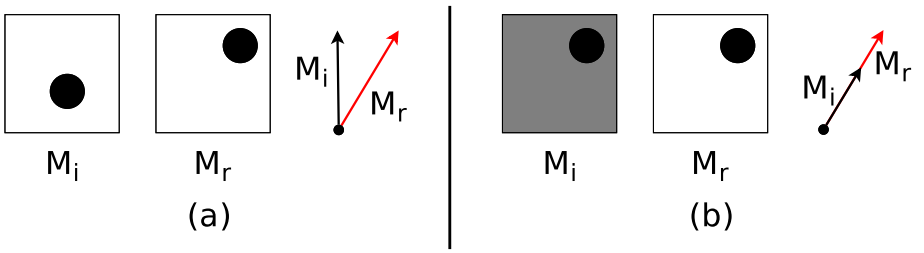

Figure D.1: Comparison of $z[i]$ vs. a norm based on inner product

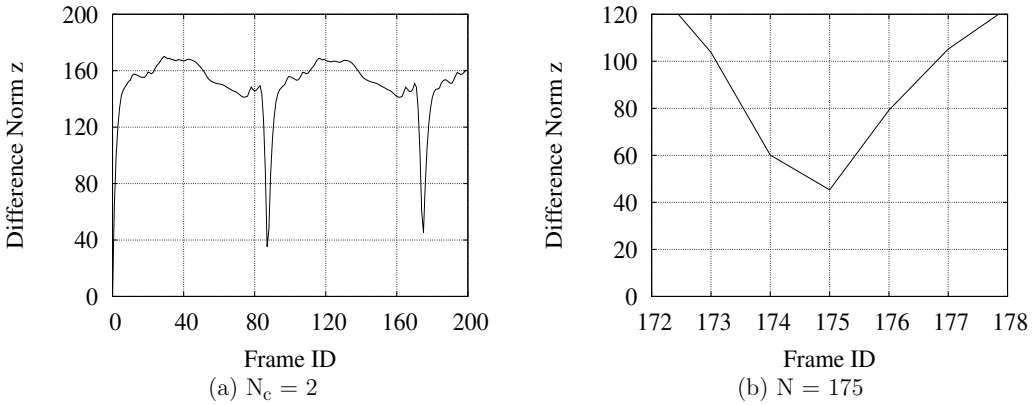

(a) $N_c = 2$ (b) $N = 175$

Figure D.2: An example of frequency estimation

occurs at $i = 175$, and hence $N = 175$. Therefore

$$f_r = 5000 \times \frac{2}{175} = 57.14(Hz) \tag{D.2}$$

Because Eq. D.1 provides only an estimation, the result is not exact. Among the parameters, f_s is a controlled parameter and N_c is obtained from figure D.2(a) with no ambiguity. Hence only the estimation of N can contribute to any error. For the observed minimal difference at $i = 175$, the actual 'minimum' of $z[i]$ may correspond to any instant between those when frames $i = 174$ and 176 are captured. In other words, a maximal under- or overestimation of one frame for N is expected. For experiments recording at least 20 frames per period and a total of 200 frames per image sequence, the result of a preliminary error estimation is obtained as shown in table. D.1, where $N_{\max}$ and $N_{\min}$ are the maximal and minimal number of frames per period possible given an N_c, and N_r the remaining frames of images

N_c	$N_{\max}$	$N_{\min}$	N_r	$\epsilon_{\max+}(\%)$	$\epsilon_{\max-}\%)$	$\epsilon_{\min+}(\%)$	$\epsilon_{\min-}(\%)$
1	200	101	99	0.002	0.003	0.010	0.010
2	200	68	64	0.005	0.005	0.043	0.044
3	200	51	47	0.007	0.008	0.113	0.118
4	200	41	36	0.010	0.010	0.232	0.244
5	200	34	30	0.012	0.013	0.420	0.446
6	200	29	26	0.015	0.015	0.690	0.739
7	200	26	18	0.017	0.018	0.997	1.077
8	200	23	16	0.020	0.020	1.449	1.581
9	200	21	11	0.022	0.023	1.948	2.143
10	200	19	10	0.025	0.025	2.632	**2.924**

Table D.1: Error estimation of resonance frequencies

not counted towards the N_c cycles. The error estimates ϵ are defined as

$$\epsilon_{\max\pm} = \left|\frac{1}{N_{\max}} - \frac{1}{N_{\max}\pm 1}\right|, \qquad \epsilon_{\min\pm} = \left|\frac{1}{N_{\min}} - \frac{1}{N_{\min}\pm 1}\right| \tag{D.3}$$

Accordingly, table. D.1 suggests that the estimated resonance frequencies possess a precision of approximately 3%.

APPENDIX E

SPECTRAL ANALYSIS: OPTIMIZED FFT

To optimize amplitude estimation in frequency analysis, data sequences are optimally truncated. Given the frequency spectrum of a signal in figure E.1(a), suppose amplitude A_t is sought, and FFT yields f_1 and f_2 as the closest sampled frequencies to f_t. The optimization truncates the data sequence to locate one of the sampled frequencies as closely to f_t as possible. The closeness is quantified by *frequency bias ratio* (FBR):

$$FBR \equiv \frac{\min[|f_t - f_1|, |f_t - f_2|]}{\max[|f_t - f_1|, |f_t - f_2|]} \tag{E.1}$$

The optimization minimizes FBR to maximize A_t and signal-to-noise ratio (SNR). The effectiveness of the method is demonstrated in figure E.1(b): lower FBR gives higher SNR. Hence the closer a sampled frequencies matches f_t, the better the amplitude estimation from frequency analysis. For a data sequence with length L_0, the method performs optimization on a sampled (given at frequency f_s), single-frequency sine wave and suggests the optimal length for a data sequence from experiment. The FBRs for data lengths $L = L_0, L_0-1, L_0-2, ..., L_{\min}(> f_s/f_d)$ are calculated and the data length with the minimal FBR is suggested. Although the method maximizes A_t at f_t and possibly underestimates other signals, it is adequate for our experiments since only signals at specific frequencies are considered.

(a) definition of FBR

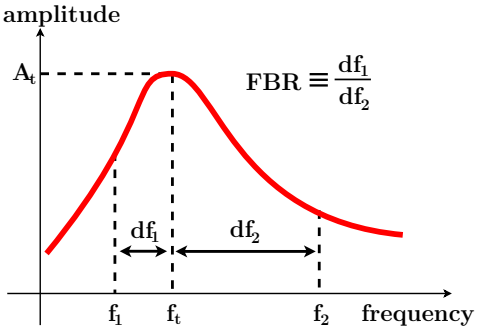

(b) FBR vs. SNR

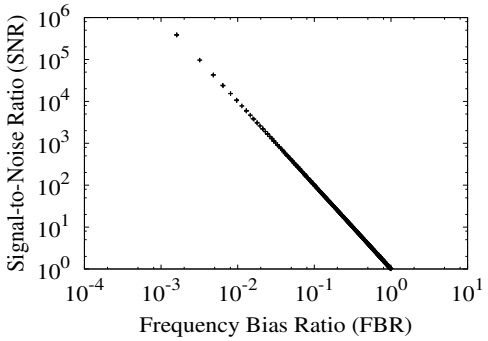

Figure E.1: The preparatory optimization for FFT. (a) Definition of frequency bias ratio FBR $\equiv df_1/df_2$, where $df_1 < df_2$. (b) Results of $f_d = 103$Hz, $f_s = 5000$Hz suggests that lower FBR gives higher SNR.

APPENDIX F

CHEMICAL PROTOCOL I: SURFACE MODIFICATION

Controlling contact angles of drops is crucial in this experimental study. As reported in the literature[93], a drop's resonance frequencies sensitively depend upon its contact angle. To probe the variation of frequency response with contact angle, either substrates with different wettabilities can be implemented to achieve different contact angles, or pinning sites can be implemented on substrates. Pinning sites are the more hydrophilic regions on a substrate. Technically, they can be created based on contrasting surface chemistry, presence and absence of physical structures, or a combination of both. As it turns out, implementing pinning sites is the more efficient method since fixing the footprints of drops allows controlling their contact angles by simply prescribing their volumes. Therefore one substrate with a pinning site allows testing drops with a wide range of contact angles. A pinning site can be created based on contrasting surface chemistry, presence and absence of physical structures, or a combination of both. The key aspects here is, among all reported techniques, how to combine various physical and chemical treatments to achieve a sufficient contrast between the wettabilities in- and outside pinning sites. To clearly visualize vibrated drops, preferred methods are those allowing transparency of substrates.

For surface modification and especially the preparation of superhydrophobic surfaces, numerous methods have been reported in the literature. Most methods incorporate both physical patterning and chemical coating. The most typical chemical coating process is silanization, in which fluoro or chloro silane is deposited onto a substrate either by chemical vapor deposition[33, 63, 51] or soaking[84, 20]. The physical patterns may be created by, including but not limited

to, replicating natural patterns on plant leaves[64], lithography[84, 115, 46, 44], electrospinning[19, 82, 69], regular[96] or irregular [59, 21, 56, 92, 40] self-assembly of nanoparticles, electroplating[110, 58] conductive (typically metal) substrates, hard anodization[13], sandblasting[20] and chemical etching in liquid[20, 106, 81, 112] or plasma phase[45], depositing mixture of polymer emulsion[107], growing carbon nanotube[63, 88], sol-gel method[70, 61, 34, 66], and surface recrystalization[23]. To pattern substrates for testing superhemispherical drops, feasibility of all surface patterning methods are examined. Among the methods, those based on lithography offer perfect controllability but are unfortunately cost-effective. Methods require electric conductivity[110, 58, 13] are inadequate because visualizing drops require transparency of the substrate. Common solid materials are either conductive (like metal) or transparent (like glass or plastic). Those depositing nanoparticles cannot be adopted in experiments with vibrating drops, since the particles are not permanently bonded to the surface and can be easily removed. Chemical etching, sol-gel method and growing carbon nanotube possibly require substantial knowledge of substrate-specific chemistry and special fabrication apparatus and hence are not adopted. By excluding all inadequate methods, solvent-induced recrystalization of polycarbonate[23] is finally adopted for implementing substrates of superhemispherical drops. As chemical coating alone provides sufficient wettability contrast, substrates for subhemispherical drops are prepared with physical patterns.

The experiments are conducted using three types of solid substrates, as tabulated in table F.1. Among these, types A and B are fabricated with circular pinning sites of prescribed sizes, while type C substrates are homogeneously treated. The pinning sites on these substrates are the more hydrophilic regions and can be created based on contrasting surface chemistry, presence and absence of phys-

Table F.1: Characteristics of substrates. F-silane = fluoro silane, APTES = amine silane. Φ = diameter.

substrate	pattern	coating	pin site	contact angle
A (glass)	none	F-silane, partial	$\Phi = 5$mm	$35° \sim 105°$
B (PC)	PC crystal	F-silane, homogeneous	$\Phi = 2.5$mm	$105° \sim 135°$
C (glass)	none	APTES, homogeneous	none	$60° \sim 80°$

ical structures, or a combination of both. The implemented pinning sites ensure reasonably circular footprints of drops and also allow controlling a drop's contact angle α by simply prescribing its volume. Tremendous effort in experiments is saved by such implementation, since no contact angle measurement is needed and all optical components stay fixed for all experiments once a substrate is installed onto the observation platform, since drops can no longer translate on the substrate.

F.1 Materials

Glass slides (VWR VistaVision, catalog No. 16004-430, 3×1×1 mm) were purchased from VWR International (Radnor, PA). Stainless steel woven metal mesh (#150, part number 85385T875) and polycarbonate sheets (12"×12"×1/16", Makrolon GP-V, made by Sheffield Plastics Inc.) were purchased from McMaster-Carr (Cleveland, OH). Ethanol (reagent alcohol, absolute, CAS# 64-17-5; Macron Chemicals) and acetone (CAS# 67-64-1; Macron Chemicals) were purchased from VWR International (Radnor, PA). High-purity compressed nitrogen and oxygen were purchased from Airgas (Salem, NH). Sulfuric acid (9598% min., MW 98.08, CAS# 7664-93-9) was purchased from VWR International (Radnor, PA). Hydrogen peroxide solution (50 wt%, 516813-500ML, CAS# 7722-84-1 MW 34.01 g/mol) was purchased from Sigma-Aldrich (St. Louis, MO). Silane products, both 3-aminopropyltriethoxysilane (APTES, product code: SIA0127.0) and (HEPTADECAFLUORO-1,1,2,2-

TETRAHYDRODECYL)TRICHLOROSILANE (product code: SIH5841.0), are purchased from Gelest, Morrisville, PA. Light mineral oil was purchased from Fisher Scientific (Pittsburgh, PA). Sylgard 184 PDMS was purchased from Dow Corning (Midland, MI).

F.2 Piranha Cleaning of Glass Slides

For substrates of types A and C, glass slides were sonicated for 20 minutes in water to remove any solid particles on their surfaces. To remove any organic contaminants, the slides were then soaked for 20 min in piranha solution (70% sulfuric acid/30% hydrogen peroxide). Afterwards the glass slides were rinsed by de-ionized (DI) water (purified by an Elga Ultra SC MK2, Siemens) for at least 10 minutes and kept fully immersed under DI water until the next step.

F.3 Substrate A: Surfaces for Pinned Subhemispherical Drops

Type A substrates are prepared purely based on surface chemistry. After piranha-cleaning and rinsing, glass slides from Appendix F.2 are dried by high-purity nitrogen for coating. The coating is prepared by mixing 2μL of (HEPTADECAFLUORO-1,1,2,2-TETRAHYDRODECYL)TRICHLOROSILANE in 2 grams of light mineral oil and then degassing for 20 minutes to remove gaseous impurities. The silane is coated onto the cleaned and dried glass slides by chemical vapor deposition (CVD) for at least 5 hours. The slides are then heated at 85°C for 15 minutes to further secure the coating. To create a pinning site, a coated

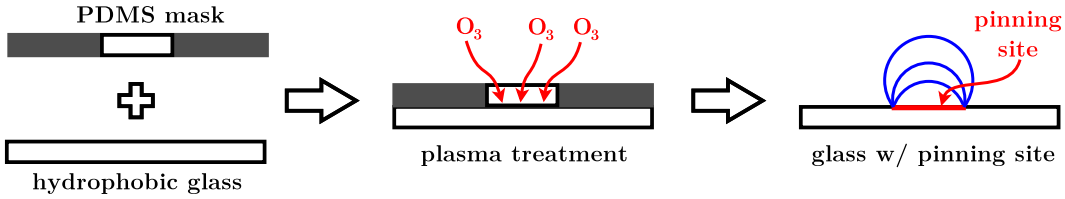

Figure F.1: Schematic of implementing pinning site on glass slides with partial plasma treatment.

slide is covered by a soft polymer (PDMS) with a prescribed circular opening of 5-mm diameter and subsequently treated by oxygen plasma (Harrick Plasma, Ithaca, NY) for 1 minute. With the plasma treatment, the coated silane molecules are removed by plasma within the uncovered circular region, as shown in figure F.1. The maximal static contact angle for water drops on a fluoro-silane-coated surface is approximately 105°, which is also the upper limit below which a drop stays pinned on the pinning site.

F.4 Substrate B: Surfaces for Pinned Superhemispherical Drops

Type B substrates are implemented based on physical structures. The method is developed with reference to [23]. A PDMS stamp with circular pillars are prepared first, as shown in figure F.2(a). The implementation starts with preparing 3”×1” stripes of PC sheets and removing the middle 1”×1” of protective film. Very gently, the polymer stamp and the PC stripe are clamped together, with the circular pillars contacting the 1”×1” exposed PC surface to shield circular regions in subsequent acetone treatment, as shown in figure F.2(b). The stripe and the stamp are soaked together in acetone for 6 minutes. Upon completion of acetone treatment, the stamp is removed from the stripe, which is then dried with compressed

air thoroughly. Except within the shielded circular regions, patterns of recrystalization should render the acetone-treated PC stripe translucent. The treated PC is then cleaned with ozone plasma (Basic Plasma Cleaner PDC-32G, by Harrick Plasma, Ithaca, NY) at 600mTorr (regulated by PlasmaFlo Gas Flow Mixer PDC-FMG, by Harrick Plasma, Ithaca, NY) for 1 minute. The same chemical coating is subsequently applied to the plasma-cleaned PC with the same procedure as for type A substrates, except at least 40 hours must be allowed for CVD. Note that chemical coating is neither applied nor suggested in [23], and sufficiently recrystalized PC surfaces are indeed completely non-wetting for small, quasi-statically deposited sessile drops. Under excitations of $30g$ or higher, however, the coating is necessary for preventing sessile drops from spreading on the surface and penetrating into the physical structure of recrystalized PC. The maximal static contact angle for de-ionized water drops on silane-coated, recrystalized PC surface is approximately 149°. While type A substrates are completely transparent, type B substrates are translucent except within the pinning sites. Due to the homogeneous silane coating, minimal contact angle of de-ionized water drops on type B substrates is approximately 105°.

F.5 Substrate C: Surfaces for Partially Pinned, Subhemispherical Drops

Substrates C are homogeneously coated with APTES silane to achieve a contact angle of DI water drops in the range of $45° \sim 80°$. To begin, the interior surface of a 400-ml staining dish and a glass rack were rinsed, in order, with (1) soap, (2) RO water, (3) ethanol, and (4) acetone. The dish and rack were then blown

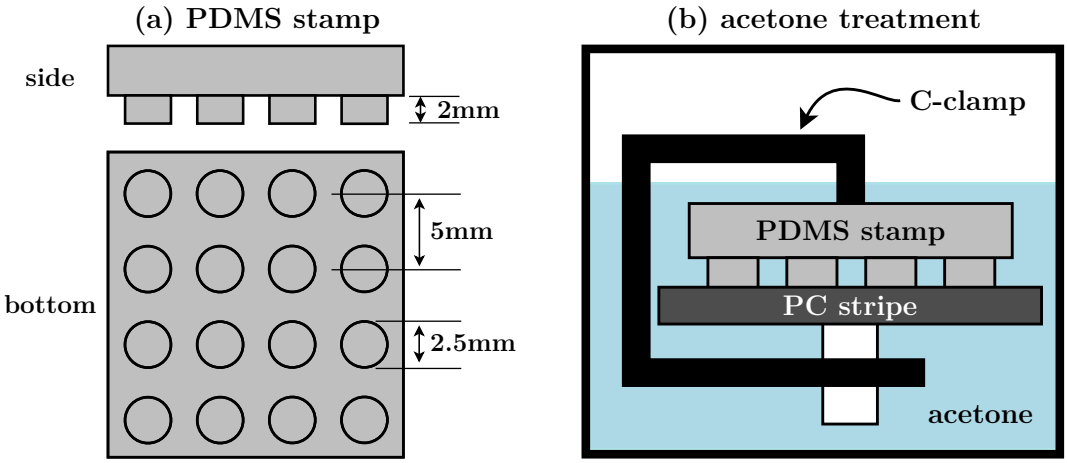

Figure F.2: Acetone treatment of polycarbonate: (a) specification of the PDMS stamp used in acetone treatment of PC, (b) a PC stripe masked by a PDMS mask and soaked in acetone.

dry by nitrogen gas and baked in the oven for 15 min. 200 ml of acetone and 8 ml of APTES silane were deposited in the cleaned staining dish. Each piranha-cleaned glass slide was dried by blowing high-purity nitrogen gas and placed onto the immersed glass rack in the APTES silane solution for 20 min. Afterwards the samples were moved to an oven for heating at 85°C for 20 minutes. Prior to their first use, all coated glass slides were rinsed with ethanol and DI water and dried with high-purity nitrogen gas. Based on 222 measurements of 40 substrates, average contact angle of DI water drops on type C substrates was approximately 68.6°C, with a standard deviation of 5°C.

F.6 Surface Characterization

Wettability of coated glass slides was characterized by measuring the contact angles of 20 μL drops on the surfaces. Contact angles were measured using static images of drops before using the same drop in oscillation experiments. Images were processed using ImageJ v.1.45.

APPENDIX G

CHEMICAL PROTOCOL II: PDMS PREPARATION

The PDMS balloon samples for liquid balloon experiments are prepared by first mix PDMS and crosslinker with prescribed cross-linking ratio (10/1 by weight recommended by manufacturer). The mixture is degassed for 10 minutes to remove gaseous impurities and trapped bubbles. Two glass slides with (HEPTADECAFLUORO-1,1,2,2-TETRAHYDRODECYL)TRICHLOROSILANE coating are prepared (Appendix F). A pair of spacers with a desired thickness are placed on a hydrophobic both ends of one of the hydrophobic glass slide. The degassed PDMS mixture is gently poured onto the hydrophobic glass slide, and the other hydrophobic glass slide is gently covered, as depicted in figure G.1. The PDMS mixture is then vulcanized between the two slides at $75°C$ for at least 2 hours. Afterwards a plastic mold and a glass pipe are placed on the membrane, and addition PDMS mixture is poured into the mold to cast the PDMS substrate. The same vulcanization process is repeated.

Thickness of a PDMS membrane sample is measured before detaching glass slides. While remaining attached, the membrane and glass slides are held vertical on the microscope stand. The thickness is then measured from the microscope

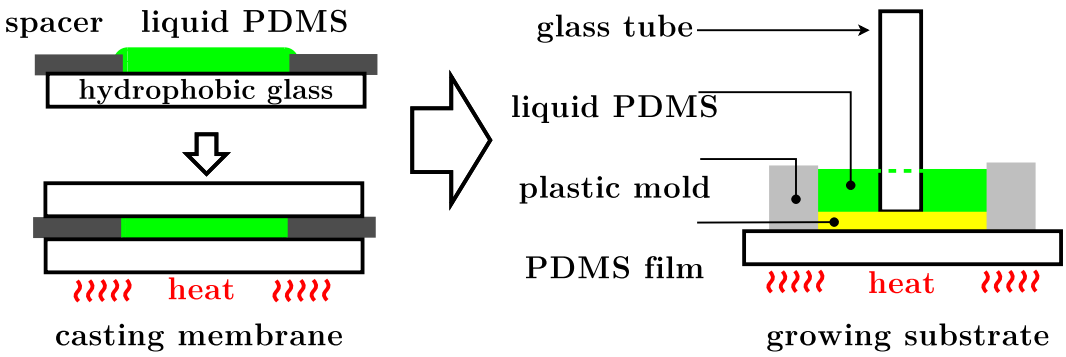

Figure G.1: Preparation of a PDMS balloon sample.

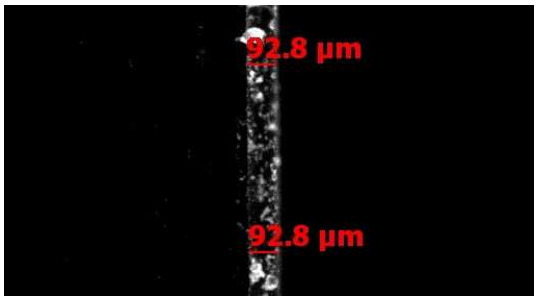

Figure G.2: Thickness of PDMS membrane measured by microscope.

image of the membrane's side (edge) view. An examples is presented in figure G.2.

APPENDIX H

CHEMICAL PROTOCOL III: LATEX RUBBER PREPARATION

Rubber membrane samples are made from raw latex rubber (AeroMarine Liquid Latex Mold Making Rubber, AeroMarine Products, Inc., San Diego, CA) by spin coating[15, 78]. Because the rubber is not crosslinked but dehydrated to solidify, the casting method for PDMS is not applicable. Instead, solidifying samples simply requires good ventilation for water in the liquid rubber to evaporate. Sample preparation starts with adding 10% DI water (by volume) to raw liquid rubber to reduce viscosity to roughly 115 centipoise. The diluted rubber solution is deposited in a syringe. A circular borosilicate glass disc (product # 8477K57, by McMaster-Carr, Cleveland, OH) is installed on the spin coater (SCS P-6700 Portable Precision Spin Coater, Specialty Coating Systems, Inc., Indianapolis, IN) for spin coating. When the spin coater achieves a prescribed spinning rate, the rubber solution is dispensed at the center of the glass disc until the disc's surface is filled. With spin-coated latex rubber on it, the glass disc is placed in a fume hood. At least one hour is allowed for drying the rubber membrane. The thickness of a sample is only controlled by spinning rates, and all other parameters (temperature, drying time, etc) remain the same.

Once a sample completely solidifies, its thickness is measured by a profilometer (Veeco Dektak 6M, by Bruker, Camarillo, CA). A small portion of the rubber is cut and removed to expose the underlying glass disc. The sample is then scanned across the cut to touch both the rubber and the glass. Each scan starts from the rubber side and collects 7500 data points. An example of a scanned profile is shown in figure H.1. The last 1000 data points (position $>$ 2.6cm) are fit to a straight line as the surface of the glass. Thickness of the membrane is calculated as the

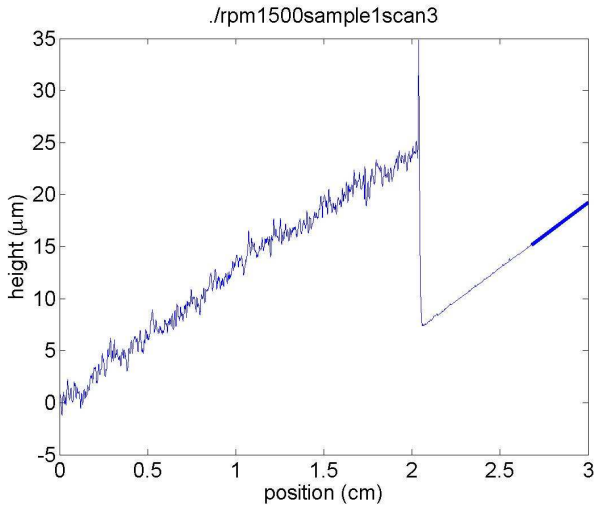

Figure H.1: An example of results from scanning rubber membrane surface with a profilometer.

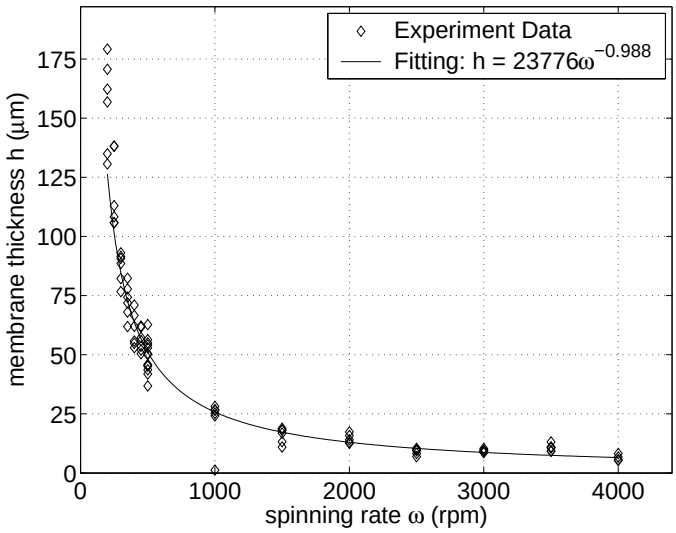

Figure H.2: Accumulated results of spinning rate vs. thickness for latex rubber samples.

average distance of the first by first fitting 3750 data points (position < 1.5cm) from the fitted glass surface. Thickness and spinning rate for all samples are fit to in the curve $h_f = K\omega^{\beta}$, as shown in figure H.2. Result of curve fitting is

$$h_f = 23776 \times \omega^{-0.988} \tag{H.1}$$

BIBLIOGRAPHY

[1] Mohammad Mahdi Aeinehvand, Fatimah Ibrahim, Sulaiman Wadi harun, Wisam Al-Faqheri, Tzer Hwai Gilbert Thio, Amin Kazemzadeh, and Marc Madou. Latex micro-balloon pumping in centrifugal microfluidic platforms. *Lab Chip*, 14:988–997, 2014.

[2] Inc. ANSYS. *ANSYS FLUENT UDF Manual R14.5*. ANSYS, Inc., Canonsburg, PA, 2012.

[3] Hisao Azuma and Shoichi Yoshihara. Three-dimensional large-amplitude drop oscillations: experiments and theoretical analysis. *Journal of Fluid Mechanics*, 393:309–332, 8 1999.

[4] B. Batson, F. Zoueshtiagh, and R. Narayanan. The faraday threshold in small cylinders and the sidewall non-ideality. *Journal of Fluid Mechanics*, 729:496–523, 8 2013.

[5] Michael Baudoin, Philippe Brunet, Olivier Bou Matar, and Etienne Herth. Low power sessile droplets actuation via modulated surface acoustic waves. *Applied Physics Letters*, 100(15):–, 2012.

[6] Terry P. Bigioni, Xiao-Min Lin, Toan T. Nguyen, Eric I. Corwin, Thomas A. Witten, and Heinrich M. Jaeger. Kinetically driven self assembly of highly ordered nanoparticle monolayers. *Nat Mater*, 5:265–270, 2006.

[7] J.B. Bostwick and P.H. Steen. Capillary oscillations of a constrained liquid drop. *Phys. Fluids*, 21:032108, 2009.

[8] J.B. Bostwick and P.H. Steen. Coupled oscillations of deformable spherical-cap droplets. part 1. inviscid motions. *J. Fluid Mech.*, 714:312–335, 2013.

[9] J.B. Bostwick and P.H. Steen. Coupled oscillations of deformable spherical-cap droplets. part 2. viscous motions. *J. Fluid Mech.*, 714:336–360, 2013.

[10] J.B. Bostwick and P.H. Steen. Dynamics of drops with contact-line mobility. part 1. theory of natural oscillation. *J. Fluid Mech.*, under review.

[11] P. Brunet, J. Eggers, and R. D. Deegan. Vibration-induced climbing of drops. *Phys. Rev. Lett.*, 99:144501, Oct 2007.

[12] P. Brunet and J.H. Snoeijer. Star-drops formed by periodic excitation and on an air cushion a short review. *The European Physical Journal Special Topics*, 192(1):207–226, 2011.

[13] Josephus G. Buijnsters, Rui Zhong, Natalia Tsyntsaru, and Jean-Pierre Celis. Surface wettability of macroporous anodized aluminum oxide. *ACS Applied Materials and Interfaces*, 5(8):3224–3233, 2013.

[14] S. Chandrasekhar. *Hydrodynamic and Hydromagnetic Stability*. Oxford University Press, New York, NY, 1961.

[15] Chao-Ching Chang, Chia-Ling Pai, Wen-Chang Chen, and Samson A. Jenekhe. Spin coating of conjugated polymers for electronic and optoelectronic applications. *Thin Solid Films*, 479(12):254 – 260, 2005.

[16] Chun-Ti Chang, Joshua B. Bostwick, Susan Daniel, and Paul H. Steen. Dynamics of drops with contact-line mobility. part 2. experiment. *J. Fluid Mech.*, under review.

[17] Chun-Ti Chang, Joshua B. Bostwick, Paul H. Steen, and Susan Daniel. Substrate constraint modifies the rayleigh spectrum of vibrating sessile drops. *Phys. Rev. E*, 88:023015, Aug 2013.

[18] Nicolas Abi Chebel, Frederic Risso, and Olivier Masbernat. Inertial modes of a periodically forced buoyant drop attached to a capillary. *Physics of Fluids (1994-present)*, 23(10):–, 2011.

[19] Daehwan Cho, Huajun Zhou, Youngjin Cho, Debra Audus, and Yong Lak Joo. Structural properties and superhydrophobicity of electrospun polypropylene fibers from solution and melt. *Polymer*, 51(25):6005 – 6012, 2010.

[20] Handong Cho, Dongseob Kim, Changwoo Lee, and Woonbong Hwang. A simple fabrication method for mechanically robust superhydrophobic surface by hierarchical aluminum hydroxide structures. *Current Applied Physics*, 13(4):762 – 767, 2013.

[21] Young-Sang Cho, JongWoo Moon, DongChan Lim, and YoungDok Kim. Fabrication of superhydrophobic surfaces using structured colloids. *Korean Journal of Chemical Engineering*, 30(5):1142–1152, 2013.

[22] S. Ciliberto and J. P. Gollub. Chaotic mode competition in parametrically forced surface waves. *Journal of Fluid Mechanics*, 158:381–398, 9 1985.

[23] Yuehua Cui, Adam T. Paxson, Katherine M. Smyth, and Kripa K. Varanasi. Hierarchical polymeric textures via solvent-induced phase transformation: A single-step production of large-area superhydrophobic surfaces. *Colloids and Surfaces A: Physicochemical and Engineering Aspects*, 394(0):8 – 13, 2012.

[24] Susan Daniel and Manoj K. Chaudhury. Rectified motion of liquid drops on gradient surfaces induced by vibration. *Langmuir*, 18(9):3404–3407, 2002.

[25] Susan Daniel, Manoj K. Chaudhury, and John C. Chen. Fast drop movements resulting from the phase change on a gradient surface. *Science*, 291(5504):633–636, 2001.

[26] Susan Daniel, Manoj K. Chaudhury, and P.-G. de Gennes. Vibration-actuated drop motion on surfaces for batch microfluidic processes. *Langmuir*, 21(9):4240–4248, 2005.

[27] Julie Diani, Bruno Fayolle, and Pierre Gilormini. A review on the mullins effect. *European Polymer Journal*, 45(3):601 – 612, 2009.

[28] L. Dong, A. Chaudhury, and M.K. Chaudhury. Lateral vibration of a water drop and its motion on a vibrating surface. *The European Physical Journal E*, 21(3):231–242, 2006.

[29] S Dorbolo, D Terwagne, N Vandewalle, and T Gilet. Resonant and rolling droplet. *New Journal of Physics*, 10(11):113021, 2008.

[30] A. Dorfmann and R.W. Ogden. A constitutive model for the mullins effect with permanent set in particle-reinforced rubber. *International Journal of Solids and Structures*, 41(7):1855 – 1878, 2004.

[31] S. Douady and S. Fauve. Pattern selection in faraday instability. *EPL (Europhysics Letters)*, 6(3):221, 1988.

[32] W. S. Edwards and S. Fauve. Patterns and quasi-patterns in the faraday experiment. *Journal of Fluid Mechanics*, 278:123–148, 11 1994.

[33] Juan V. Escobar, Cristina Garza, Juan Carlos Alonso, and Rolando Castillo. Super-mercuryphobic and hydrophobic diamond surfaces with hierarchical

structures: Vanishment of the contact angle hysteresis with mercury. *Applied Surface Science*, 273(0):692 – 701, 2013.

[34] Youhua Fan, Changzhu Li, Zejun Chen, and Hong Chen. Study on fabrication of the superhydrophobic sol-gel films based on copper wafer and its anti-corrosive properties. *Applied Surface Science*, 258(17):6531 – 6536, 2012.

[35] M. Faraday. On a peculiar class of acoustical figures; and on certain forms assumed by groups of particles upon vibrating elastic surfaces. *Philosophical Transactions of the Royal Society of London*, 121:299–340, 1831.

[36] I.S. Fayzrakhmanova and A.V. Straube. Stick-slip dynamics of an oscillated sessile drop. *Phys. Fluids*, 21:072104, 2009.

[37] Anny L. Flory, David A. Brass, and Kenneth R. Shull. Deformation and adhesive contact of elastomeric membranes. *Journal of Polymer Science Part B: Polymer Physics*, 45(24):3361–3374, 2007.

[38] J.W. Fox and N.C. Goulbourne. On the dynamic electromechanical loading of dielectric elastomer membranes. *Journal of the Mechanics and Physics of Solids*, 56(8):2669 – 2686, 2008.

[39] J.W. Fox and N.C. Goulbourne. Electric field-induced surface transformations and experimental dynamic characteristics of dielectric elastomer membranes. *Journal of the Mechanics and Physics of Solids*, 57(8):1417 – 1435, 2009.

[40] Andreas Geissler, Longquan Chen, Kai Zhang, Elmar Bonaccurso, and Markus Biesalski. Superhydrophobic surfaces fabricated from nano- and microstructured cellulose stearoyl esters. *Chem. Commun.*, 49:4962–4964, 2013.

[41] D. Gerlach, G. Tomar, G. Biswas, and F. Durst. Comparison of volume-of-fluid methods for surface tension-dominant two-phase flows. *International Journal of Heat and Mass Transfer*, 49(34):740 – 754, 2006.

[42] A. Lasek H. Rodot, C. Bisch. Zeor-gravity simulation of liquids in contact with a solid surface. *Acta Astronautica*, 6:1083, 1979.

[43] Ole Hassager, Susanne B. Kristensen, Johannes R. Larsen, and Jesper Neergaard. Inflation and instability of a polymeric membrane. *Journal of Non-Newtonian Fluid Mechanics*, 88(12):185 – 204, 1999.

[44] Yang He, Chengyu Jiang, Hengxu Yin, Jun Chen, and Weizheng Yuan. Superhydrophobic silicon surfaces with micronano hierarchical structures via deep reactive ion etching and galvanic etching. *Journal of Colloid and Interface Science*, 364(1):219 – 229, 2011.

[45] E. K. Her, T.-J. Ko, B. Shin, H. Roh, W. Dai, W. K. Seong, H.-Y. Kim, K.-R. Lee, K. H. Oh, and M.-W. Moon. Superhydrophobic transparent surface of nanostructured poly(methyl methacrylate) enhanced by a hydrolysis reaction. *Plasma Processes and Polymers*, 10(5):481–488, 2013.

[46] Dale L. Herbertson, Carl R. Evans, Neil J. Shirtcliffe, Glen McHale, and Michael I. Newton. Electrowetting on superhydrophobic su-8 patterned surfaces. *Sensors and Actuators A: Physical*, 130131(0):189 – 193, 2006. Selected Papers from {TRANSDUCERS} '05 The 13th International Conference on Solid-State Sensors, Actuators and Microsystems - Seoul, Korea, 5-9 June 2005.

[47] R. J. A. Hill and L. Eaves. Vibrations of a diamagnetically levitated water droplet. *Phys. Rev. E*, 81:056312, May 2010.

[48] C.W Hirt and B.D Nichols. Volume of fluid (vof) method for the dynamics of free boundaries. *Journal of Computational Physics*, 39(1):201 – 225, 1981.

[49] L.M. Hocking. Waves produced by a vertically oscillating plate. *J. Fluid Mech.*, 179:267–281, 1987.

[50] Norman J. Holter and Wilford R. Glasscock. Vibrations of evaporating liquid drops. *The Journal of the Acoustical Society of America*, 24(6):682–686, 1952.

[51] Atsushi Hozumi, Dalton F. Cheng, and Makoto Yagihashi. Hydrophobic/superhydrophobic oxidized metal surfaces showing negligible contact angle hysteresis. *Journal of Colloid and Interface Science*, 353(2):582 – 587, 2011.

[52] Robert W Smithwick III and Joseph A.M Boulet. Vibrations of microscopic mercury droplets on glass. *Journal of Colloid and Interface Science*, 130(2):588 – 596, 1989.

[53] Robert W Smithwick III and Doyle M Hembree Jr. Preliminary studies of an oscillating mercury-droplet electrode. *Journal of Colloid and Interface Science*, 140(1):57 – 65, 1990.

[54] A. James, B. Vukasinovic, M.K. Smith, and A. Glezer. Vibration-induced drop atomization and bursting. *J. Fluid Mech.*, 476:1–28, 2003.

[55] K. L. Johnson, K. Kendall, and A. D. Roberts. Surface energy and the contact of elastic solids. *Proceedings of the Royal Society of London. A. Mathematical and Physical Sciences*, 324(1558):301–313, 1971.

[56] Shabnam Joneydi, Akbar Khoddami, and Ali Zadhoush. Novel superhydrophobic top coating on surface modified pvc-coated fabric. *Progress in Organic Coatings*, 76(5):821 – 826, 2013.

[57] Sunghwan Jung, Erica Kim, Michael J. Shelley, and Jun Zhang. Surface waves on a semitoroidal water ring. *Physics of Fluids (1994-present)*, 19(5):–, 2007.

[58] Zhixin Kang, Qi Ye, Jing Sang, and Yuanyuan Li. Fabrication of superhydrophobic surface on copper surface by polymer plating. *Journal of Materials Processing Technology*, 209(9):4543 – 4547, 2009.

[59] Eun-Kyeong Kim, Chul-Sung Lee, and Sang Sub Kim. Superhydrophobicity of electrospray-synthesized fluorinated silica layers. *Journal of Colloid and Interface Science*, 368(1):599 – 602, 2012.

[60] Erwin Kreyszig. *Differential Geometry*. Dover Publications, Mineola, New York, 1991.

[61] R.V. Lakshmi, T. Bharathidasan, Parthasarathi Bera, and Bharathibai J. Basu. Fabrication of superhydrophobic and oleophobic sol-gel nanocomposite coating. *Surface and Coatings Technology*, 206(1920):3888 – 3894, 2012.

[62] H. Lamb. *Hydrodynamics*. Cambridge University Press, Cambridge, UK, 1932.

[63] Kenneth K. S. Lau, Jos Bico, Kenneth B. K. Teo, Manish Chhowalla, Gehan A. J. Amaratunga, William I. Milne, Gareth H. McKinley, and Karen K. Gleason. Superhydrophobic carbon nanotube forests. *Nano Letters*, 3(12):1701–1705, 2003.

[64] Seung-Mo Lee and Tai Hun Kwon. Mass-producible replication of highly hydrophobic surfaces from plant leaves. *Nanotechnology*, 17(13):3189, 2006.

[65] Rong Long, Kenneth R. Shull, and Chung-Yuen Hui. Large deformation

adhesive contact mechanics of circular membranes with a flat rigid substrate. *Journal of the Mechanics and Physics of Solids*, 58(9):1225 – 1242, 2010.

[66] Shixiang Lu, Yiling Chen, Wenguo Xu, and Wei Liu. Controlled growth of superhydrophobic films by sol-gel method on aluminum substrate. *Applied Surface Science*, 256(20):6072 – 6075, 2010.

[67] Dmitry V. Lyubimov, Tatyana P. Lyubimova, and Sergey V. Shklyaev. Behavior of a drop on an oscillating solid plate. *Physics of Fluids (1994-present)*, 18(1):–, 2006.

[68] D.V. Lyubimov, T.P. Lyubimova, and S.V. Shklyaev. Non-axisymmetric oscillations of a hemispherical drop. *Fluid Dynamics*, 39(6):851–862, 2004.

[69] Minglin Ma, Randal M. Hill, Joseph L. Lowery, Sergey V. Fridrikh, and Gregory C. Rutledge. Electrospun poly(styrene-block-dimethylsiloxane) block copolymer fibers exhibiting superhydrophobicity. *Langmuir*, 21(12):5549–5554, 2005.

[70] Satish A. Mahadik, Mahendra S. Kavale, S.K. Mukherjee, and A. Venkateswara Rao. Transparent superhydrophobic silica coatings on glass by sol-gel method. *Applied Surface Science*, 257(2):333 – 339, 2010.

[71] S. Mettu and M. K. Chaudhury. Vibration spectroscopy of a sessile drop and its contact line. *Langmuir*, 28(39):14100–14106, 2012.

[72] Jong Hoon Moon, Byung Ha Kang, and Ho-Young Kim. The lowest oscillation mode of a pendant drop. *Physics of Fluids (1994-present)*, 18(2):–, 2006.

[73] M. Mooney. A theory of large elastic deformation. *Journal of Applied Physics*, 11(9):582–592, 1940.

[74] I. Mueller and P. Strehlow. *Rubber and Rubber Balloons Paradigms of Thermodynamics*. Springer-Verlag, Berlin, Germany, 2004.

[75] L. Mullins. Softening of rubber by deformation. *Rubber Chemistry and Technology*, 42(1):339 – 362, 1969.

[76] X. Noblin, A. Buguin, and F. Brochard-Wyart. Vibrated sessile drops: Transition between pinned and mobile contact line oscillations. *The European Physical Journal E*, 14(4):395–404, 2004.

[77] X. Noblin, A. Buguin, and F. Brochard-Wyart. Vibrations of sessile drops. *The European Physical Journal Special Topics*, 166(1):7–10, 2009.

[78] K. Norrman, A. Ghanbari-Siahkali, and N. B. Larsen. 6 studies of spin-coated polymer films. *Annu. Rep. Prog. Chem., Sect. C: Phys. Chem.*, 101:174–201, 2005.

[79] R. W. Ogden. Large deformation isotropic elasticity - on the correlation of theory and experiment for incompressible rubberlike solids. *Proceedings of the Royal Society of London. A. Mathematical and Physical Sciences*, 326(1567):565–584, 1972.

[80] R. W. Ogden and D. G. Roxburgh. A pseudo-elastic model for the mullins effect in filled rubber. *Proceedings of the Royal Society of London. Series A: Mathematical, Physical and Engineering Sciences*, 455(1988):2861–2877, 1999.

[81] Junfei Ou, Weihua Hu, Mingshan Xue, Fajun Wang, and Wen Li. Superhydrophobic surfaces on light alloy substrates fabricated by a versatile process and their corrosion protection. *ACS Applied Materials and Interfaces*, 5(8):3101–3107, 2013.

[82] Song Hee Park, Song Min Lee, Ho Sun Lim, Joong Tark Han, Dong Ryeol Lee, Hwa Sung Shin, Youngjin Jeong, Jooyong Kim, and Jeong Ho Cho. Robust superhydrophobic mats based on electrospun crystalline nanofibers combined with a silane precursor. *ACS Applied Materials and Interfaces*, 2(3):658–662, 2010. PMID: 20356265.

[83] M. Perez, Y. Brechet, L. Salvo, M. Papoular, and M. Suery. Oscillation of liquid drops under gravity: Influence of shape on the resonance frequency. *EPL (Europhysics Letters)*, 47(2):189, 1999.

[84] Alessandro Pozzato, Simone Dal Zilio, Giovanni Fois, Diego Vendramin, Giampaolo Mistura, Michele Belotti, Yong Chen, and Marco Natali. Superhydrophobic surfaces fabricated by nanoimprint lithography. *Microelectronic Engineering*, 83(49):884 – 888, 2006. Micro- and Nano-Engineering {MNE} 2005 Proceedings of the 31st International Conference on Micro- and Nano-Engineering.

[85] Andrea Prosperetti. Linear oscillations of constrained drops, bubbles, and plane liquid surfaces. *Physics of Fluids (1994-present)*, 24(3):–, 2012.

[86] Jean Rajchenbach, Didier Clamond, and Alphonse Leroux. Observation of star-shaped surface gravity waves. *Phys. Rev. Lett.*, 110:094502, Feb 2013.

[87] Santhosh Ramalingam, Doraiswami Ramkrishna, and Osman A. Basaran. Free vibrations of a spherical drop constrained at an azimuth. *Physics of Fluids (1994-present)*, 24(8):–, 2012.

[88] S.C. Ramos, G. Vasconcelos, E.F. Antunes, A.O. Lobo, V.J. Trava-Airoldi, and E.J. Corat. Total re-establishment of superhydrophobicity of vertically-aligned carbon nanotubes by co2 laser treatment. *Surface and Coatings Technology*, 204(1819):3073 – 3077, 2010. The Tenth International Workshop on Plasma-Based Ion Implantation and Deposition.

[89] Richard H. Rand. *Lecture Notes on Nonlinear Vibrations*. University Readers, San Diego, CA, 2012.

[90] Lord Rayleigh. On the capillary phenomena of jets. *Proceedings of the Royal Society of London*, 29(196-199):71–97, 1879.

[91] R. S. Rivlin and D. W. Saunders. Large elastic deformations of isotropic materials. vii. experiments on the deformation of rubber. *Philosophical Transactions of the Royal Society of London. Series A, Mathematical and Physical Sciences*, 243(865):251–288, 1951.

[92] S. A. Seyedmehdi, Hui Zhang, and Jesse Zhu. Fabrication of superhydrophobic coatings based on nanoparticles and fluoropolyurethane. *Journal of Applied Polymer Science*, 128(6):4136–4140, 2013.

[93] James S. Sharp, David J. Farmer, and James Kelly. Contact angle dependence of the resonant frequency of sessile water droplets. *Langmuir*, 27(15):9367–9371, 2011.

[94] C. L. Shen, W. J. Xie, and B. Wei. Parametrically excited sectorial oscillation of liquid drops floating in ultrasound. *Phys. Rev. E*, 81:046305, 2010.

[95] Richard Shilton, Ming K. Tan, Leslie Y. Yeo, and James R. Friend. Particle concentration and mixing in microdrops driven by focused surface acoustic waves. *Journal of Applied Physics*, 104(1):–, 2008.

[96] Jau-Ye Shiu, Chun-Wen Kuo, Peilin Chen, and Chung-Yuan Mou. Fabrication of tunable superhydrophobic surfaces by nanosphere lithography. *Chemistry of Materials*, 16(4):561–564, 2004.

[97] Renata M. Soares and Paulo B. Goncalves. Nonlinear vibrations and instabilities of a stretched hyperelastic annular membrane. *International Journal of Solids and Structures*, 49(34):514 – 526, 2012.

[98] J. J. Stoker. *Nonlinear Vibrations in Mechanical and Electrical Systems*. Interscience Publishers, Inc., New York, NY, 1950.

[99] M. Strani and F. Sabetta. Free vibrations of a drop in partial contact with a solid support. *Journal of Fluid Mechanics*, 141:233–247, 4 1984.

[100] M. Strani and F. Sabetta. Viscous oscillations of a supported drop in an immiscible fluid. *Journal of Fluid Mechanics*, 189:397–421, 4 1988.

[101] W. Thompson. *Mathematical and Physical Papers*. Cambridge University Press, Cambridge, UK, 1890.

[102] E. Trinh, A. Zwern, and T. G. Wang. An experimental study of small-amplitude drop oscillations in immiscible liquid systems. *Journal of Fluid Mechanics*, 115:453–474, 2 1982.

[103] E. Trinh, A. Zwern, and T.G. Wang. An experimental study of small-amplitude drop oscillations in immiscible liquid system. *J. Fluid Mech.*, 115:453–474, 1982.

[104] Henrik B. van Lengerich, Michael J. Vogel, and Paul H. Steen. Coarsening of capillary drops coupled by conduit networks. *Phys. Rev. E*, 82:066312, Dec 2010.

[105] B. Vukasinovic, M.K. Smith, and A. Glezer. Dynamics of a sessile drop in forced vibration. *J. Fluid Mech.*, 587:395–423, 2007.

[106] Peng Wan, Jingyao Wu, LiLi Tan, Bingchun Zhang, and Ke Yang. Research on super-hydrophobic surface of biodegradable magnesium alloys used for vascular stents. *Materials Science and Engineering: C*, 33(5):2885 – 2890, 2013.

[107] Huaiyuan Wang, Jingyan Zhao, Youzhuang Zhu, Yang Meng, and Yanji Zhu. The fabrication, nano/micro-structure, heat- and wear-resistance of the superhydrophobic pps/ptfe composite coatings. *Journal of Colloid and Interface Science*, 402(0):253 – 258, 2013.

[108] T. G. Wang, A. V. Anilkumar, and C. P. Lee. Oscillations of liquid drops:

results from usml-1 experiments in space. *Journal of Fluid Mechanics*, 308:1–14, 2 1996.

[109] James Whitehill, Adrian Neild, Tuck Wah Ng, and Mark Stokes. Collection of suspended particles in a drop using low frequency vibration. *Applied Physics Letters*, 96(5):–, 2010.

[110] Wenjun Xi, Zhenmei Qiao, Chunlei Zhu, Ao Jia, and Ming Li. The preparation of lotus-like super-hydrophobic copper surfaces by electroplating. *Applied Surface Science*, 255(9):4836 – 4839, 2009.

[111] Jie Xu and Daniel Attinger. Acoustic excitation of superharmonic capillary waves on a meniscus in a planar microgeometry. *Physics of Fluids (1994-present)*, 19(10):–, 2007.

[112] Chao-Hua Xue, Ping Zhang, Jian-Zhong Ma, Peng-Ting Ji, Ya-Ru Li, and Shun-Tian Jia. Long-lived superhydrophobic colorful surfaces. *Chem. Commun.*, 49:3588–3590, 2013.

[113] Sang-Hee Yoon, V. Reyes-Ortiz, Kwang-Ho Kim, Young Ho Seo, and Mohammad R K Mofrad. Analysis of circular pdms microballoons with ultralarge deflection for mems design. *Microelectromechanical Systems, Journal of*, 19(4):854–864, Aug 2010.

[114] Nobuo Yoshiyasu, Kazuhisa Matsuda, and Ryuji Takaki. Self-induced vibration of a water drop placed on an oscillating plate. *Journal of the Physical Society of Japan*, 65(7):2068–2071, 1996.

[115] Liang Zhu, Yanying Feng, Xiongying Ye, and Zhaoying Zhou. Tuning wettability and getting superhydrophobic surface by controlling surface roughness with well-designed microstructures. *Sensors and Actuators A: Physical*, 130131(0):595 – 600, 2006. Selected Papers from {TRANSDUCERS} '05 The 13th International Conference on Solid-State Sensors, Actuators and Microsystems - Seoul, Korea, 5-9 June 2005.